UNIVERSITY OF CALIFORNIA, SAN DIEGO

Development of Thermoelectric and Permanent Magnet Nanoparticles for Clean Energy Applications

A dissertation submitted in partial satisfaction of the requirements for the degree Doctor of Philosophy

in

Materials Science and Engineering

by

Phi-Khanh Nguyen

Committee in Charge:

Professor Ami Berkowitz, Co-Chair
Professor Sungho Jin, Co-Chair
Professor Prabhakar Bandaru
Professor Renkun Chen
Professor Eric Fullerton

2015

The dissertation of Phi-Khanh Nguyen is approved, and it is acceptable in quality and form for publication on microfilm and electronically:

Co-Chair

Co-Chair

University of California, San Diego

2015

DEDICATION

Dedicated to my mother and father

EPIGRAPH

"Materials science is just common sense."

- *Ami E. Berkowitz*

TABLE OF CONTENTS

LIST OF ABBREVIATIONS

BST, bismuth antimony telluride (from Bi-Sb-Te)

EDX, energy-dispersive x-ray spectroscopy

H_C, coercive force

H_{dm}, demagnetizing field

HTP, high-temperature phase (MnBi)

LTP-MnBi, low-temperature phase manganese bismuth

M_{3T}, magnetization in 3 Tesla

M_r, remnant magnetization

M_S, saturation magnetization

PM, permanent magnet

PPMS, physical property measurement system

REFPM, rare-earth-free permanent magnet

RPS, rapid process sintering

SEM, scanning electron microscopy

SPS, spark plasma sintering

T_B, superparamagnetic blocking temperature

TEM, transmission electron microscopy

VSM, vibrating sample magnetometry

QHTP, quenched high-temperature phase (MnBi)

XRD, x-ray diffraction

XRF, x-ray fluorescent spectroscopy

LIST OF FIGURES

LIST OF TABLES

PREFACE

I remember working at Devine's Pharmacy in Edison, New Jersey as a part-time store clerk throughout high school. When discussing with one of the pharmacists about my future direction, I was so confident that *nanotechnology* was going to change the world, and I wanted to be a part of this change. I don't really remember how at that age I was introduced to "nanotech", but I think it was from watching Saturday morning cartoons. It was for this reason that I later decided to pursue a bachelors in materials science and engineering at Rutgers.

As it turns out, changing the world actually takes quite a lot of time, energy, and discipline. Hungry to make an impact somehow, I devoted a lot of my efforts into Engineers Without Borders (EWB), a student organization that seeks to empower third world countries by implementing sustainable energy solutions. For years, we helped a lot of people through EWB.

During my third year at Rutgers, life brought me to a major fork in the road where key decisions regarding my career were to be made. I was studying abroad in Manchester, United Kingdom when I had to choose between a materials science summer research internship at UC Berkeley or spending the summer in a Mayan village in Guatemala to help design a system for bringing potable water to the storm-ravaged community. It was not with a heavy heart that I picked to go to Berkeley; I had before me two great choices. While at Berkeley, I did some good work with Jan Seidel and so formed a good relationship with my advisor at the time, Professor Ramamoorthy Ramesh.

When I decided to attend UC San Diego for graduate school, I was offered a position by Professor Sungho Jin to do work on nanostructured thermoelectrics in a joint collaboration with him and Professor Ami Berkowitz. I consulted with Prof. Ramesh who informed me that he had been a post-doc of Ami's and that I should definitely take this opportunity. In doing so, I worked as part of a collaboration with Samsung, while also undertaking a part-time project to produce hollow aluminum particles for a small company. As it turns out, the aluminum project lead to the suggestion of optimizing parameters in order to achieve a high fraction of nanoparticles at an extraordinarily high production rate. This discovery was applied to the thermoelectric project, and many of the successes are reported Chapter 2 of this dissertation.

Having developed the spark erosion technique into a versatile mass-nanoparticle producing machine, our team was able to secure a DOE ARPA-E grant for producing magnetic nanoparticles for permanent magnets. I decided to transition into this project despite my relative lack of interest in magnetism primarily due to the clean energy implications, and to my loyalty to Ami. This work is reported in Chapter 3 of this dissertation.

If there is any practical point to this preface other than being a self-promoting memoir, it's that it serves as my stark justification for the heavy emphasis on the clean energy applications of this work. This has always been my reason for all that I've done in my young career – a foolish ambition to make a difference, to change lives, and to do meaningful work that may one day change the world.

ACKNOWLEDGEMENTS

The work presented in this dissertation would not have been possible if not for the administrators, collaborators, teachers, and supporters from whom I've learned from and grown with.

First and foremost, I would like to thank my advisor, Professor Ami Berkowitz, for his immeasurable contributions to my education and career. Ami is my mentor, advisor, and collaborator, and I consider him to be the greatest teacher that I've ever had. He has refined all of my experimental practices, influencing my ability to achieve success in research. The most important things that Ami has taught me were done by example – confidence, passion, determination, and an unwillingness to settle for mediocrity. I carry with me these lessons for the rest of life.

I would also like to express my deepest appreciation for Professor Sungho Jin for giving me my early opportunities at UCSD. He believed in me enough to connect me with a project, an advisor, and a source of funding. I will not forget that without his influence, none of this would have been set in motion.

This appreciation is extended to the other great professors who have taught me at UCSD, especially those who serve on my thesis committee: Professor Renkun Chen, Professor Eric Fullerton, and Professor Prab Bandaru. Each of these professors have at least on one occasion welcomed me into their office for consultation and/or advice.

Professor Ken Vecchio, Wayne Neilson, Dr. Chulmin (Edward) Choi, and Dr. Li-Han Chen have all taught me miscellaneous methods in research and experimentation. Ray Descoteaux of CMRR has taught me so much that I often refer to him as "Professor

Ray". The useful discussions that I've had with Dr. Fred Spada are priceless and have expanded the limits of my knowledge and wisdom. I appreciate infinitely from these gentlemen their willingness to help me learn.

Furthermore, I wish to acknowledge those who have taught me how to operate the equipment used for my graduate research: Ryan Anderson for SEM/EDX, Maribel Montero for XRF, Phuong Dau, Honghan Fei, and Sanwen (Vince) Chen for PXRD, Andrea Potocny for DLS, Tae Kyoung Kim for UV-VIS spectroscopy, and Professor Dave Smith and the microscopy team at ASU for high resolution electron microscopy.

I would also like to extend this appreciation to the helpful administrators who have aided me throughout my time at CMRR: Betty Manoulian, Kevin Wong, Lauren Coleman, Julie Matsuda, Kelly Huang, Gabby Tshamjyan, Jonathan Chae, and especially Iris Villanueva.

I am very grateful to have worked with the brightest: Jeonghoon (David) Kim, my first collaborator who helped me to adapt to graduate work at UCSD, Chu (Charlie) Yinghao, Jaeyun Moon, Chin Hung (Isaac) Liu, and especially Young Jin Kim, who constantly challenges me to improve the quality of my work.

For other collaborators of the work presented in this dissertation, the following is acknowledged: Chapter 2, in part, is a reprint of the material as it appears in Nanotechnology, Volume 23, 2012, Phi-Khanh Nguyen, Kyu Hyoung Lee, Jaeyun Moon, Sang Il Kim, Kyunghan Ahn, Li-Han Chen, Sang Mok Lee, Renkun Chen, Sungho Jin, and Ami E. Berkowitz. Chapter 3, in part, is a reprint of the material as it appears in Journal of Applied Physics, Volume 115, 2014, and IEEE Transactions on Magnetics, Volume 49,

2013, Phi-Khanh Nguyen, Sungho Jin, and Ami E. Berkowitz. The dissertation author was the primary investigator and author of these papers.

As the only student in my group, I give special thanks to the students and post-docs of CMRR who have made my time here special: Sohini Manna, Nasim Eibagi, Liane Matthes, Jimmy Kan, Jonathan Sapan, Sergio Montoya, Richard Choi, Vojta Uhlir, Matthias Gottwald, Cihan Kuru, Pablo Salas-Mendez, Tang (Tony) Zhengqiang, Young Woo Seo, Alex Phan, Chuanwei (John Wayne) Zhang, Youyi Fu, and, of course, Benjamin Suen.

Lastly, I am forever thankful for the love and support of my truly amazing family: my mother who has worked tirelessly after fleeing a war-torn nation for the sake of my future, my father who has instilled in me a passion for science while allowing me the freedom to pursue my own interests, my brothers, Khanh and Tam, who have always made me feel smart and special, and finally, my life partner and fiancée, Victoria, with whom I've walked this journey through the long nights, early mornings, erratic hours, successes, and failures – she is forever the co-author to the greatest things I'll ever do.

VITA

2015	Doctor of Philosophy, University of California, San Diego
2012	Master of Science, University of California, San Diego
2010	Bachelor of Science, Rutgers University, New Brunswick/Piscataway
2009	Summer Intern, University of California, Berkeley
2009	Study Abroad, University of Manchester, United Kingdom
2008	Summer Intern, University of California, Riverside

LIST OF PUBLICATIONS

P.-K. Nguyen, S. Jin, A. E. Berkowitz. "MnBi Particles with High Energy Density made by Spark Erosion". Journal of Applied Physics, 115, 17A756. (2014)

P.-K. Nguyen, S Jin, A. E. Berkowitz. "Unexpected Domain Behavior in LTP-MnBi". IEEE Transactions on Magnetics, 49 3387-3390. (2013)

P.-K. Nguyen, K. H. Lee, J. Moon, S. I. Kim, K. A. Ahn, L. H. Chen, S. M Lee, R. K. Chen, S. Jin, A. E. Berkowitz. "Spark erosion: a high production rate method for producing $Bi_{0.5}Sb_{1.5}Te_3$ nanoparticles with enhanced thermoelectric performance". Nanotechnology 23 415604-415711. (2012)

J. Seidel, W. Luo, S. J. Suresha, **P.-K. Nguyen**, A. S. Lee, S. Y. Kim, C. H Yang, S. J. Pennycook, S. T. Pantelides, J. F. Scott, R. Ramesh. "Prominent electrochromism through vacancy-order melting in a complex oxide". Nature Communications, 3:799 doi: 10.1038/ncomms1799. (2012)

ABSTRACT OF THE DISSERTATION

Development of Thermoelectric and Permanent Magnet Nanoparticles
for Clean Energy Applications

by

Phi-Khanh Nguyen

Doctor of Philosophy in Materials Science and Engineering

University of California, San Diego, 2015

Professor Ami E. Berkowitz, Co-Chair
Professor Sungho Jin, Co-Chair

The global trend towards energy efficiency and environmental sustainability has generated a strong demand for clean energy technologies. Among the many energy solutions, the work in this dissertation contributes to two strategic goals: the reduction of fuel consumption in the transportation sector, and the increase of domestic wind power capacity. The key barriers to achieving these goals are materials challenges. Automobiles can be made more efficient by thermoelectric conversion of waste heat from the engine into electricity that can be used to power electrical components in the vehicle. Vehicles

can forego petroleum fuel altogether by using electric or hybrid motors. Unfortunately, the conversion efficiency of current thermoelectric technology is too low to be considered economically feasible, and the permanent magnets used in electric vehicle motors and wind turbine generators require critical rare-earth elements that are economically unstable (often referred to as the "rare-earth crisis"). In order to combat these challenges, a "spark erosion" technique was utilized for producing nanoparticles that improve thermoelectric efficiency and contribute to the development of electromotors that do not require rare-earths.

In Chapter 2 of this dissertation, I describe the utilization of spark erosion for producing high-quality thermoelectric nanoparticles at a remarkably high rate and with enhanced thermoelectric properties. The technique was employed to synthesize p-type $Bi_{0.5}Sb_{1.5}Te_3$ (BST) and n-type skutterudite nanoparticles, using a relatively small laboratory apparatus, with low energy consumption. The compacted BST nanocomposite samples made from these nanoparticles exhibit a well-defined, 20 – 50 nm size nanograin microstructure, and show an enhanced Figure of merit, ZT, of 1.36 at 360 K due to a reduction in lattice thermal conductivity. The skutterudite nanocomposites also show reduced thermal conductivity but still require enhancement in the thermoelectric power factor. Such a technique is essential for providing inexpensive, oxidation-free nanoparticles required for fabricating high performance thermoelectric devices for power generation from waste heat, and for refrigeration.

We have investigated the spark erosion of MnBi, a promising rare-earth-free permanent magnet, and have determined that spark erosion provides the best approach for producing MnBi particles. The low-temperature phase of MnBi (LTP-MnBi) is an

attractive rare-earth free permanent magnet material due it its high uniaxial magnetocrystalline anisotropy, which produces an unusually high coercivity at the elevated temperatures required for motor and generators. However, due to the peritectic Mn-Bi phase diagram and the slow interdiffusion of Mn and Bi below the 350°C phase change temperature, bulk samples of LTP-MnBi with high saturation magnetization (M_S) have been difficult to achieve.

In Chapter 3, we describe the successful formation of high-purity bulk LTP-MnBi ingots and spark erosion of this material to produce single-domain particles of MnBi at an unprecedented rate. The bulk ingots have M_S > 90 wt % of LTP-MnBi, and are formed by chill-casting and by vacuum-annealing of arc-melted ingots. The as-prepared powder then consists of amorphous, crystalline, and superparamagnetic particles, mostly as porous aggregates. The major fraction of the powder consists of 20-30 nm particles. A short anneal crystallizes the amorphous particles producing a high moment, albeit with H_C of only a few kOe. If lightly milled, the agglomerates are broken up and yield an H_C of 1 T and a maximum energy product of 3.0 MGOe.

The particles can be further engineered through milling, annealing, and/or solution processing in order to produce unique properties that hold promise to achieving the first bulk permanent magnet that utilizes the exchange-spring principle. In addition, we have found that due to the amorphous component of the spark-eroded powder, a cold compact can be magnetically oriented by crystallizing in a magnetic field. This crystallographic alignment is necessary for further improvement of the magnet energy density.

CHAPTER 1: INTRODUCTION

1.1 Clean Energy

Renewable energy technologies have become increasingly popular, more recently due to the 2000's oil crisis that saw rise in gas prices throughout the United States. The acceptance of climate change has also bolstered these technologies, promoting the term "clean" energy, indicating that the source of energy does not contribute to CO_2 emissions, the primary contributor to the greenhouse effect. The benefits to renewable energy are environmental-friendliness, sustainability, and domestic energy security.

While popularized by cultural and political forces, renewable/clean energy has long been considered a long-term plan for gradually moving away from fossil fuels.

	Coal	Natural Gas*	Crude Oil	Nuclear	Renewables	Total Production (Quadrillion Btu)
2000	31.9%	31.2%	17.3%	11.0%	8.6%	71.3
2001	32.8%	31.7%	17.1%	11.2%	7.2%	71.7
2002	32.1%	31.0%	17.2%	11.5%	8.1%	70.7
2003	31.6%	31.4%	17.1%	11.4%	8.5%	69.9
2004	32.5%	30.7%	16.4%	11.7%	8.6%	70.2
2005	33.4%	30.1%	15.8%	11.8%	9.0%	69.4
2006	33.6%	30.2%	15.2%	11.6%	9.3%	70.7
2007	32.9%	31.1%	15.0%	11.8%	9.1%	71.4
2008	32.6%	31.6%	14.5%	11.5%	9.9%	73.2
2009	29.8%	32.6%	15.6%	11.5%	10.5%	72.7
2010	29.5%	32.9%	15.5%	11.3%	10.9%	74.8
2011	28.5%	33.8%	15.3%	10.6%	11.8%	78.0
2012	26.1%	35.2%	17.4%	10.2%	11.2%	79.2
2013	24.7%	34.6%	19.3%	10.1%	11.2%	81.8

Figure 1.1 Historic trend of U.S. energy production by energy source.[1] Trends show a continuous rise in renewable energy and decline of coal energy.

Historic trends for the production of energy in the United States are shown in Figure 1.1 for various energy sources.[1] It can be seen here that in the last decade, renewables are the only energy sources that continuously grow. Coal continuously drops due to economic competition from natural gas, which gives off fewer emissions.[2] Due to similar economic forces, the price of crude oil has dropped but has since been rebounding (at the time of writing this dissertation, the price of gas is half of what is was when I started my Ph.D. research in 2010). Nuclear energy has fallen overall due to the closure of 48 nuclear plants in Japan after the Fukushima Daiichi nuclear disaster of 2011.[3]

The continual rise of renewable energy in the U.S. is broken down by source in Figure 1.2.[1] The *nameplate* capacity indicates the total of the manufacturers' specifications on the amount of energy a system is capable of producing. While the

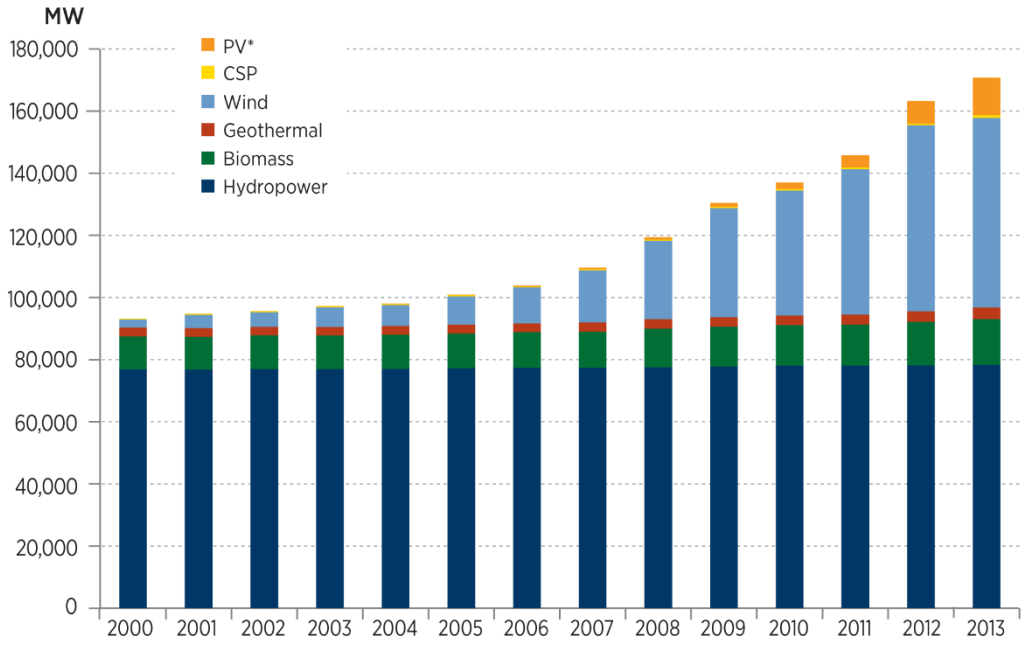

Figure 1.2 Historic trend of U.S. renewable electricity nameplate capacity by source.[1] Trends show a major increase in wind energy, minor increase in solar energy, and relatively no change in other renewable energy sources.

capacity of most renewable sources remains unchanged, wind energy has grown significantly due to technology maturity, feasibility, geographical favorability, and tax incentives.[4] For similar reasons, solar energy is also on the rise. The increase in wind energy capacity requires the use of electric generators. The next section will discuss the scarcity of materials used in motors/generators and how the work in this dissertation addresses this sustainability issue in order to assure an energy-secure future that allows for increased wind generation capability.

The Sankey diagram of energy consumption and application in the U.S. in 2013 is shown in Figure 1.3.[5] This estimation is made by Lawrence Livermore National Laboratory in conjunction with the Department of Energy every year and is widely used as the standard for energy calculations. There are two key points to extract from this figure: 1) petroleum is the largest source of energy in the U.S., and 2) over half of the energy available is wasted.

Since transportation is perhaps the most crucial component to the U.S. economy, the heavy use of petroleum should come as no surprise. Wasted energy, however, is a key focus of the work in this dissertation. In order to improve energy efficiency in the transportation sector, vehicle manufacturers are aiming for better fuel-efficiency. One mode of improvement is by waste-heat harvesting using thermoelectric (TE) devices. As will be discussed in Chapter 2, such devices convert heat into electricity. When combined with vehicles, the wasted heat can be converted into electricity for use in various

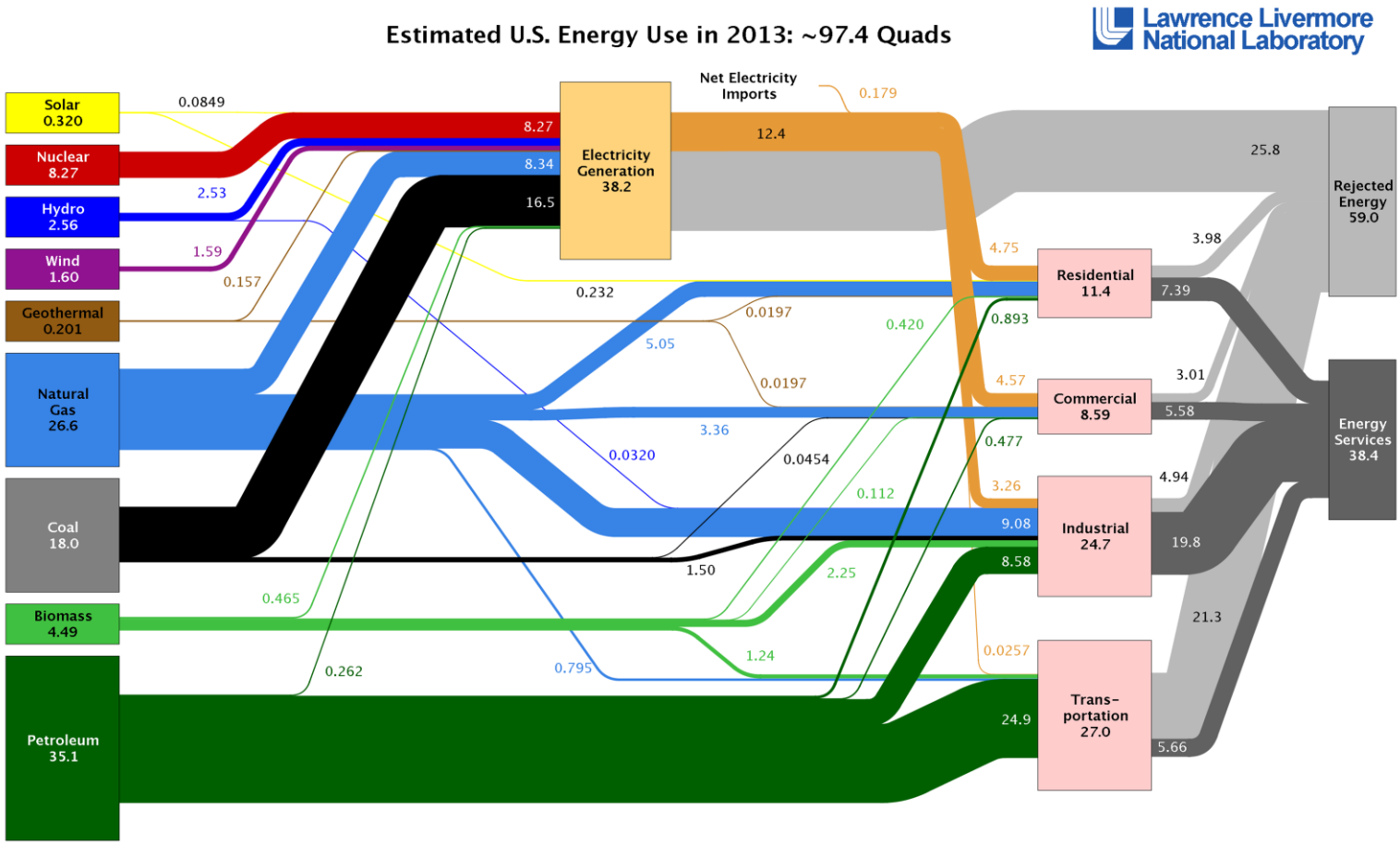

Figure 1.3 Estimated U.S. Energy Use in 2013 by source and sector as provided by Lawrence Livermore National Laboratory.[5] The total estimated usage of 97.4 Quads shows 60.5% wasted energy and 36% energy produced by petroleum. 27.7% of energy consumed in the U.S. is used for transportation.

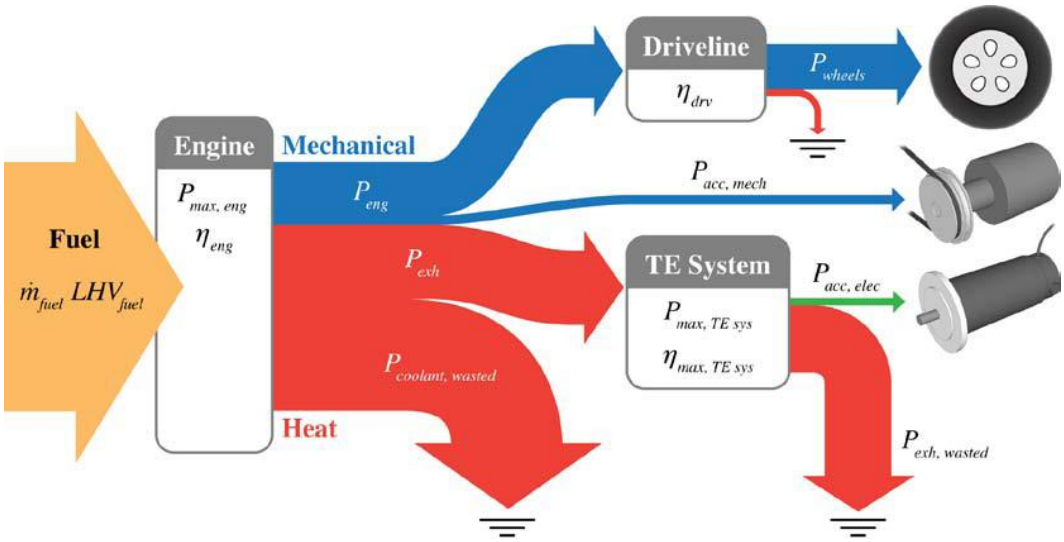

Figure 1.4 Energy diagram for vehicle system with embedded thermoelectrics. A thermoelectric system converts some of the waste heat produced by the engine into electricity that can be used for several components within the vehicle.[6]

electrical components. The diagram in Figure 1.4 shows a model for waste-heat harvesting of a vehicle system by using the efficiencies of existing motors and thermoelectric heat conversion devices.[6] In order for TE devices to be economically competitive, their conversion efficiencies need to be enhanced. This is the focus of the work in Chapter 2 of this dissertation. Another way to reduce fuel consumption is by using hybrid- or all-electric vehicles. Like in wind turbine generators, such vehicles require the permanent magnet components that will be discussed in Chapter 3.

1.2 Sustainability and the Rare-Earth Crisis

The increasing demand for wind turbine generators and hybrid/electric vehicles requires strong permanent magnets for the mechanical-electrical energy conversion. This has led to a large rise in the sales of the magnets that are most suitable for this application (Figure 1.5).[7] However, such magnets require rare-earth elements, of which the supply is dominated by other countries, predominantly China (Figure 1.6).[8] In 2009, a large spike in costs for rare-earths supplied by China brought this to international attention. Prices have since relaxed but remain relatively high (Figure 1.7).[8] This economic instability has since been deemed the "rare-earth crisis", driven by cost instabilities due to the monopoly of rare-earth element supply by China.

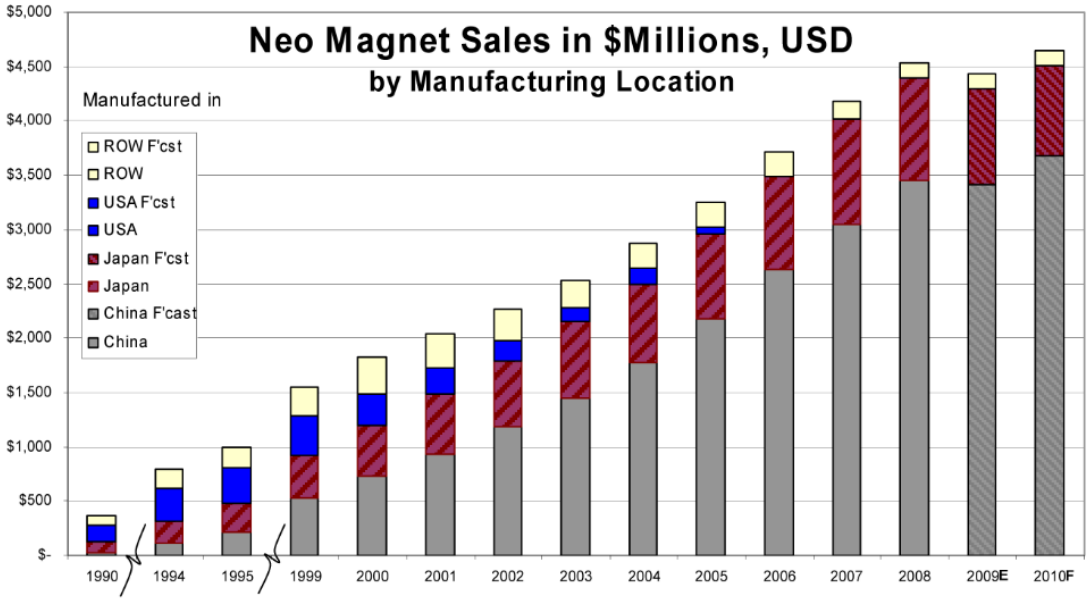

Figure 1.5 Historic trend of Nd-based magnet sales by manufacturing location showing an increasing dominance of Chinese-manufactured magnets and the lack of magnets made in U.S.[7] (© Arnold Magnetic Technologies)

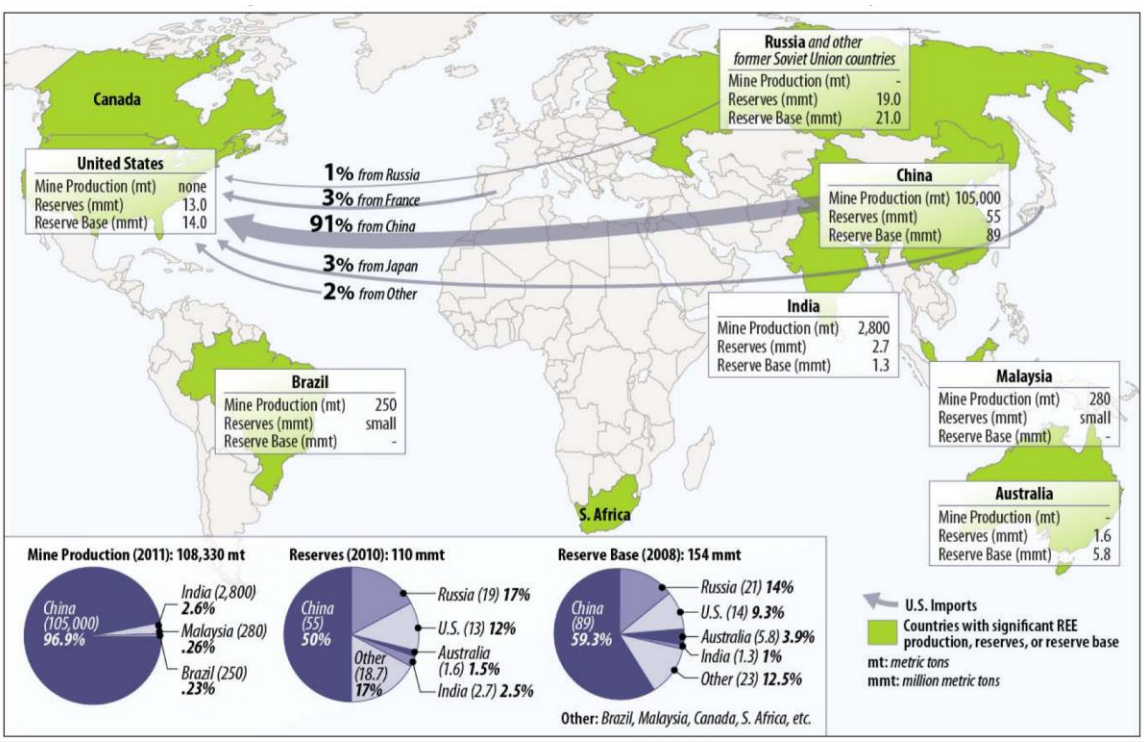

Figure 1.6 Rare Earth Elements: World Production, Reserves, and U.S. Imports. [8]

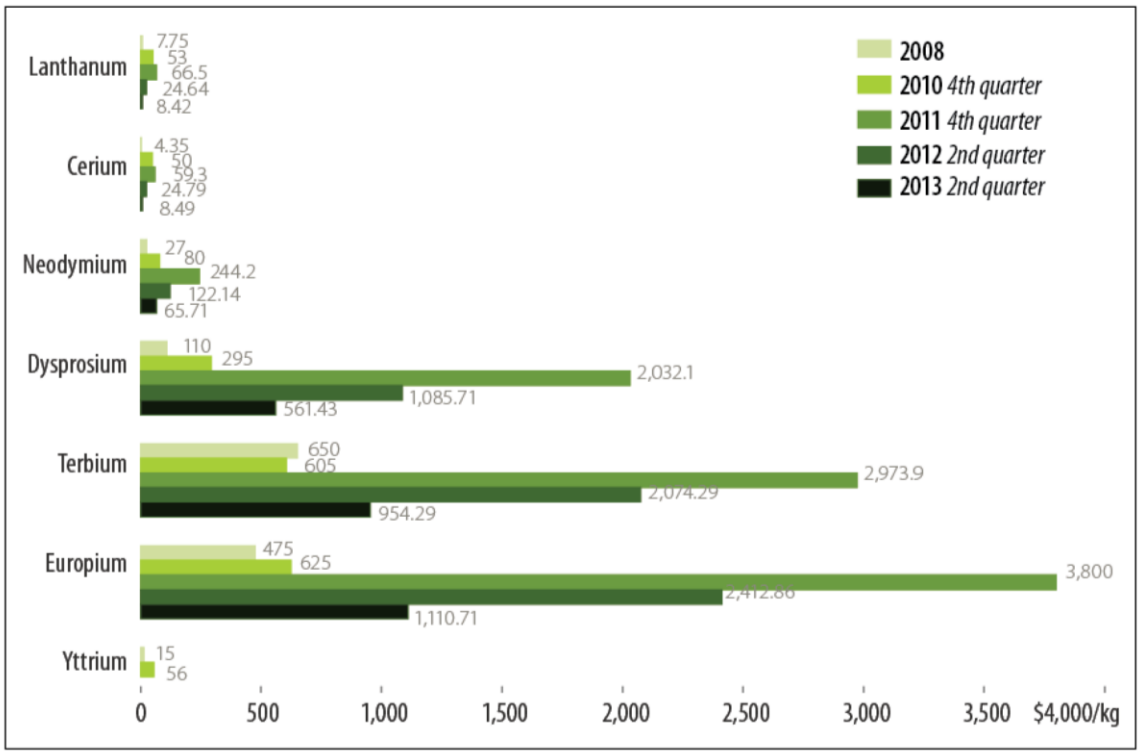

Figure 1.7 Selected Rare Earth Oxide Prices, 2008-2013.[8]

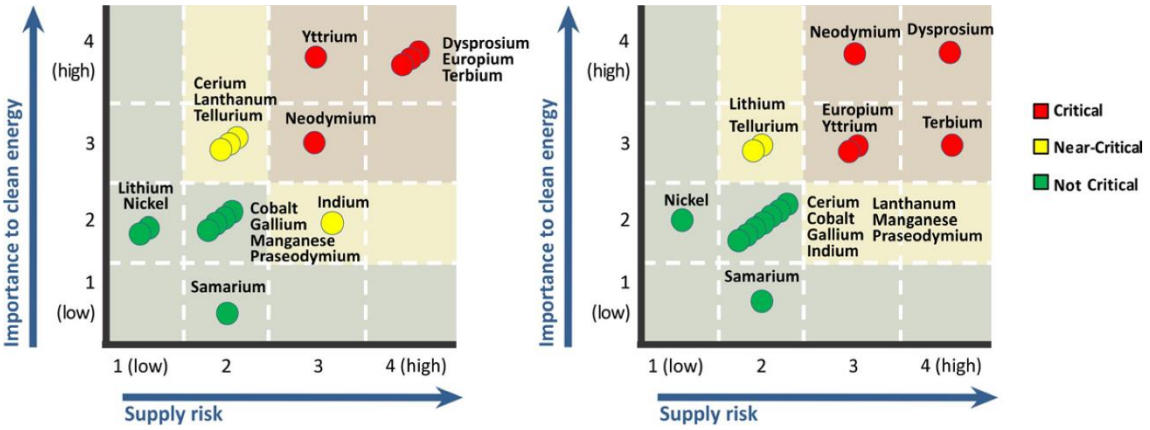

Figure 1.8 Department of Energy Strategic and Critical Elements Chart showing importance to clean energy and supply risk. Dysprosium is the single most critical element.[9]

For these reasons, the U.S. Department of Energy has declared these rare-earth elements to be most critical to the domestic clean energy strategy (Figure 1.8).[9] The most critical element is dysprosium, which is mainly used for the stabilization of Nd-Fe-B permanent magnets at the elevated temperature at which they operate for motors and generators.[10] Because of this, the rare-earth crisis is often referred to simply as a "dysprosium crisis". Chapter 3 will discuss the development of rare-earth-free permanent magnets (REFPM) in order to promote sustainable solutions that do not require these critical elements.

1.4 References

[1] U.S. Department of Energy, "2013 Renewable Energy Data Book". NREL, DOE/GO-102014-4491 (2014).

[2] Center for Climate and Energy Solutions Website. Retrieved February 2015 from "http://www.c2es.org/energy/source/coal".

[3] M. Schneider and A. Froggatt, "The World Nuclear Industry Status Report 2014", Mycle Schneider Consulting (2014).

[4] U.S. Department of Energy, "2013 Wind Technologies Martket Report". DOE/GO-102014-4459 (2014).

[5] Lawrence Livermore National Laboratory, "https://flowcharts.llnl.gov", U.S. Department of Energy, LLNL-MI-410527 (2014)

[6] National Renewable Energy Laboratory, "Feasibility of Thermoelectrics for Waste Heat Recovery in Conventional Vehicles", NREL/TP-540-44247 (2009).

[7] S. Constantinides, "The Magnetic Material Challenge", ARPA-E Workshop Presentation, Rare Earth and Critical Materials, Arlington, VA (2010).

[8] M. Humphries, "Rare Earth Elements:The Global Supply Chain", Congressional Research Service, R41347(2013).

[9] U.S. Department of Energy, "U.S. Department of Energy Critical Materials Strategy December 2011", DOE/PI-0009 (2012).

[10] O. Gutfleisch, M. A. Willard, E. Bruck, C. H. Chen, S. G. Sankar, and J. P. Liu, "Magnetic materials and devices for the 21st century: stronger, lighter, and more energy efficient", Adv. Mater. **23**, 821-842 (2011).

CHAPTER 2: THERMOELECTRICS

2.1 Background

2.1.1 Principles

Thermoelectric materials can directly convert waste heat from manufacturing processes, building heating systems, automobile exhausts, solar and geothermal sources, etc., into electrical power by the Seebeck effect, in which temperature differences produce electrical power.[1] Conversely, the Peltier effect uses electricity for refrigeration.[2]

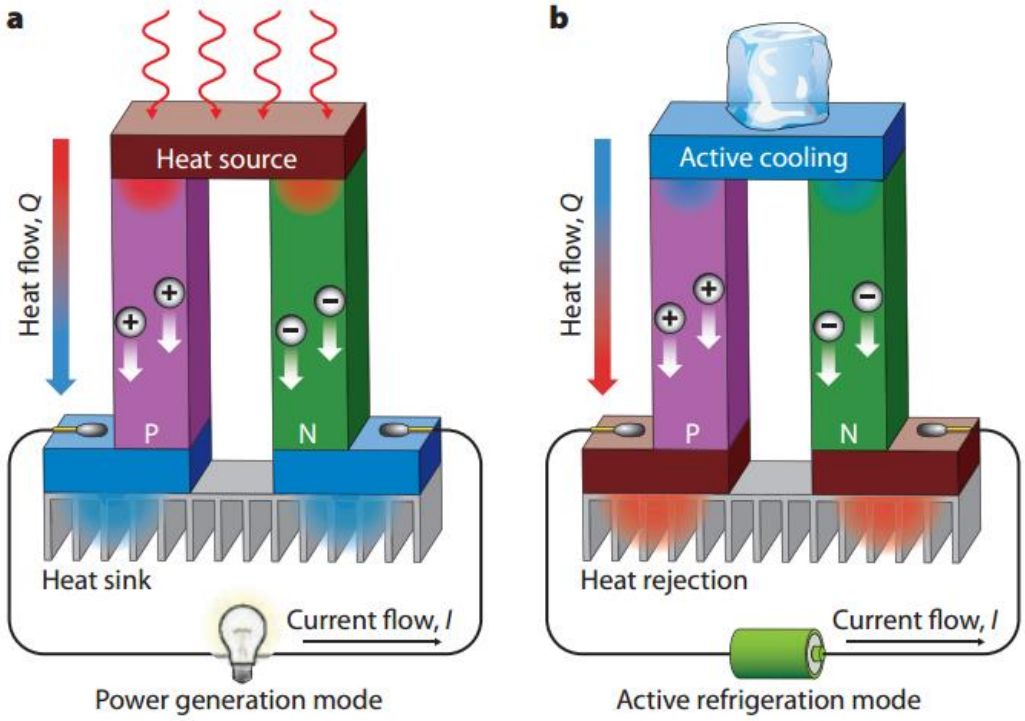

Figure 2.1 Schematic illustrations of a thermoelectric device module for (a) power generation (Seebeck effect) and (b) active refrigeration (Peltier effect).[3] (© Tokyo Institute of Technology)

The Seebeck effect relies on the underlying principle of charge carrier diffusion. In most metals, for example, electrons are constantly in motion throughout the conductive material. Without a bias, this motion is random, and so the net potential gradient is zero. When there is a temperature gradient, high-energy electrons diffuse towards the cold end faster than lower energy electrons diffuse to the hot end. This imbalance forms the potential difference that is utilized for thermoelectric conversion. The relative voltage change per temperature difference defines the Seebeck coefficient, S (sometimes denoted α), which is negative for most metals. Hence, in doped semiconductors where electrons are the majority charge carriers (n-type), the Seebeck coefficient is also negative. Likewise, when holes are the majority charge carriers (p-type), S is positive.

A semiconductor thermoelectric device module is depicted in Figure 2.1 showing the use of the Seebeck and Peltier effects for thermoelectric power generation and refrigeration, respectively. For both modes, both p- and n-type semiconductors are required for the continuous flow of charge carriers. For power generation (Figure 2.1a), a a heat source repels the charge carriers (attracts electrons in a p-type semiconductor and repels electrons in an n-type). Since the magnitude is dependent on the temperature difference, a heat sink maximizes the temperature gradient by reducing the temperature of the cold side. For refrigeration (Figure 2.1b), the current flow forces the charge carriers to create a temperature gradient, and heat from the hot end is dissipated in order to actively cool on the cold end.

At present, thermoelectric phenomena has only limited usage for these applications. The principal reason is the very low conversion efficiency of thermoelectric devices as compared to the corresponding mechanical systems.

2.1.2 ZT Figure of Merit

The ideal thermoelectric material should have a high Seebeck coefficient but also a high electrical conductivity (low resistivity) in order to reduce joule heating. This, along with a low thermal conductivity, would aid to maximize the temperature gradient. A dimensionless figure of merit, ZT, measures the efficiency of thermoelectric materials:

$$ZT = \frac{S^2\sigma T}{\kappa} = \frac{S^2\sigma T}{\kappa_L + \kappa_e} \tag{3.1}$$

…where T is the absolute temperature, S the Seebeck coefficient, σ the electrical conductivity, and κ the thermal conductivity that is composed of the sum of κ_L, the lattice thermal conductivity, and κ_e, the electronic thermal conductivity.[1] $S^2\sigma$ is called the

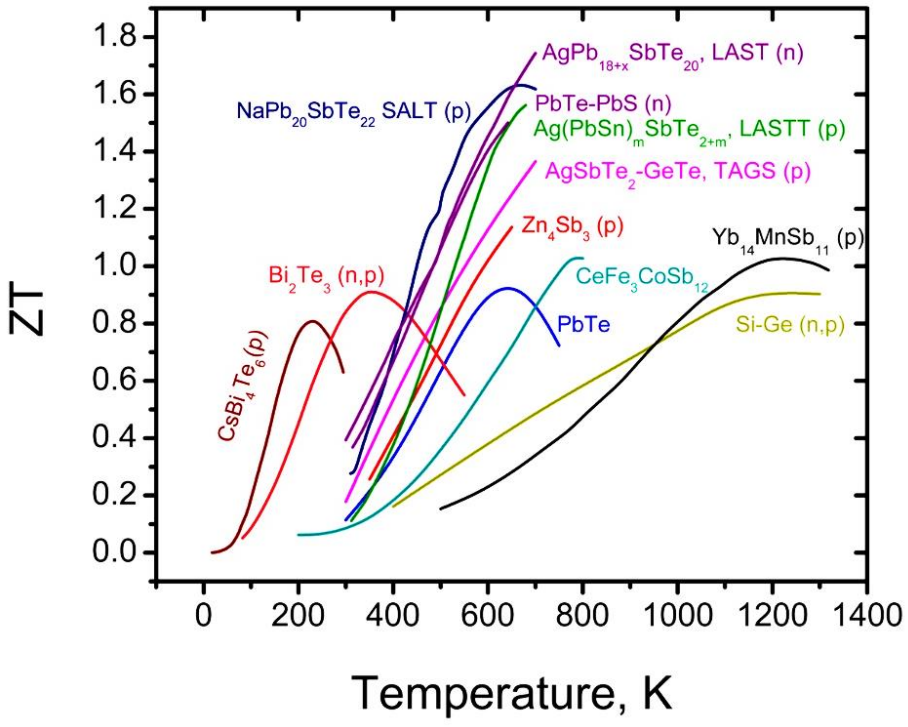

Figure 2.2 Figure of merit, ZT, versus temperature for several conventional p- and n-type thermoelectric systems.[4]

power factor, the measure of the materials ability to generate energy without considering inefficiencies due to high thermal conductivity. In conventional bulk semiconductor materials, the parameters S, σ, and κ_e are interdependent, and thus the best bulk thermoelectric materials have possessed $ZT \approx 1$ for over 40 years (Figure 2.2).[4] $ZT \approx 4$ is required for thermoelectrics to be competitive with current refrigeration technology.[2] As can be seen in Figure 2.2, the best thermoelectric materials also use elements that are rare, expensive, or toxic (tellurium is deemed a near-critical element in Figure 1.8).

The Seebeck coefficient and electrical conductivity are both strongly dependent on the charge carrier concentration. The Seebeck coefficient, however, decreases with increasing carrier concentration, while the electrical conductivity increases. There is

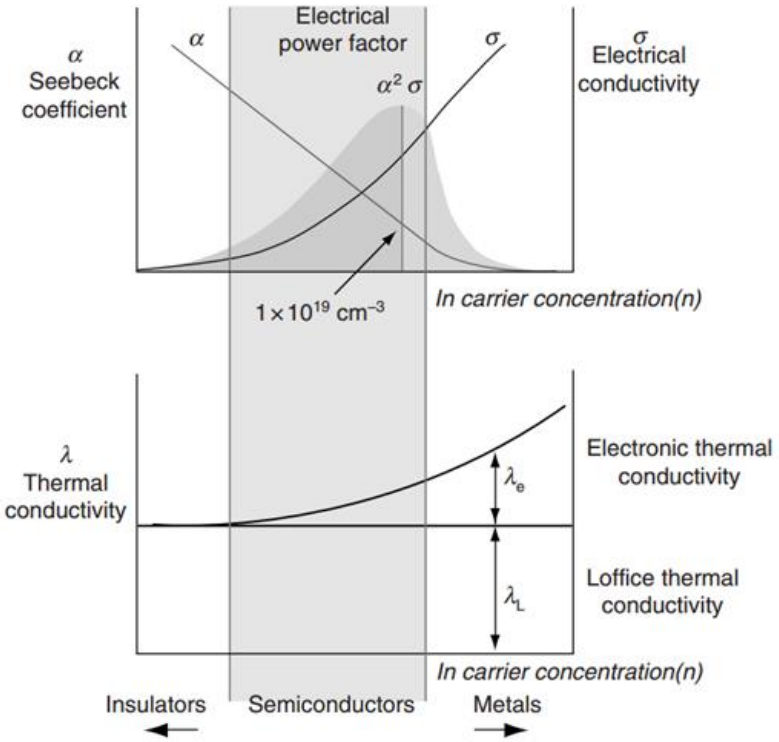

Figure 2.3 The Seebeck coefficient, electrical conductivity, and electronic and lattice thermal conductivities, versus carrier concentration showing an optimal electrical power factor when the carrier concentration is 1×10^{19} cm^{-3}.[2] (© CRC Press)

therefore an optimal carrier concentration for a maximum power factor in conventional thermoelectric materials. This relationship and the optimal carrier concentration of 1×10^{19} cm^{-3} is shown in Figure 2.2. It is for this reason that semiconductors make the best thermoelectric materials – the optimal charge carrier concentration is achieved in semiconductors.

Since κ_e is also dependent on the carrier concentration, the only independent parameter is κ_L. Thermal conductivity through the lattice is carried by phonons, which are quantized vibrational modes of the crystal lattice and thus have a group velocity and mean free length. Reduction of κ_L depends on the scattering of phonons mainly by interaction with lattice defects, impurities, grain boundaries, or other phonons. For this reason, the best thermoelectric alloys in Figure 2.2 contain large atoms.

In order to further reduce ZT, Dresselhaus *et al* theorized that quantum confinement could lead to thermoelectrically favorable effects: enhancement of the density of states near the Fermi energy leading to an enhancement of the Seebeck coefficient, increased carrier mobilities at a given carrier concentration, different temperature dependences of the transport properties and intrinsic carrier excitations in

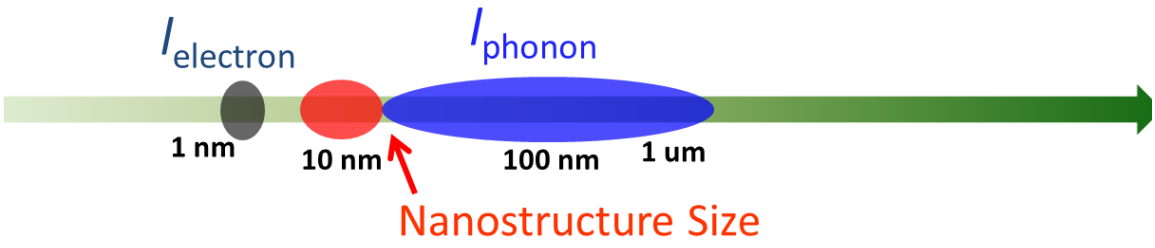

Figure 2.4 By creating nanostructures of a size smaller than the phonon mean free length but larger than that of the electron, phonon-boundary scattering can be increased while preserving electron mobility.

low dimensional systems relative to 3D systems, and increased boundary scattering of phonons at the barrier-well interfaces, while effectively preserving carrier mobilities by exploiting the different length scales for phonon and electron scattering.[5] Since this report, the field of thermoelectrics has progressed enormously as evidenced by numerous reports showing enhanced ZT in nanostructured materials[6,7] such as superlattices of Bi_2Te_3/Sb_2Te_3[8] and PbSeTe/PbTe[9], nanowires[10,11], and in bulk materials with complex structures[12], such as lead antimony silver telluride (LAST)[13] and skutterudites[14]. It is now recognized that the enhanced ZT values in these nano- or complex-structured materials are mainly due to reduced lattice thermal conductivity produced by stronger phonon-boundary scattering in nanostructures.[6,7,5] This approach has been shown to be quite generic provided that the characteristic nanostructure sizes are smaller than phonon mean free path in corresponding bulk materials, which is usually dictated by *Umklapp* scattering and alloy scattering.

Over the last few years, in search for a more scalable route for making thermoelectric nanostructures, a new bulk-nanostructuring approach has been developed and has achieved very notable success.[5,7] This new approach is based on the production of bulk thermoelectric composites from powders containing nanoparticles and/or high density of grain boundaries. The key idea of the nanocomposites is to utilize the high density of grain boundaries to scatter phonons without significantly adversely affecting the charge transport (Figure 2.4). The fabrication of various nanocomposite materials and their thermoelectric properties have been reported.[15-32]

2.1.3 Bulk Nanostructured Thermoelectrics

Among the reported bulk nanostructure thermoelectrics, the production methods of the starting thermoelectric powders containing nanoscale features can be generally categorized into two approaches: top-down[15,17,19,21-24,31,32] and bottom-up[25-30]. For example, Poudel *et al.* reported the fabrication of nanocomposite p-type $Bi_{0.5}Sb_{1.5}Te_3$ by ball-milling the bulk alloys for several hours to nanometer dimensions in inert environments and hot-pressing these nano-powders to produce the sintered compacts.[19] They have achieved a high ZT of 1.4 at 100°C. The same groups also reported similar ball-milling-hot pressing approach for a variety of thermoelectric materials, including n-type $Bi_2Te_{2.7}Se_{0.3}$[33], n- and p-type SiGe[17,32], n-type Si[24], among others. Another recently developed approach is melt-spinning ribbons of the appropriate alloy, hand-grinding them, and compacting them by spark plasma sintering (SPS).[21,22] A similarly high ZT of ~1.5 at 360 K was observed in these $(Bi,Sb)_2Te_3$ nanocomposites. The comprehensive characterization[21,34] of the samples prepared from the ball-milling and melt-spinning techniques demonstrated that the low κ_L and the enhanced ZT were due to the nanocrystalline domains present. An important economic advantage of hot-pressing nano-powders is the possibility of preparing net shapes without machining. Besides these 'top down' approaches, there have been a growing number of reports showing 'bottom-up' routes for producing Bi-Sb-Te nanostructures by solution processes[25-30]. The latter approach, although having a great potential for scalability, has yet to demonstrate a ZT higher than 0.5,{27,28] presumably due to the hindered charge transport or perhaps particle surface oxidation presented in solution processing.

Despite the very important successes of the various nano-bulk composite approaches, both the top-down and bottom-up methods have disadvantages. Though the bottom-up approach yields intriguing ZT, the yield of nano-powders for fabricating compacted samples is still relatively low, and in some cases, the powder fabrication process itself could be very energy-consuming, which implies high cost. Meanwhile, the potentially low-cost and scalable 'bottom-up' approaches address this issue, but have yet to demonstrate a ZT comparable to bulk materials. Therefore, a new technique capable of delivering both advantages would be extremely attractive. Such a technique would produce clean thermoelectric nanostructures at a significantly improved production rate, which would also lead to nanostructured bulk composites that demonstrate the high ZT achieved by the 'top down' approaches.

In this chapter, the spark erosion method has been optimized for the production of nanoparticles of thermoelectric materials. The resultant nanostructured compacts using spark-eroded $Bi_{0.5}Sb_{1.5}Te_3$ show a high ZT of 1.36 at 360 K, close to the ZT values on similar alloys prepared by other top-down techniques described above.[19,21] However, spark erosion offers very significant advantages over these other methods, particularly with respect to processing efficiency, rate of nano-powder production, and scale-up potential. Furthermore, since spark erosion requires no crucible, there is no contamination issue, and oxygen-free processing conditions are readily achieved. Compacts of $Ba_{0.3}Ni_{0.05}Co_{3.95}Sb_{12}$ have also been developed in the same manner and show promising results.

2.2 Experimental Procedures

2.2.1 Sample Preparation

High-purity (> 99.999%) Bi, Sb, and Te granules were weighed according to the composition of $Bi_{0.5}Sb_{1.5}Te_3$ and loaded into a quartz tube 20 mm in diameter. The tube was vacuum-sealed under 10^{-4} torr, and the contents were melted and homogeneously mixed in a rocking furnace for 10 h at 1073 K, then quenched to room temperature. For the zone-melting, the quenched ingot was directionally grown at a rate of 1 $K \cdot min^{-1}$. These ingots were used as spark erosion targets.

For sintered compacts of spark-eroded nanoparticles, disk-shaped bulk samples (10 mm in diameter and 13 mm in thickness) were fabricated from this powder by SPS under 90 MPa and at 450°C for 1 min in a vacuum. The sample densities for those compounds were about 97% of theoretical densities.

Ingots of $Ba_{0.3}Ni_{0.05}Co_{3.95}Sb_{12}$ were prepared by arc-melting and also used as spark erosion targets. The sintered compacts were fabricated by SPS under 50 or 40 MPa, at 650°C or 600°C, and for 5 or 10 min.

2.2.2 Thermoelectric Measurements & Characterization

Disks (10 mm in diameter and 1 mm in thickness) for thermal diffusivity measurement and bars (2 mm × 2 mm by × mm) for carrier transport properties and

Seebeck coefficient measurement were cut in the planes parallel and perpendicular to the press direction, respectively, so that all three parameters were measured in planes parallel to the press direction (See Figure 2.5).

The electrical conductivity and Seebeck coefficients were measured from 300 to 520 K (800 K for Section 2.2.2) by a four-point probe method using a thermoelectric measurement system (ZEM-3, ULVAC, Japan). The thermal conductivity values ($\kappa = \rho_s \bullet C_p \bullet \lambda$) were calculated from measurements taken separately; sample density (ρ_s), heat capacity (C_p) via thermal relaxation method, and thermal diffusivity (λ) were measured under vacuum by laser-flash method (TC-9000, ULVAC, Japan).

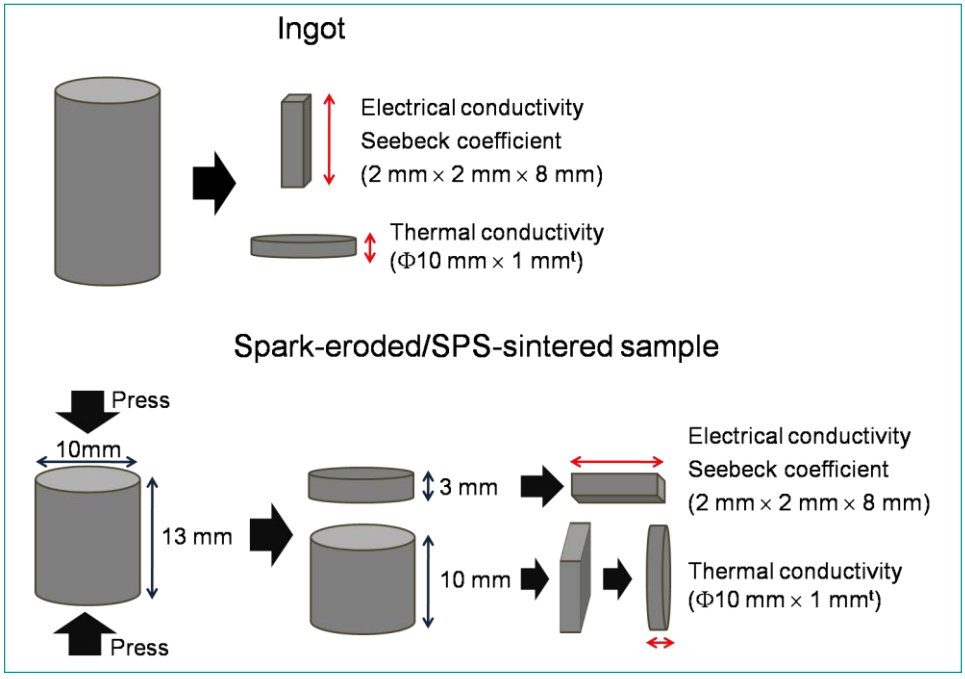

Figure 2.5 Thermoelectric measurement orientations as controlled by sample slicing directions, and the dimensions for the ingot samples and spark-eroded/SPS-sintered samples.

For powder x-ray diffraction, samples were prepared on a glass slide in air and bound by a mixture of Devcon® Duco Cement and acetone. X-ray diffraction patterns were measured in a Rigaku Geiger-flex unit with Co radiation in the Bragg-Brentano mode.

Elemental analysis was performed by direct current plasma emission spectroscopy (ASTM E 1097-07). Oxygen analysis was performed by inert gas fusion (ASTM E 1019-08)

2.3 Results and Discussion

2.3.1 Enhanced ZT in Bismuth Tellurides

The spark erosion nanoparticles' synthesis rate was approximately 135 grams/hour of clean non-oxidized $Bi_{0.5}Sb_{1.5}Te_3$ alloy. This high rate, with the high ZT to be shown, is remarkable considering the small laboratory cell dimension of only 10 cm in diameter (~1 liter in volume), indicating that scale-up to many tons/month with either larger cell diameter or parallel operation of multiple units is quite feasible. Remarkably, the energy consumption of the spark erosion process is estimated to be < 2.0 kWh per kg of $Bi_{0.5}Sb_{1.5}Te_3$ nanoparticles, based on the electrical power used by the pulse power mode operation.

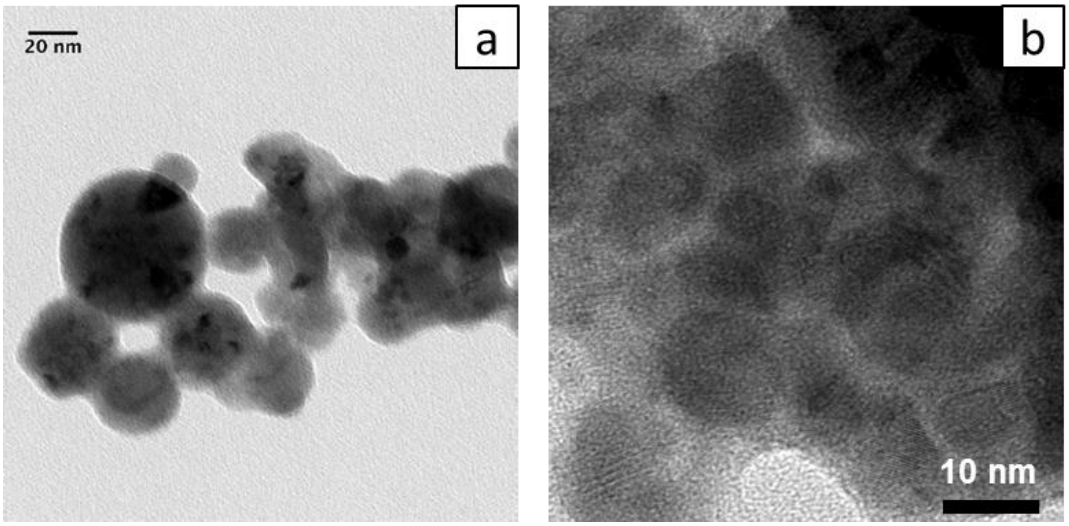

Figure 2.6 Spark-eroded $Bi_{0.5}Sb_{1.5}Te_3$ nanoparticles and nanostructures. (a) Bright field TEM of mostly spherical nanoparticles, showing smaller crystallized regions within the nanoparticles. (b) TEM micrograph of typical $Bi_{0.5}Sb_{1.5}Te_3$ nanoparticles. Lattice images indicate their single- or polycrystalline nature.

The TEM micrograph in Figure 2.6(a) shows some typical nanoparticles, illustrating their mostly spherical nature and nanoscale dimensions. Within these mostly spherical nanoparticles are smaller crystalline sub-grains. The spark-eroded $Bi_{0.5}Sb_{1.5}Te_3$ nanoparticles appear to be well crystallized as shown in Figure 2.6(b). The lattice images in some of the nanoparticles in the TEM microstructure of Figure 2.6(b) show their single crystal microstructure, while some of the larger particles are polycrystalline with a nanograin structure. Figure 2.7(a) shows nanoparticles clustered around larger spherical particles. These larger particles have a fine grain structure due to rapid quenching. The

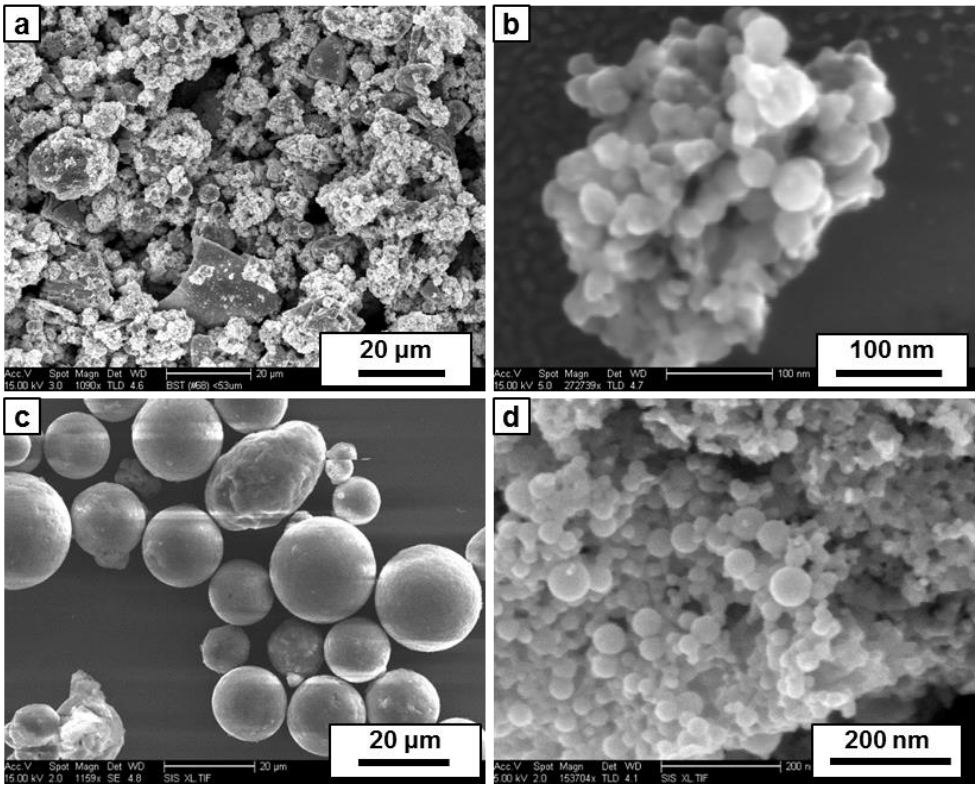

Figure 2.7 SEM images of spark-eroded $Bi_{0.5}Sb_{1.5}Te_3$ particles showing (a) the yield, which consists of a major fraction of nanoparticles and a minor fraction of micron-sized particles, albeit with fine structure (b) a cluster of nanoparticles, (c) micron-sized particles after nanoparticles are washed away, and (d) spherical nanoparticles.

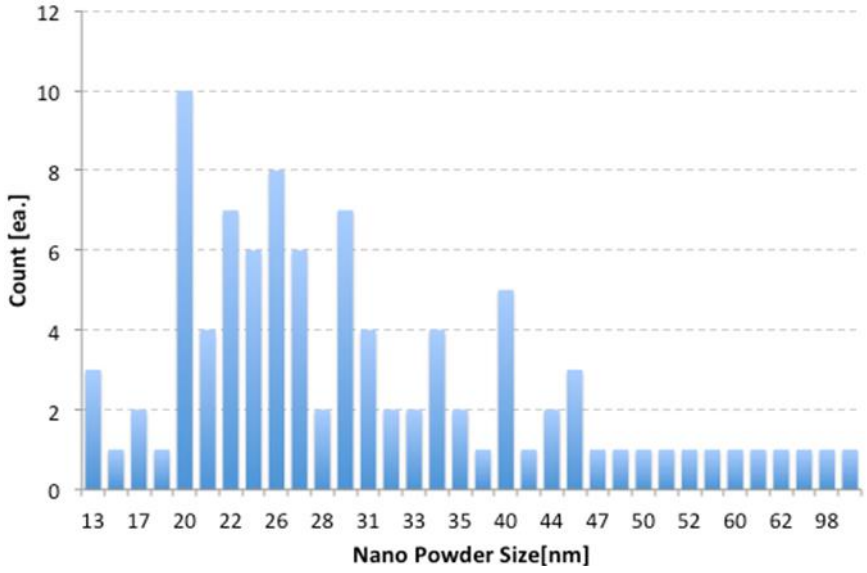

Figure 2.8 Particle size distribution of spark-eroded $Bi_{0.5}Sb_{1.5}Te_3$ based on TEM.

$Bi_{0.5}Sb_{1.5}Te_3$ nanoparticles synthesized by spark erosion exhibit relatively uniform diameters in the range of ~10 – 50 nm as determined by extensive TEM analysis with the average particle diameter being ~25 nm (Figure 2.8). Nevertheless, even further enhancement of ZT would result from increasing the fraction of smaller nanoparticles in Figure 2.7(b) and (d).

Figure 2.9 shows TEM micrographs of sections of the SPS compact made from the spark-eroded powders. Figure 2.9(a) shows that the mostly spherical nanoparticles are converted by the SPS into flat-sided parallelepiped grains. It is noteworthy that the sintering has not increased the grain size significantly over the original nanoparticles' dimensions. The higher magnification TEM in Figure 2.9(b) shows lattice fringes and indicates that many coherent grain boundaries are present in the sintered compacts.

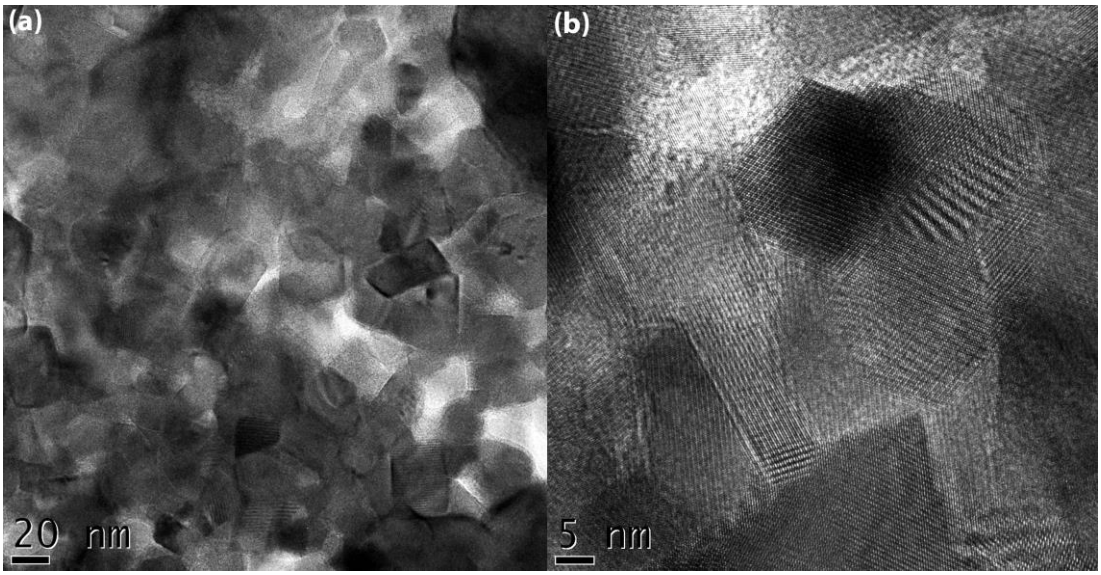

Figure 2.9 TEM micrographs of sections of the SPS sintered compacts made from spark-eroded $Bi_{0.5}Sb_{1.5}Te_3$ nanoparticles.

Figure 2.10 shows x-ray diffraction patterns of the starting bulk ingot, the < 53 μm spark-eroded powder, and the SPS compact made from the powder. Only lines of $Bi_{0.5}Sb_{1.5}Te_3$ are present (the shoulder on the 33 degree line of the powder is not present in the compact and remains an unexplained feature). The powder and compact patterns show random orientations. Random orientation of the crystallites' axes is necessary for insuring isotropy in thermoelectric devices, a very desirable feature.

The transport properties of the starting bulk alloy and the SPS compact are shown in Figure 2.11. Note that the properties of a sample of the zone-refined starting material may be strongly influenced by its structural anisotropy. To examine that issue, $Bi_{0.5}Sb_{1.5}Te_3$ ingots were milled at 200 rpm for 10 h in an N_2 atmosphere using a planetary ball-mill. The milled powder was sieved to obtain < 45 μm diameter particles. This powder was then compacted under the same conditions as the spark-eroded powder, and the transport properties were measured on disks and rods of the same sizes as used

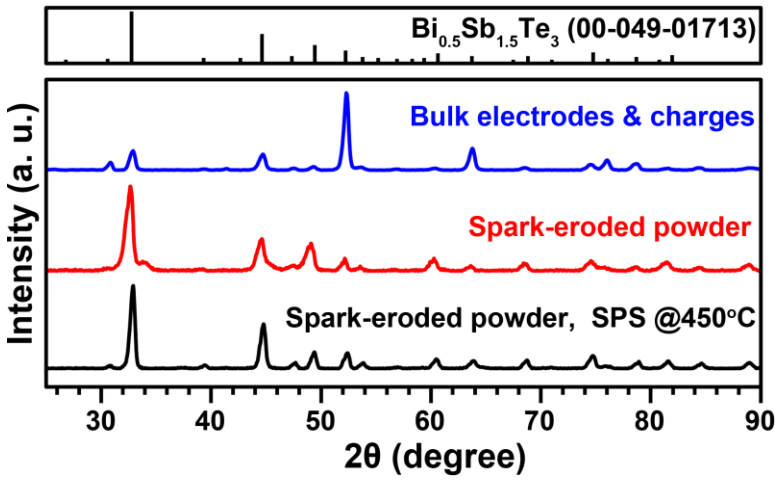

Figure 2.10 X-ray diffraction patterns with Co radiation of the bulk starting ingot, the < 53 μm spark-eroded powder, and the SPS compact made from that powder, compared to the standard $Bi_{0.5}Sb_{1.5}Te_3$ XRD pattern shown at the top.

for the starting material and the SPS-sintered compacts of spark-eroded powder. The properties were very similar to those of the sample of starting material.

As shown in Figure 2.11, the electrical conductivity of the spark-eroded samples is close to that of the starting bulk ingots (Figure 2.11a), while the Seebeck coefficient is lower below (higher above) 400 K than that of the ingot (Figure 2.11b). Overall, the power factor ($S^2\sigma$) values are comparable to that of the ingot below 360 K, and slightly higher above 360 K. The electrical transport properties of our spark-eroded samples are very similar to those of the $Bi_{0.5}Sb_{1.5}Te_3$ nanocomposite reported by Poudel *et al.*[19], showing the comparable quality of nanoparticles fabricated by spark erosion, *e.g.*, with minimal oxidation.

The thermal conductivity of the spark-eroded samples is significantly lower than that of the ingot (Figure 2.11d), which leads to a substantial increase in ZT over the entire temperature range of 300 – 520 K (Figure 2.11f). The peak ZT of 1.36 at 360 K, is

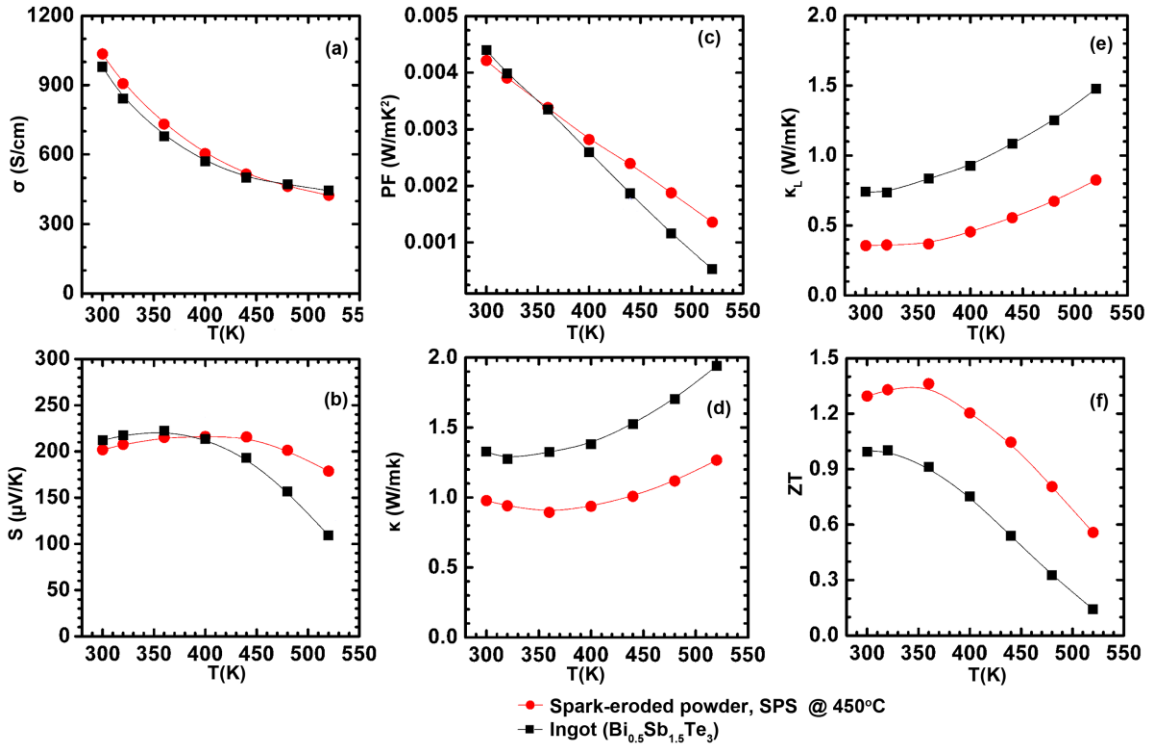

Figure 2.11 Thermoelectric properties of the starting bulk alloy, and the spark-eroded and SPS-sintered samples, as indicated by their respective markers. (a) electrical conductivity, (b) Seebeck coefficient, (c) power factor, (d) total thermal conductivity, (e) lattice thermal conductivity, (f) ZT value.

significantly higher than that of ~1.0 at 300 K for the bulk ingot, and is close to the highest reported ZT values in $Bi_{0.5}Sb_{1.5}Te_3$ nanocomposites fabricated by ball-milling as well as melt-spinning (1.4 at 100°C by Poudel *et al.*[19] and ~1.5 at 360 K by Xie *et al.*[21]). Above 360 K, ZT of the spark-eroded samples is decreasing with temperature, as a result of the decreasing electrical conductivity due to enhanced carrier-phonon scattering and the increasing thermal conductivity due to the bipolar thermal conduction.[12,21,34]

The enhanced ZT of the spark-eroded $Bi_{0.5}Sb_{1.5}Te_3$ nanoparticles after sintering is primarily due to the reduced thermal conductivity from 300 – 520 K, and is partially due

to the slightly increased power factor above 400 K. To elucidate this, we calculated the lattice thermal conductivity (κ_L) of both samples (Figure 2.11e) via the following relationship: $\kappa_L = \kappa - \kappa_e$, where the electronic thermal conductivity (κ_e) is estimated from the Wiedemann-Franz law, $\kappa_e = L \bullet T\sigma$, and the Lorenz number $L_0 = 2.0 \times 10^{-8}$ V^2/K^2, typical for a heavily-doped semiconductor.[22] Figure 2.11(e) shows that κ_L in the spark-eroded samples is reduced by about 50% over the entire temperature range, indicating stronger phonon scattering at nanograin interfaces, which is the main reason for the enhanced ZT.

It is worth noting that the calculated κ_L of our spark-eroded samples is very similar to those of nanocomposite Bi-Sb-Te samples reported in Refs. 19 and 21 if the same Lorenz number is used (Figure 2.12), indicating similar phonon and charge transport behaviour, presumably due to the similar microstructures. Note that the

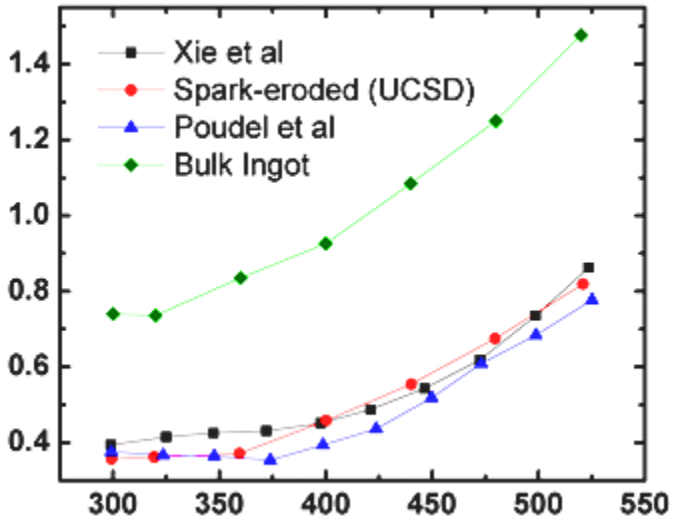

Figure 2.12 Comparison of κ_L versus temperature for various investigations in which nanostructured $Bi_{0.5}Sb_{1.5}Te_3$ was reported. The similar values indicate that the mechanism for κ_L reduction is probably the same.

calculated κ_L shown in Figure 2.11(e) also includes the contribution from the bipolar thermal conduction[12,21,34], and may not represent the true lattice thermal conductivity[34]. Poudel *et al*.[19] modelled κ_L based on the Boltzmann equation and showed that it is actually decreasing with temperature, and is reduced by a factor of two in nanocomposites when compared to bulk. In our spark-eroded and bulk samples, the fact that the peaks of the Seebeck coefficient and the minima of the total thermal conductivity occur at similar temperatures (360 – 400 K) suggests that bipolar thermal and electrical conduction becomes important above 360 K[19,21], and the higher Seebeck coefficient in the spark-eroded samples indicates that the bipolar conduction is suppressed, which also contributes to the reduced κ and the enhanced ZT.[21,34]

2.3.2 Spark-Eroded Skutterudite ($CoSb_3$)

The $CoSb_3$ system has been an attractive material for thermoelectric devices because of its large carrier mobility.[3] However, relatively high thermal conductivity has made it inferior to bismuth telluride-based thermoelectrics. The system is thus primarily attractive at medium to high temperatures.[3] Additionally, that high performing thermoelectrics can be made both n- and p-type with the same material system is attractive for fabricating thermoelectric devices (Figure 2.1).

Dyck *et al* has found that embedding divalent Ba into the "cage" of the skutterudite structure creates an additional phonon-scattering site without adversely affecting electrical conductivity.[36] In addition, the group found that the presence of a

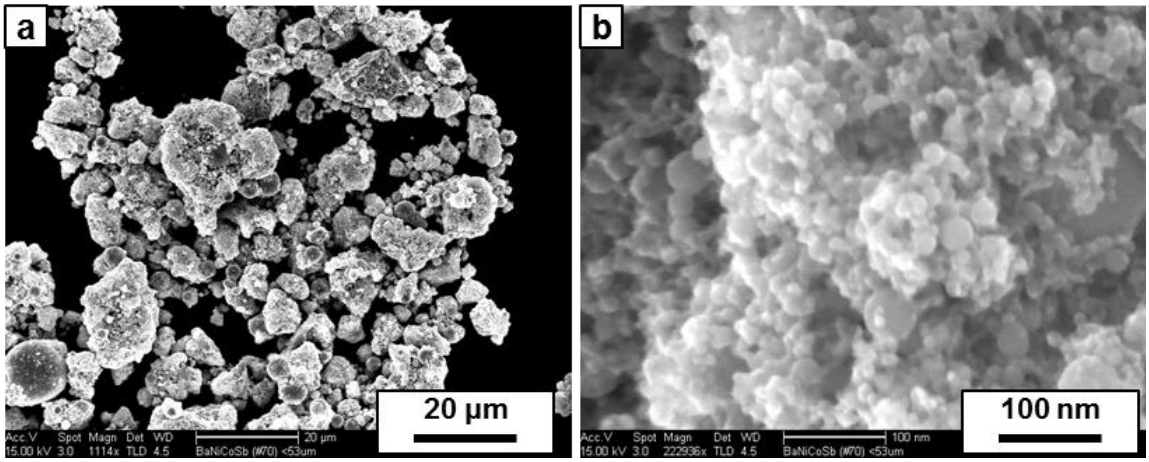

Figure 2.13 SEM images of spark-eroded $Ba_{0.3}Ni_{0.05}Co_{3.95}Sb_{12}$ particles showing (a) the spark-eroded yield and (b) nanoparticle fraction of the yield.

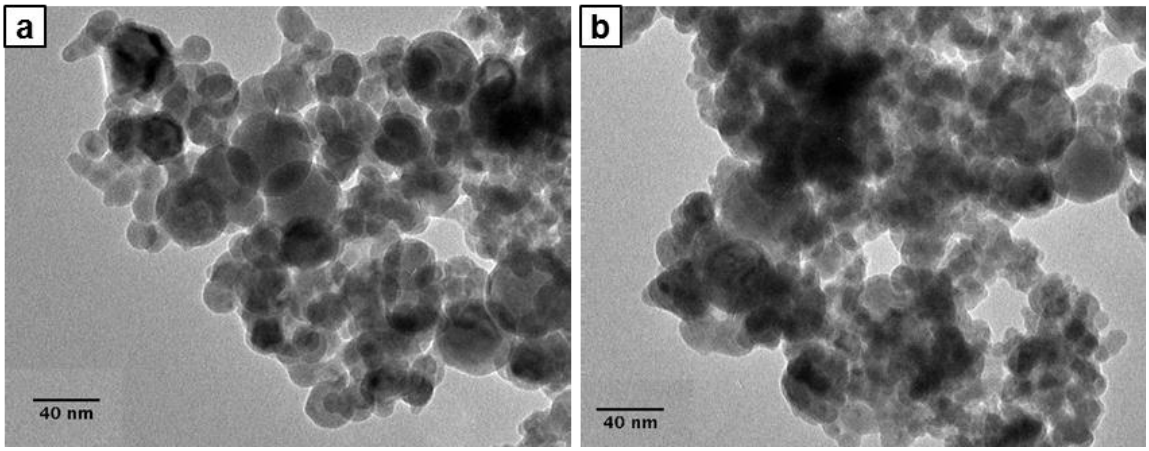

Figure 2.14 TEM images of spark-eroded $Ba_{0.3}Ni_{0.05}Co_{3.95}Sb_{12}$ particles showing 10-40 nm diameter polycrystalline particles.

small amount of Ni in the alloy increases the electron concentration, which enhances the thermoelectric power factor and reduces thermal conductivity due to ionized impurity scattering of phonons. Mi *et al* has reduced the κ_L in $CoSb_3$ by nanostructuring.[37] The work presented in this section uses the Ba- and Ni-containing composition ($Ba_{0.3}Ni_{0.05}Co_{3.95}Sb_{12}$) as spark-eroded targets in order to achieve phonon scattering from both the "caged" Ba and grain boundaries.

The microscopy images in Figures 3.13 and 3.14 confirm the production of fine particles by spark erosion. Like the yield of $Bi_{0.5}Sb_{1.5}Te_3$ discussed in the previous section, the skutterudite yield consists of a major volume fraction of nanoparticles and a minor fraction of micron-sized particles. As expected, the particles are spherical. A particle size distribution (Figure 2.15) shows that the average nanoparticle size is 25 nm.

The XRD patterns of the starting material and spark-eroded powder are shown in Figure 2.16. The starting arc-melted ingots contain the $CoSb_3$ skutterudite, $CoSb_2$ monoclinic, and antimony phases. No barium or nickel phases are detected, either due to complete integration into the skutterudite structure, or existing in too small of a volume to be detected. The latter reason is more likely the case since the starting composition of Ba was determined by the number of atoms required to fill all "cages", and since there are non-skutterudite phases present, Ba is expected to exist somewhere in the alloy. The

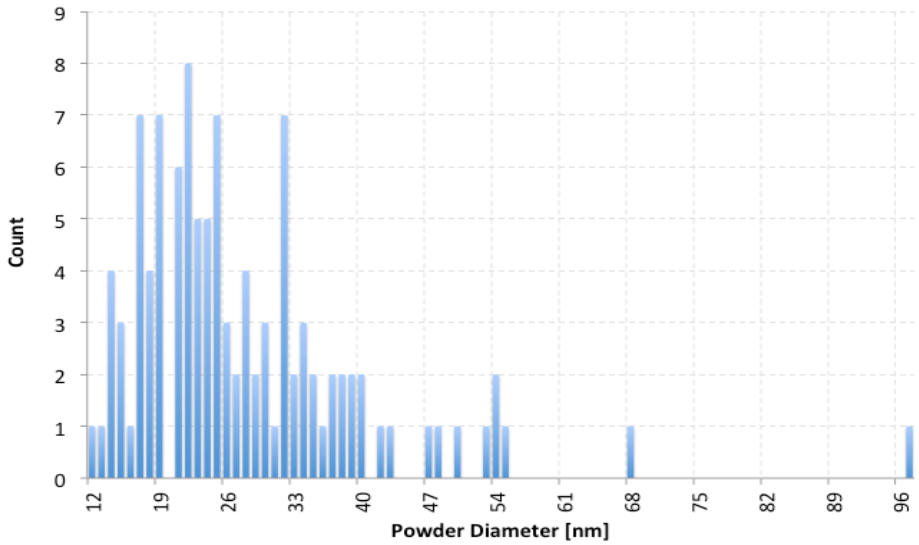

Figure 2.15 Particle size distribution of spark-eroded $Ba_{0.3}Ni_{0.05}Co_{3.95}Sb_{12}$ particles obtained from TEM images showing an average particle size of 25 nm.

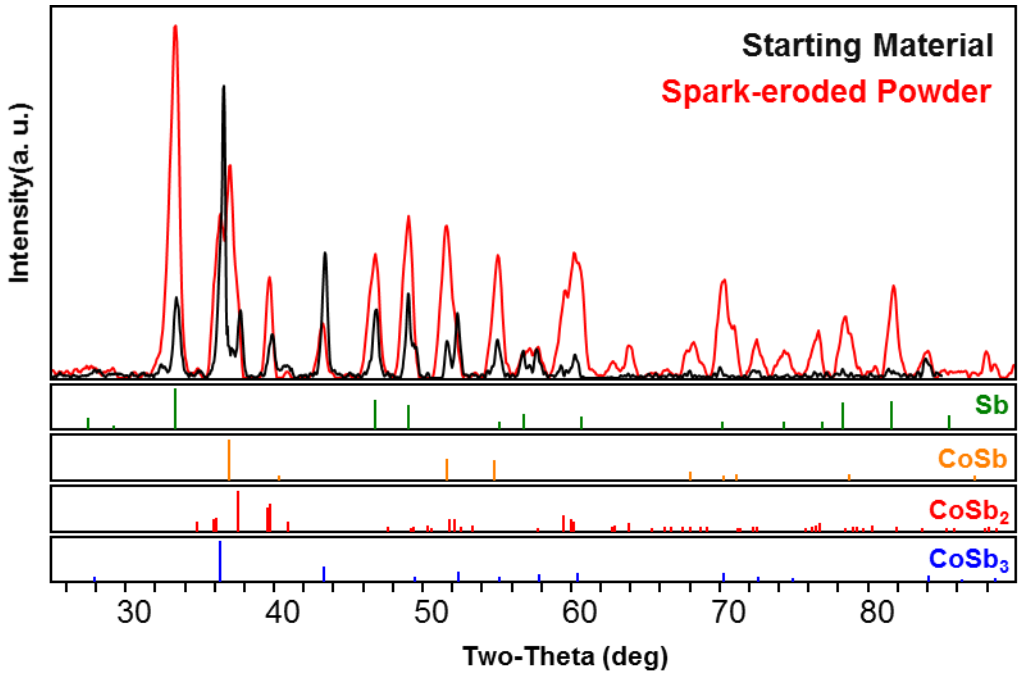

Figure 2.16 XRD pattern of spark-eroded $Ba_{0.3}Ni_{0.05}Co_{3.95}Sb_{12}$ particles and of the starting bulk materials obtained by arc-melting.

spark-eroded powder shows the same phases, except with the addition of the CoSb hexagonal phase. However, after spark erosion, the major peak for Sb has increased. In The peaks are broadened after spark erosion.

The results of an elemental analysis on the starting bulk sample and spark-eroded powder is shown in Table 3.1. The "ideal composition" is obtained for the work by Dyck *et al*, in which the amount of Ba and Ni is optimized.[36] The arc-melted starting material comes very close to this nominal composition. The excess barium at the expense of cobalt is negligible. After spark erosion, the amount of antimony relative to the other elements has decreased. The oxygen content is believed to be due to the measurement process and not due to spark erosion. The lower atomic percent of antimony is surprising

Table 2.1 Atomic percent for skutterudite ($CoSb_3$) starting materials and spark-eroded powder.

Atomic %	Ideal Composition[36]	Starting Material	Spark-Eroded
Barium	1.84	2.53	2.10
Nickel	0.31	0.51	0.50
Cobalt	24.2	23.1	22.7
Antimony	73.6	73.7	65.0
Oxygen	0	0.21	9.7

given the increased peak in the XRD pattern. However, the drop is reasonable since Sb appears to relocate freely during spark erosion; the formation of CoSb and increased Sb is evidence of this.

After compaction by SPS, the thermoelectric properties are measured and shown in Figure 2.17. Considering the multiple phases present in the spark-eroded powder, the thermoelectric properties are surprisingly robust. The highly negative Seebeck coefficient suggests that there is sufficient skutterudite phase, and that it is adequately doped (the negative Seebeck coefficient confirms n-type conduction while $CoSb_3$ is intrinsically p-type[37]). Better SPS parameters increase ZT due to the enhanced thermoelectric power factor. This may be a matter of higher density or phase homogenization. The thermal and electrical conductivities are similar to that of nanostructured $CoSb_3$ reported by Mi *et al*.[37] Dyck *et al* had found that increasing the carrier concentration by adding Ni reduces the Seebeck coefficient while decreasing electrical conductivity at high temperature due to degeneracy. Since this is not observed, it is unlikely that Ni has integrated well in the compacted powders. Moreover, there is no evidence of κ_L reduction by the barium

"caging" effect. Future work should focus on achieving the Ba-filled, Ni-doped skutterudite in bulk form before proceeding to spark-erosion.

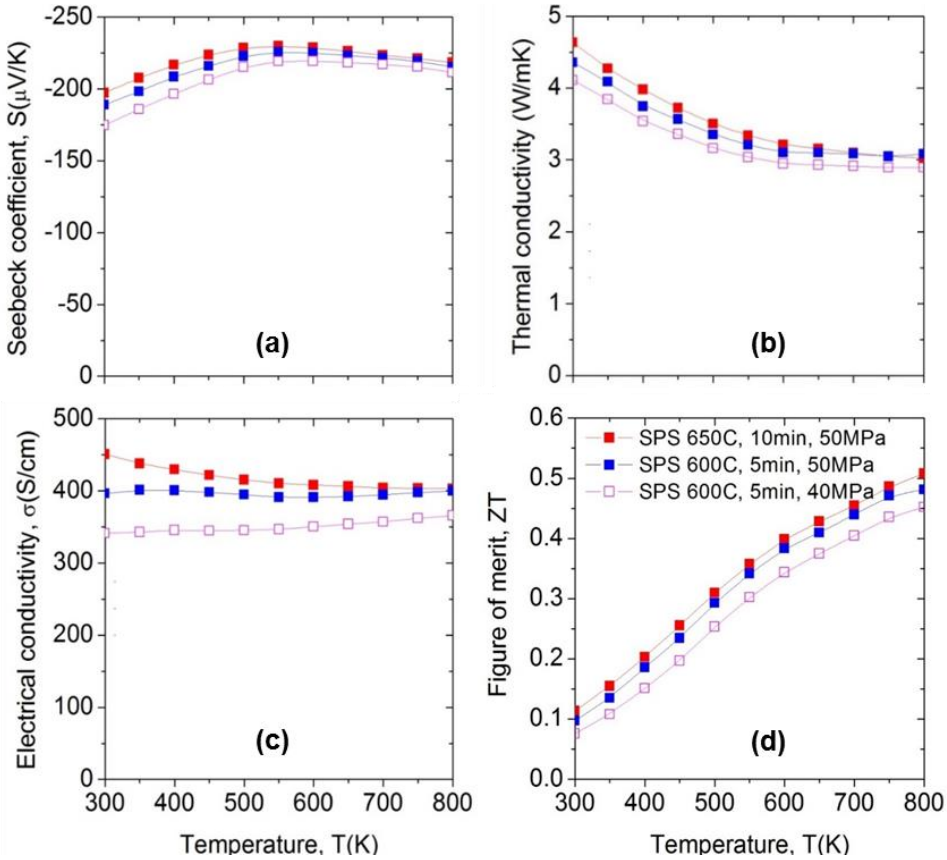

Figure 2.17 Thermoelectric properties of the spark-eroded and SPS-sintered samples under various SPS conditions. (a) Seebeck coefficient, (b) total thermal conductivity, (c) electrical conductivity, (d) ZT value.

2.4 Conclusions

We have developed a uniquely efficient, cost-effective method for producing thermoelectric nanoparticles at a high production rate. These nanoparticles were SPS-sintered into nano-grained thermoelectric alloy with a ZT of the $Bi_{0.5}Sb_{1.5}Te_3$ compact comparable to the best reported values. The improved ZT is a result of the reduced lattice thermal conductivity, as well as the suppressed high temperature bipolar contributions to electronic thermal transport. Spark-eroded $Ba_{0.3}Ni_{0.05}Co_{3.95}Sb_{12}$ powder compacted by SPS also show reduced thermal conductivity, but more doping is required to raise the thermoelectric power factor. Spark erosion not only produces these clean, oxidation-free, high-ZT thermoelectric nanoparticles directly at low energy consumption, but the rate of production is very high, indicating that scale-up to many tons/month is quite feasible. With the inherent nanoparticle synthesis and nanograined structure using spark-eroded thermoelectric alloys, the prospects for further improvements in performance and production rate appear to be promising.

2.5 Acknowledgements

The authors acknowledge a partial support of this research by Iwama fund (S.J.) and Center for Magnetic Recording Research at UC San Diego, and research start-up fund from UC San Diego (R.C.). Very useful discussions with Dr. David Smith at Arizona State University and Dr. Fred Spada at UC San Diego are appreciated.

This chapter, in part, is a reprint of the material as it appears in Nanotechnology, Volume 23, 2012, Phi-Khanh Nguyen, Kyu Hyoung Lee, Jaeyun Moon, Sang Il Kim, Kyunghan Ahn, Li-Han Chen, Sang Mok Lee, Renkun Chen, Sungho Jin, and Ami E. Berkowitz. The dissertation author was the primary investigator and author of this paper.

2.6 References

[1] L. E. Bell, "Cooling, heating, generating power, and recovering waste heat with thermoelectric systems", Science, **321**, 1457-1461 (2008).

[2] D. M. Rowe,"CRC Handbook of Thermoelectrics", CRC Press, Boca Raton, FL (1995).

[3] J.-F. Li, W.-S. Liu, L.-D. Zhao, and M. Zhou, "High-performance nanostructured thermoelectric materials", NPG Asia Mater. **2**(4) 152–158 (2010).

[4] The Mercouri G. Kanatzidis Researcvh group Website. Retrieved February 2015 from "http://chemgroups.northwestern.edu/kanatzidis/greatthermo.html".

[5] M. S. Dresselhaus, G. Chen, M. Y. Tang, R. G. Yang,H. Lee, D. Z. Wang, Z. F. Ren, J. P. Fleurial, P. Gogna, "New directions for low-dimensional thermoelectric materials.", Adv. Mater., **19** (8), 1043-1053, (2007).

[6] C. J. Vineis, A. Shakouri, A. Majumdar, and M. G. Kanatzidis, "Nanostructured Thermoelectrics: Big Efficiency Gains from Small Features", Adv. Mater., **22**, 3970-3980, (2010).

[7] Y. C. Lan, A. J. Minnich, G. Chen, and Z. F. Ren, "Enhancement of Thermoelectric Figure-of-Merit by a Bulk Nanostructuring Approach", Adv. Funct. Mater., **20**, 357-376 (2010).

[8] R. Venkatasubramanian, E. Siivola, T. Colpitts, and B. O'Quinn, "Thin-film thermoelectric devices with high room-temperature figures of merit", Nature, 413, 597-602, (2001).

[9] T. C. Harman, P. J. Taylor, M. P. Walsh, and B. E. LaForge, "Quantum dot superlattice thermoelectric materials and devices", Science, 297, 2229-2232, (2002).

[10] A. I. Boukai, Y. Bunimovich, J. Tahir-Kheli, J. K. Yu, W. A. Goddard, and J. R. Heath, "Silicon nanowires as efficient thermoelectric materials", Nature, 451,168-171 (2008).

[11] A. I. Hochbaum, R. K. Chen, R. D. Delgado, W. J. Liang, E. C. Garnett, M. Najarian, A. Majumdar, and P. D. Yang, "Enhanced thermoelectric performance of rough silicon nanowires", Nature, **451**, 163-167 (2008).

[12] G. J. Snyder and E. S. Toberer, "Complex thermoelectric materials", Nat. Mater., 105-114 (2008).

[13] K. F. Hsu, S. Loo, F. Guo, W. Chen, J. S. Dyck, C. Uher, T. Hogan, E. K. Polychroniadis, and M. G. Kanatzidis, "Cubic $AgPb_mSbTe_{2+m}$: Bulk thermoelectric materials with high figure of merit", Science, 303, 818-821 (2004).

[14] D. T. Morelli, T. M. Tritt, and G. S. Nolas, "Skutterudites: A phonon-glass-electron crystal approach to advanced thermoelectric energy conversion applications", Annu. Rev. Mater. Sci., **29**, 89-116 (1999).

[15] D. G. Ebling, A. Jacquot, H. Bottner, L. Kirste, J. Schmidt, and M. J. Aguirre, "Influence of Group IV-Te Alloying on Nanocomposite Structure and Thermoelectric Properties of Bi_2Te_3 Compounds", Electron. Mater., **38**, 1450-1455 (2009).

[16] J. Q. He, J. R. Sootsman, S. N. Girard, J. C. Zheng, J. G. Wen, Y. M. Zhu, M. G. Kanatzidis, and V. P. Dravid, "On the Origin of Increased Phonon Scattering in Nanostructured PbTe Based Thermoelectric Materials" J. Am. Chem. Soc., 132, 8669-8675 (2010).

[17] G. Joshi, H. Lee, Y. C. Lan, X. W. Wang, G. H. Zhu, D. Z. Wang, R. W. Gould, D. C. Cuff, M. Y. Tang, M. S. Dresselhaus, G. Chen, and Z. F. Ren, "Enhanced Thermoelectric Figure-of-Merit in Nanostructured p-type Silicon Germanium Bulk Alloys", Nano Lett., 8, 4670-4674 (2008).

[18] W. Kim, J. Zide, A. Gossard, D. Klenov, S. Stemmer, A. Shakouri, and A. Majumdar, "Thermal conductivity reduction and thermoelectric figure of merit increase by embedding nanoparticles in crystalline semiconductors", Phys. Rev. Lett., **96**, 045901 (2006).

[19] B. Poudel, Q. Hao, Y. Ma, Y. C. Lan, A. Minnich, B. Yu, X. A. Yan, D. Z. Wang, A. Muto, D. Vashaee, X. Y. Chen, J. M. Liu, M. S. Dresselhaus, G. Chen, and Z. F. Ren, "High-thermoelectric performance of nanostructured bismuth antimony telluride bulk alloys", Science, 320, 634-638 (2008).

[20] T. M. Tritt, N. Gothard, X. Ji, and J. He, "Thermoelectric and transport properties of n-type Bi_2Te_3 nanocomposites", J. Appl. Phys., 103, 054314 (2008).

[21] W. J. Xie, J. He, H. J. Kang, X. F. Tang, S. Zhu, M. Laver, S. Y. Wang, J. R. D. Copley, C. M. Brown, Q. J. Zhang, and T. M. Tritt, "Identifying the Specific Nanostructures Responsible for the High Thermoelectric Performance of $(Bi,Sb)_2Te_3$ Nanocomposites", Nano Lett., 10, 3283-3289 (2010).

[22] W. J. Xie, Y. G. Yan, X. F. Tang, Q. J. Zhang, and T. M. Tritt, "High thermoelectric performance BiSbTe alloy with unique low-dimensional structure", J. Appl. Phys., 105, 113713 (2009).

[23] G. H. Zhu, H. Lee, Y. C. Lan, X. W. Wang, G. Joshi, D. Z. Wang, J. Yang, D. Vashaee, H. Guilbert, A. Pillitteri, M. S. Dresselhaus, G. Chen, and Z. F. Ren, "Increased Phonon Scattering by Nanograins and Point Defects in Nanostructured Silicon with a Low Concentration of Germanium", Phys. Rev. Lett., 102, 196803 (2009).

[24] S. K. Bux, R. G. Blair, P. K. Gogna, H. Lee, G. Chen, M. S. Dresselhaus, R. B. Kaner, and J. P. Fleurial, "Nanostructured Bulk Silicon as an Effective Thermoelectric Material", Adv. Funct. Mater., 19, 2445-2452 (2009).

[25] M. R. Dirmyer, J. Martin, G. S. Nolas, A. Sen, and J. V. Badding, "Thermal and Electrical Conductivity of Size-Tuned Bismuth Telluride Nanoparticles", Small, 5, 933-937 (2009)

[26] M. Scheele, N. Oeschler, K. Meier, A. Kornowski, C. Klinke, and H. Weller, "Synthesis and Thermoelectric Characterization of Bi_2Te_3 Nanoparticles" Adv. Funct. Mater., 19, 3476-3483 (2009).

[27] M. Scheele, N. Oeschler, I. Veremchuk, K. G. Reinsberg, A. M. Kreuziger, A. Kornowski, J. Broekaert, C. Klinke, and H. Weller, "ZT Enhancement in Solution-Grown $Sb_{(2-x)}Bi_xTe_3$ Nanoplatelets", ACS Nano, 4, 4283-4291 (2010).

[28] Y. C. Zhang, H. Wang, S. Kraemer, Y. F. Shi, F. Zhang, M. Snedaker, K. L. Ding, M. Moskovits, G. J. Snyder, and G. D. Stuck, "Surfactant-Free Synthesis of Bi_2Te_3-Te Micro-Nano Heterostructure with Enhanced Thermoelectric Figure of Merit", ACS Nano, **5**, 3158-3165 (2011).

[29] K. C. See, J. P. Feser, C. E. Chen, A. Majumdar, J. Urban, and R. A. Segalman, "Water-Processable Polymer-Nanocrystal Hybrids for Thermoelectrics", Nano Lett., **10**, 4664-4667 (2010).

[30] R. Y. Wang, J. P. Feser, X. Gu, K. M. Yu, R. A. Segalman, A. Majumdar, D. J. Milliron, and J. Urban "Universal and Solution-Processable Precursor to Bismuth Chalcogenide Thermoelectrics", J. Chem. Mater., 22, 1943-1945 (2010).

[31] Y. Ma, Q. Hao, B. Poudel, Y. C. Lan, B. Yu, D. Z. Wang, Z. F. Ren, and G. Chen, "Enhanced thermoelectric figure of merit in nanostructured n-type silicon germanium bulk alloy", Nano Lett., 8, 2580-2584 (2008).

[32] X. W. Wang, H. Lee, Y. C. Lan, G. H. Zhu, G. Joshi, D. Z. Wang, J. Yang, A. J. Muto, M. Y. Tang, J. Klatsky, S. Song, M. S. Dresselhaus, Z. F. Ren, and G. Chen, "Enhanced thermoelectric figure of merit in nanostructured n-type silicon germanium bulk alloy", Appl. Phys. Lett., 93, 193121 (2008).

[33] G. Chen, X. A. Yan, B. Poudel, Y. Ma, W. S. Liu, G. Joshi, H. Wang, Y. C. Lan, D. Z. Wang, and Z. F. Ren, "Experimental Studies on Anisotropic Thermoelectric

Properties and Structures of n-Type $Bi_2Te_{2.7}Se_{0.3}$", Nano Lett., 10, 3373-3378 (2010).

[34] J. S. Dyck, W. Chen, and C. Uher, "Thermoelectric properties of the n-type filled skutterudite $Ba_{0.3}Co_4Sb_{12}$ doped with Ni", J. Appl. Phys., Vol. 91, No. 6, 15 (2002).

[35] J. L. Mi, T. J. Zhu, X. B. Zhao, and J. Ma, "Nanostructuring and thermoelectric properties of bulk skutterudite compound $CoSb_3$", J. Appl. Phys., **101**, 054314 (2007).

CHAPTER 3: PERMANENT MAGNETS

3.1 Background

3.1.1 Principles

Permanent magnets (PM) are materials that retain their magnetization in the absence of a magnetic field and are useful due to the strong external fields that they produce. The strength of this field is a result of the remnant magnetization, M_r, and the stability of this magnetization (the resistance to demagnetization) requires high coercivity, H_C. These properties can be achieved by the engineering of ferromagnetic materials.

Ferromagnetic materials are spontaneously magnetized due to "exchange forces".[1] The magnitude of magnetization, the magnetic moment per volume, is determined mainly by composition since electrons' spins and orbits determine the magnetism in materials. *Magnetocrystalline anisotropy* refers to the preference for the magnetization to lie along certain crystallographic directions, called "easy" directions. In hexagonal crystals, the c-axis is the only easy-axis (uniaxial crystal anisotropy), while cubic crystals (not discussed in this dissertation) have several easy-axes due to increased symmetry. When placed in a field, the magnetization rotates to align with the field direction. The magnetocrystalline anisotropy, typically described by the anisotropy constant, K, is a measure of the energy required to rotate the magnetization 90 degrees away from the easy-axis.

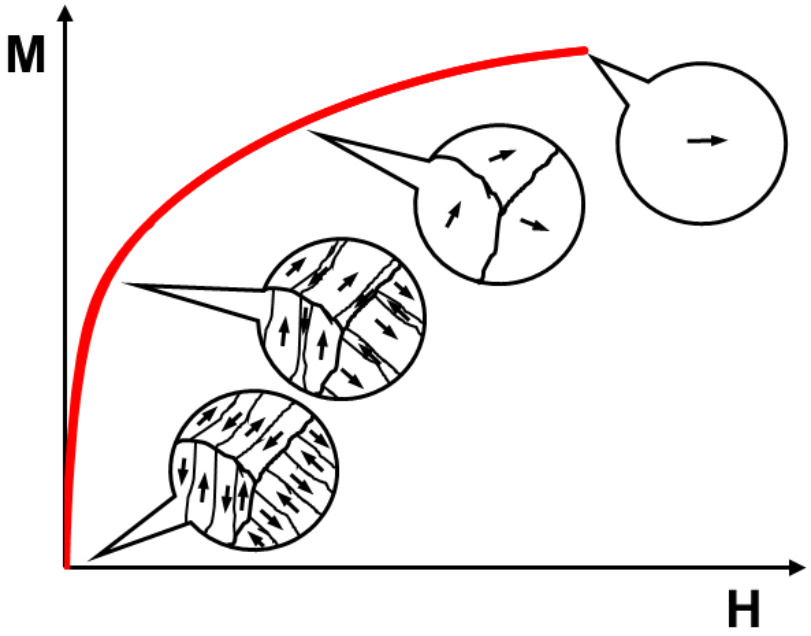

Figure 3.1 The magnetization process of a multi-domain, polycrystalline sample showing that magnetization first occurs by domain wall motion, then by rotation of the magnetized domains until saturation magnetization. Upon demagnetization, domain walls are typically nucleated.

Magnets achieve a lower energy state by creating magnetic domains in which regions of magnetization point in various directions, minimizing the net M_r (Figure 3.1). The regions that separate the domains are called the domain walls. When a field is applied, the moments of the domains align with the field direction by moving domain walls such that domains with moments pointed along the field direction grow at the expense of opposing domains. In polycrystalline magnets, the moments are then pointed towards the randomly-oriented easy-axes that must then rotate towards the field direction. When all domains are aligned, saturation magnetization, M_S, is achieved. Upon field reversal, reverse domains will nucleate and grow. Hysteresis of the magnetization as the

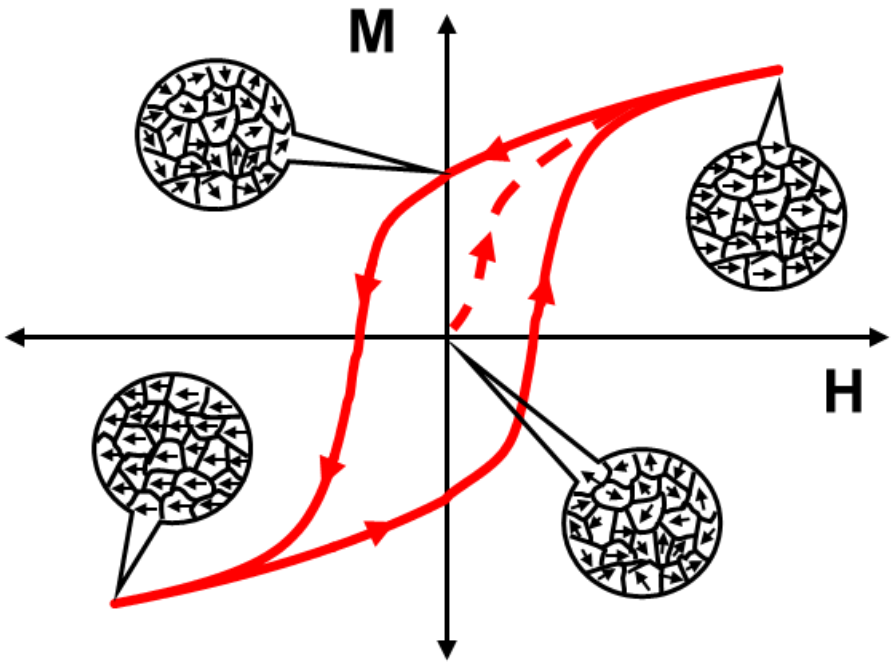

Figure 3.2 The magnetization process of randomly-oriented single-domain particles with uniaxial crystal anisotropy.

applied field is cycled generally depends on the magnitude of the magnetic anisotropy energy and the presence of "pinning" sites for the domain walls.

When particle dimensions are small enough, single-domain particles are produced. The hysteresis of these particles depends on their magnetic anisotropy energy and their shape. A group of non-interacting single-domain particles can be aligned along their easy axes and compacted so that domain rotation is the only mechanism for magnetization reversal in the bulk compact. The magnetization cycle is shown in Figure 3.2. Here, the moments point in random directions in the demagnetized state. When a field is applied, moments first flip along the easy-axis towards the field direction and then rotate to align with this direction. When the field is then reduced to zero, the moments

rotate back to the easy-direction, but remain pointed towards the direction in which they were magnetized (remnant state). In this ideal case, a measurement of this magnet parallel to the aligned axis would produce M_r equal to M_S and H_c equal to the anisotropy field, H_K (K/M_S). If randomly-oriented, $M_r = 0.5M_S$, and $H_C \approx 0.5H_K$.

3.1.2 The Maximum Energy Product – $(BH)_{MAX}$

A permanent magnet operates at a point somewhere along the second quadrant of the B-H curve subject to the demagnetization field, H_{dm}, which is determined by the shape of the magnet; its direction is opposite that of the magnetization. The *magnetostatic energy* within a magnet can thus be defined as:

$$E = -\frac{1}{2}\int B \cdot H dV, \tag{3.1}$$

where B is the total magnetic flux in the sample and $H = H_{applied} - H_{dm}$. The *energy product* is defined as $-B \cdot H$ (energy per volume). Finally, the figure of merit of a permanent magnet is the **maximum energy product**, $(BH)_{MAX}$, which is the largest product of the B and H fields in the second quadrant of the B-H loop, shown as the shaded region in Figure 3.3.

In Figure 3.3, a "square" M-H loop is plotted over the B-H loop, where $B = H + 4\pi M_S$. The "squareness" of the M-H loop affects the slope of the B-H curve in the second

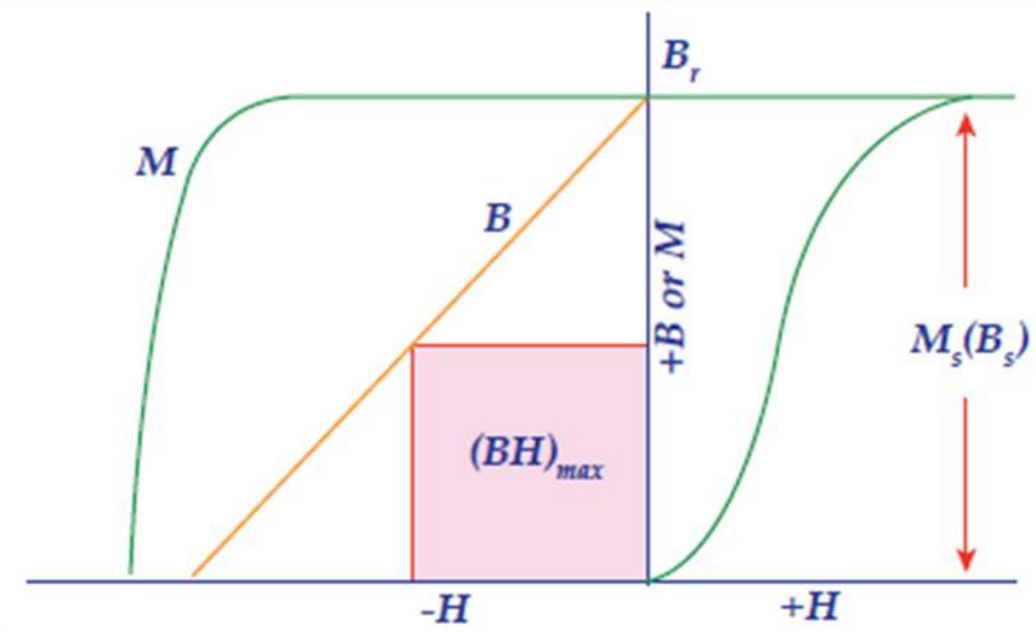

Figure 3.3 M-H and corresponding B-H loops for a typical permanent magnet with a graphical representation of the maximum energy product, $(BH)_{MAX.}$[2] (© IEEE)

quadrant. When M is flat ($M_r = M_S$) as shown in Figure 3.3, the area that represents $(BH)_{MAX}$ is the largest. If the M-H loop is not square (e.g. for randomly-oriented particles), then some domains begin to switch at fields smaller than H_C, decreasing the *extrinsic coercivity* of the B-H loop and therefore also $(BH)_{MAX.}$ (Note: in this dissertation, H_C, or simply the coercivity, refers to the M-H loop. H_C of the B-H loop will be referred to as the extrinsic coercivity). Magnetic alignment is thus crucial to achieving high $(BH)_{MAX}$. Since M_r cannot exceed M_S, the magnitude of B in the second quadrant is limited by M_S since $Br = M_r$.

The coercivity of the M-H loop, dictates the "knee" of the B-H loop, shown in Figure 3.4. By increasing H_C, the extrinsic coercivity can be extended into the third quadrant, which is the case for the lower temperature loops in Figure 3.4. When a "knee" is present, the shape of the magnet is limited; the magnet must be elongated in the

alignment direction in order to decrease the demagnetizing field so that the operating point is sufficiently away from the "knee" reducing the risk of demagnetization. As the extrinsic coercivity nears half of B_r, the $(BH)_{MAX}$ then begins to reduce.

Currently, Nd-Fe-B magnets achieve the highest $(BH)_{MAX}$ (Figure 3.5) and are thus used for wind turbine generators and electric vehicle motors. However, for these applications require the magnet to operate at around 180°C.[3] The anisotropy of magnets, and thus H_C, typically decrease when temperature is increased (Figure 3.6). Therefore, at this elevated temperature, Nd-Fe-B magnets are inadequate and require doping with dysprosium in order to increase H_C at 180°C (Figure 3.4). For this reason, dysprosium is labeled by the U.S. Department of Energy as the most critical element to a clean energy future (Section 1.2).

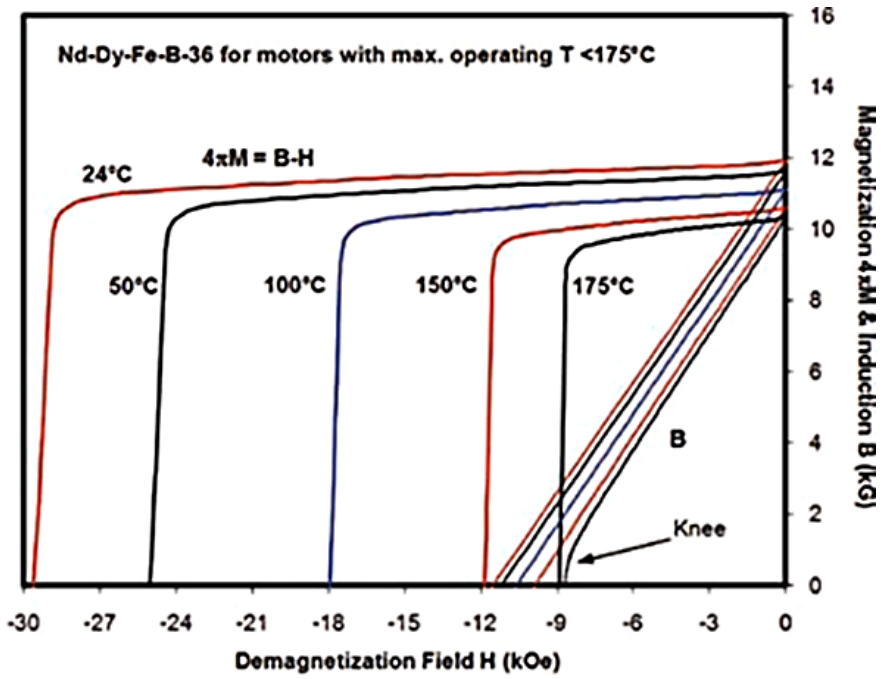

Figure 3.4 Magnetization and induction curves for a Nd-Dy-Fe-B magnet at various temperatures. The "knee" moves towards the higher fields (more negative) when coercivity is increased.[3] (© WILEY)

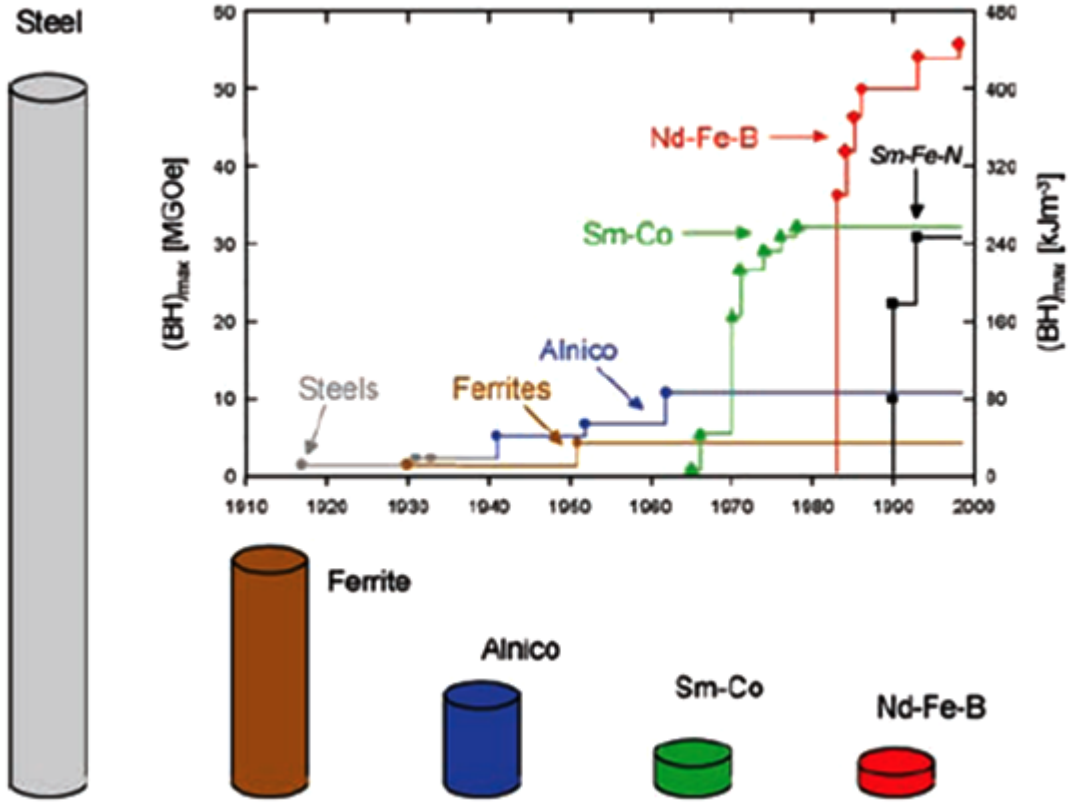

Figure 3.5 Development of permanent magnets in the 20th century, and a visual comparison of permanent magnets with similar energy densities at room temperature (each magnet has 100mT field 5mm from the top surface)[3] (© WILEY)

Figure 3.6 shows the dependence of $(BH)_{MAX}$ and H_C on temperature for various permanent magnet materials. As it turns out, at higher temperature, Sm-Co magnets can outperform Nd-Dy-Fe-B magnets, and it is used for selected applications. Currently, no other materials are competitive with these rare-earth magnets. The rare-earth-free ferromagnetic materials that have high M_S have low crystal anisotropy, and the highly anisotropic materials have relatively low M_S. A proposed method for creating high M_S, high K magnets by a two-phase approach will be discussed. The ideal permanent magnet

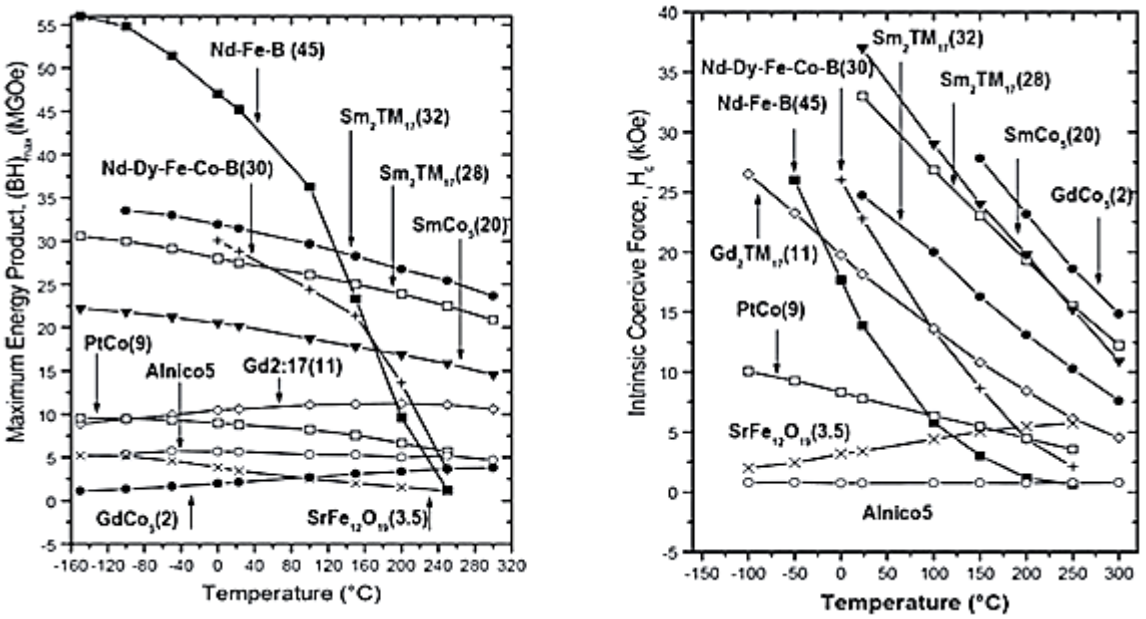

Figure 3.6 Maximum energy product and intrinsic coercivity versus temperature for various permanent magnets showing a general decrease with increasing temperature.[4] (© IEEE)

would be rare-earth-free, have high M_S, high H_C at elevated temperatures, and easy to produce. This work in this dissertation aims for all of the above.

3.1.3 Exchange-Spring Magnets

In 1991, Kneller and Hawig proposed a two-phase magnet in which the magnetization of a hard magnet could be increased by the addition of a high-M_S soft magnet with little reduction in H_C.[6] The proposed magnet would behave like a single-phase magnet with a higher energy product. The schematic in Figure 3.7 depicts such a magnet with exchange-coupled hard and soft layers. In this figure, the applied field

opposite to the magnetization of the hard phase, but lower in magnitude than the switching field of the hard phase. The moments closer to the hard layer are more strongly coupled, and thus the soft magnetization resembles a torsional spring upon demagnetization.

The exchange-spring concept requires that the soft phase be sufficiently small such that domain walls do not form upon reversal. The soft phase should be about twice the width of the hard phase domain walls (i.e., ≈ 2-4 nm). The smaller the hard phase, the larger the volume fraction of soft-phase, and thus larger M_S and $(BH)_{MAX}$.

The implications of the exchange-spring magnet are that a hard, rare-earth-free magnet could be coupled with a soft, high-M_S magnet in order to form rare-earth-free

Figure 3.7 Model of an exchange-spring magnet showing the hard/soft interfaces and the "spring" that forms with the soft magnetization.

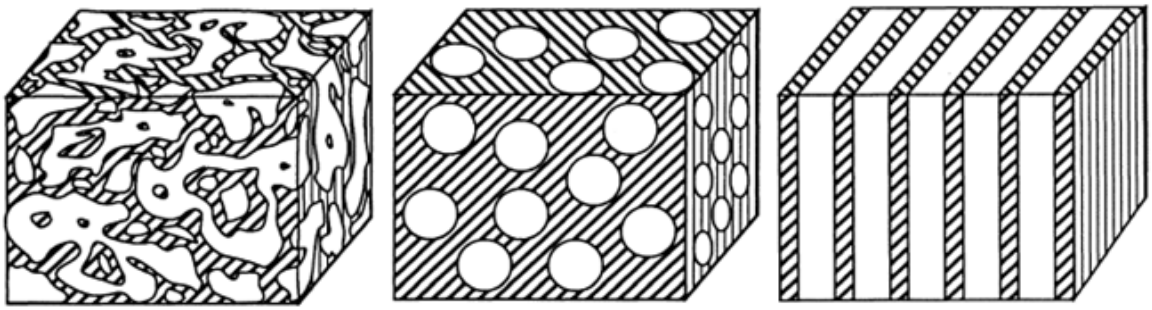

Figure 3.8 Possible configurations for bulk exchange-spring magnets showing a disordered magnet in which both phases are smaller than the Bloch wall thickness, soft inclusions within a hard matrix, and alternating soft/hard layers. The striped phase is the oriented hard phase.[7] (© The American Physical Society)

permanent magnets that would have competitive $(BH)_{MAX}$ compared to Nd-Dy-Fe-B magnets. However, a bulk exchange-spring magnet has never been produced. Figure 3.8 shares some possible configurations for bulk exchange-spring magnets. This chapter focuses on promising routes for the development of rare-earth-free exchange-spring permanent magnets using the spark erosion technique.

3.1.4 Low-Temperature Phase MnBi

The most promising candidate for a rare-earth-free permanent magnet is the low-temperature phase of manganese bismuth (LTP-MnBi). The intermetallic alloy exists in three phases, a low-temperature phase (LTP), high-temperature phase (HTP), and quenched-high-temperature phase (QHTP), with LTP-MnBi being the most attractive. LTP-MnBi has a high uniaxial magnetocrystalline anisotropy at room temperature ($K \approx 10^7$ ergs/cc) that increases with temperature.[8] This leads to an unusual increase of

coercivity with increasing temperature. With a large coercive force, the theoretical maximum energy product of LTP-MnBi is believed to be 18 MGOe.[9] At 180ºC, the

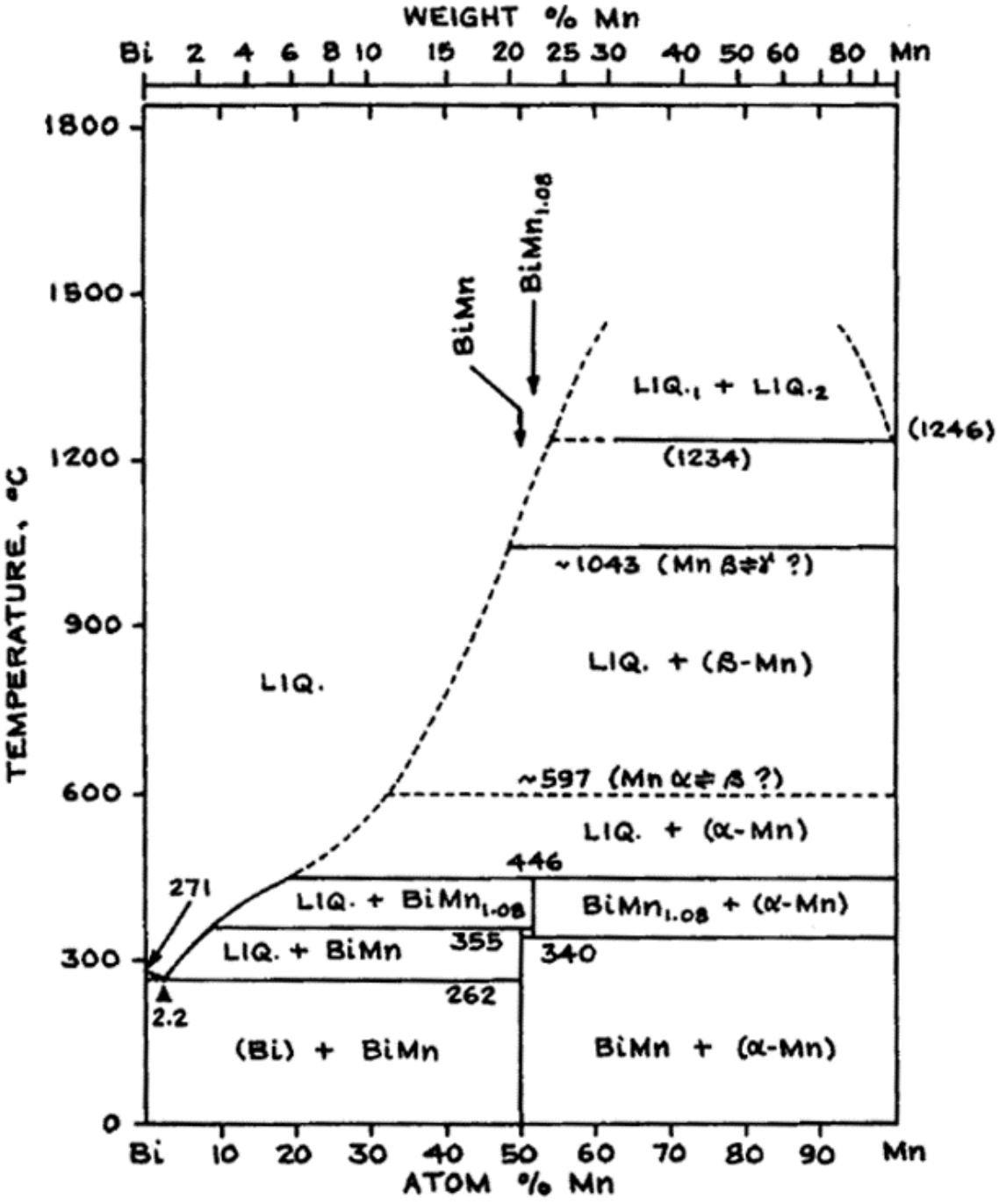

Figure 3.9 The Mn-Bi phase diagram.[10] (© General Electric Company)

coercivity of LTP-MnBi surpasses that of conventional permanent magnet materials such as Nd-Fe-B and Sm-Co.

However, a single-phase LTP-MnBi bulk sample is difficult to obtain as a consequence of its peritectic phase diagram[9, 10] (Figure 3.9). Above the peritectic temperature, Mn segregates from the Mn-Bi melt. The transition from the closely-related HTP, existing as $Mn_{1.08}Bi$, to LTP-MnBi yields an excess of Mn. Obtaining LTP-MnBi by diffusion is tedious since the annealing must be carried out below 340°C; the diffusion of Mn and Bi through the MnBi phase has been shown to be extremely slow.[11]

Among the known methods of producing pure LTP-MnBi , Chen *et al* grew single-crystal MnBi by pulling a seed crystal from the melt.[8] Later, Yoshida *et al* obtained bulk MnBi by quenching in liquid nitrogen, arc-melting, and then zone-melting.[12] More recently, Guo *et al* used melt-spinning to form amorphous MnBi flakes that crystallized upon annealing.[13] In order to form particles, the melt spun ribbon were ball-milled.[14] Others have studied LTP-MnBi powders produced by mechanically grinding the bulk ingot; the saturation magnetization, M_S, of these samples were not high.[15, 16]

In this chapter, we discuss several superior methods for producing LTP-MnBi bulk alloys and particles. First, we describe how polycrystalline LTP-MnBi of > 90 wt % was made by chill-casting and subsequent annealing at 300°C for 96 hours. This sample has a room temperature moment of 73.5 emu/g in 70 kOe, as compared to the saturation magnetization (M_S) of 80 emu/g.[17] We also report a novel method for preparing high-M_S bulk MnBi by extraction of the non-magnetic Bi phase from an arc-melted MnBi ingot. When these bulk LTP-MnBi ingots are spark-eroded, the as-prepared powder consists of

amorphous, crystalline, and superparamagnetic particles, mostly as porous aggregates. When subsequently annealed and lightly milled, the randomly-oriented powder has M_S of 69 emu/g and H_C of 1 T at room temperature. The $(BH)_{MAX}$ for this randomly-oriented powder is 3.0 MGOe at room temperature. The large fraction of amorphous particles, when crystallized in a magnetic field, can be oriented along the field direction. By this method, a hysteresis with M_r/M_S of 0.8 is achieved. Finally, when the spark-eroded powders are mixed with soft phases by various methods in order to determine potential routes to an exchange-spring magnet, it was found that FeCo is the best candidate for coupling.

3.2 Experimental Procedures

3.2.1 Preparation of High M_S Bulk Ingots

High purity LTP-MnBi ingots were fabricated by induction melting and chill-casting an alloy with purity > 99.9%, a weight ratio of 77.9/22.1 Bi/Mn ($Mn_{1.08}Bi$), and subsequently annealing at 300°C for 96 hrs.

An alternative method was to arc-melt > 99.9% purity $Mn_{1.1}Bi$ billets (52.4 at % Mn). The billets had thicknesses of 0.25, 0.375, and 0.5 inches. They were placed on a rigid stainless wire mesh (9 × 9) inside of a stainless steel chamber constructed of commercial vacuum flange components, sealed with a copper gasket. They were positioned in two ways: randomly placed on top of a flat mesh, and supported at the sides by a mesh fixture (Figure 3.10). The entire chamber was placed in the uniform heat region of a Lindberg (Blue M) Box furnace for annealing. The ingots were annealed at

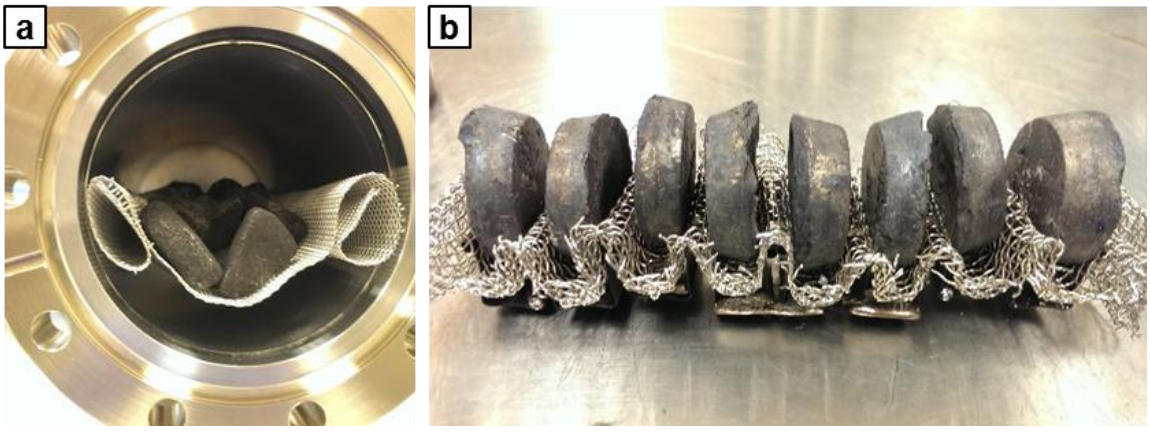

Figure 3.10 The setup for vacuum-annealing showing (a) ingots placed randomly atop a stainless steel mesh inside a 3 inch diameter high-vacuum chamber, and (b) ingots mounted on a stainless steel fixture creating separation.

330°C for 64 hours in ≈ 10^{-5} torr. As a control experiment, one ingot was annealed under similar conditions in a small furnace placed inside an argon glove box (< 5 ppm O_2).

3.2.2 Powder Sample Preparation

The ingots were spark-eroded with liquid nitrogen as the dielectric. The powder yield was coarsely sieved at 270 mesh in order to remove bulk material chipped off the charge pieces during this low temperature process. The powders were annealed in a small quartz tube furnace in the glove box. Samples were heated from room temperature to 300°C in ≈ 15 minutes when the furnace power was turned off (no hold time).

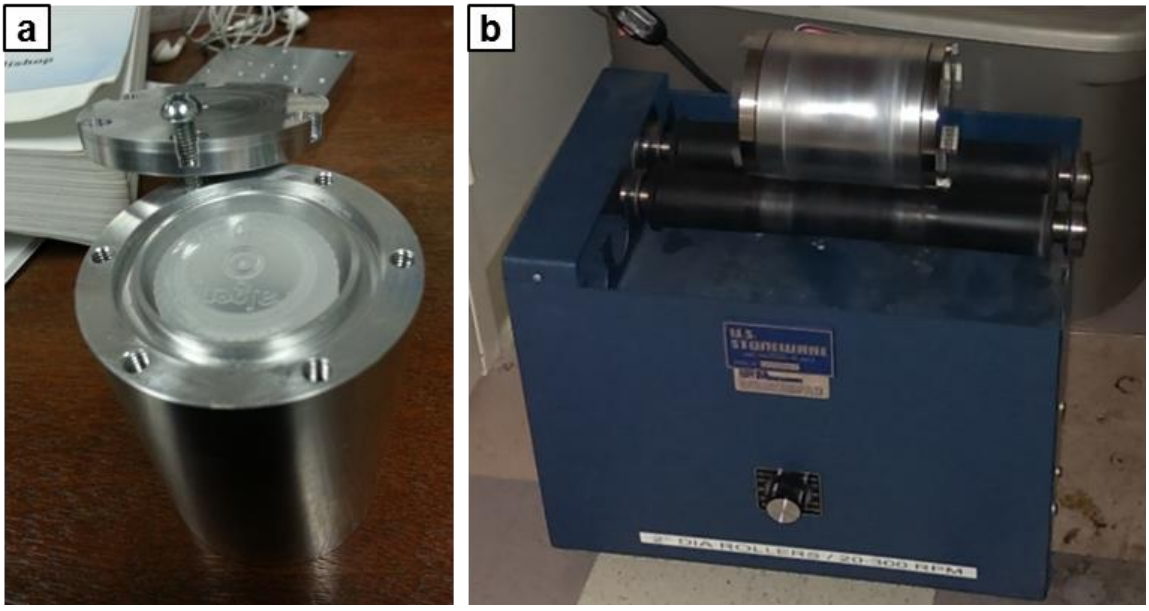

Figure 3.11 Milling setup showing (a) a plastic bottle inserted into a custom aluminum container for SPEX milling and (b) a welded stainless steel container on a commercial roller.

A few grams of the annealed powders was loaded into a plastic container (about 20 cc volume) together with 20-30 2 mm diameter ceramic or plastic beads. This plastic container was inserted into a custom aluminum vessel that is sealed by an O-ring (Figure 3.11a). The container was loaded into a commercial SPEX Mill and milled for 3 hrs.

For ball-milling, a custom welded stainless steel container (4 inch id) was used on a commercial roller (Figure 3.11b). 10 grams of powder was weighed and loaded into the container with hexane and a random mixture of 0.25, 0.375, and 0.5 inch diameter chrome steel balls that were filled to about half the volume of the container. The milling went for 19 hours at a rotation speed of 43 RPM. As-sparked and annealed powder, and

Figure 3.12 High-frequency ultrasonic probe located inside of a nitrogen glove box (an argon glove box appeared to cause shorting of the piezoelectric circuit due to arcing).

powder mixtures, were milled. For Fe, Co, and FeCo mixtures, the powder consisted of 25, 27, and 26 percent soft phase by weight, respectively. The powders were also mixed using an ultrasonic probe (Figure 3.12). Powders were ultrasonicated for several hours in hexane.

Bulk and spark-eroded MnBi were coated with Co by mixing in $CoCl_2$ ethanol solutions of various molarities. A bulk ingot was placed in a beaker with $CoCl_2$ in ethanol (0.25 M) and stirred overnight. For powder samples, the mixing was done by ball-milling, ultrasonication, and drip-stirring. For these samples, the $CoCl_2$ quantity was calculated to give a 2 nm coating on the spark-eroded particles. The powder samples were Co-coated by ball-milling with glass beads in glass bottles. The same glass bottles were sonicated in an ultrasonic bath. The powder was also mixed with ethanol and continuously stirred as 10 mL of $CoCl_2$ solution was slowly dripped into the bottles at rate of 1mL/min.

3.2.3 Rapid Process Sintering (RPS)

A custom “rapid process sintering” (RPS) technique was developed for compaction of the spark-eroded particles and mixtures. Figure 3.13 shows the schematic of this process. RPS uses an insulating die constructed of Macor™. The pistons were stainless steel. The die was placed in a small aluminum vacuum chamber that fits in a 12 ton Mini C Carver press. The aluminum chamber also acts as an electrode and was insulated from ground. An AC transformer provides a low voltage, high current power

source. As determined by the resistance of the sample, up to 400 A can be utilized, which heated the sample to 300°C at a rate of up to 100°C/min.

Powder samples were loaded into the RPS chamber within the glove box. The chamber was closed with a vacuum valve, moved into the Carver, and evacuated with a diffusion pump. Samples were pressed to 100 MPa and heated to various temperatures at various heating rates. A resulting compact is shown in Figure 3.14.

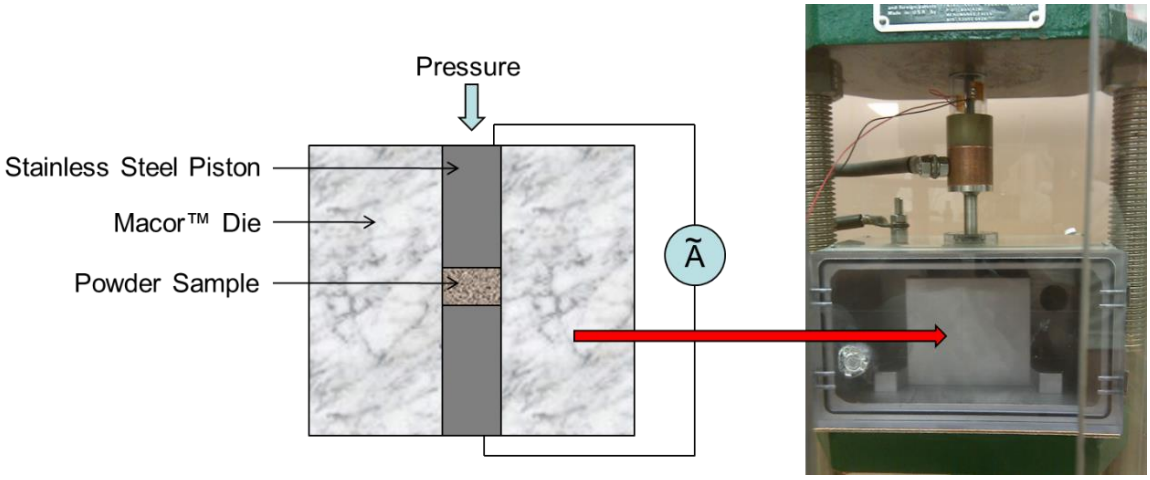

Figure 3.13 Schematic of Rapid Process Sintering (RPS) showing a powder sample within the insulating Macor™ die, pressed with stainless steel pistons through which an AC current is applied. The die is placed in an aluminum vacuum chamber, which is then placed on a Carver press for the application of pressure. The feedthrough for the top piston is sealed with an O-ring and is electrically insulating in order to prevent electrical contact with the aluminum chamber, which acts also as a current pathway.

Figure 3.14 Bulk MnBi that has been compacted by RPS from spark-eroded MnBi powder compared to a U.S. dime. The nominal diameter of the compact is 3/8 inches.

3.2.4 Magnetic Measurements & Characterization

The magnetic properties of the powders and bulk ingots were measured by vibrating sample magnetometry (VSM) using a Physical Property Measurement System (PPMS, Quantum Design, Inc). Zero-field-cooled and field-cooled (ZFC/FC) curves were measured from 75 K to 300 K with an applied field of 50 Oe and a heating rate of 10 K/min. Higher-temperature measurements (> 300 K) and temperature-dependent coercivities were measured in a commercial VersaLab™ VSM Oven (Quantum Design, Inc). In order to assure that particles do not oxidize during measurement, they were encased in silver foil. The method for preparing VSM samples in this manner is shown in the flow diagram in Figure 3.15. The weight of the silver foil was tared from the weight of the sealed sample to determine the powder weight.

The oxygen content of spark-eroded powders and their sample capsules were measured by inert gas fusion (ASTM E 1019-11). Empty capsules were measured for

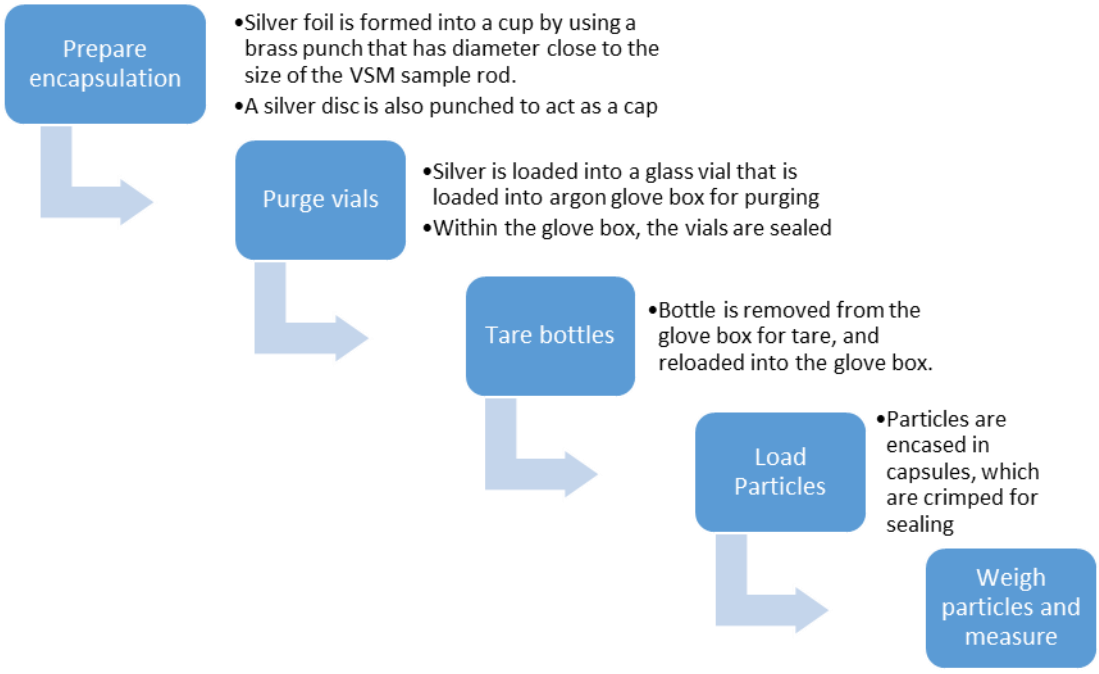

Figure 3.15 Flow chart for preparing samples for VSM measurements. The samples are encapsulated in silver foil in order to prevent the particles from oxidizing.

their contribution to the total oxygen content. The other elemental compositions were measured by direct current plasma emission spectroscopy (ASTM E 1097-07) and verified by x-ray fluorescent spectroscopy (XRF) and energy-dispersive x-ray spectroscopy (EDX).

Electron microscopy images of the samples were taken with a Phillips XL30. Optical microscopy was performed with a Keyence digital microscope with image-stitching software. In order to observe the cross-section of tight clusters, the as-sparked powder was cold pressed at 300 MPa and then mounted in epoxy for polishing. Bulk samples were mounted in epoxy and polished with a Buehler MiniMet™ polisher. To observe the domain structure of the magnetic phase, a suspension of $CoFe_2O_4$ nanoparticles in hexane was applied to polished bulk ingot. The particles collect in

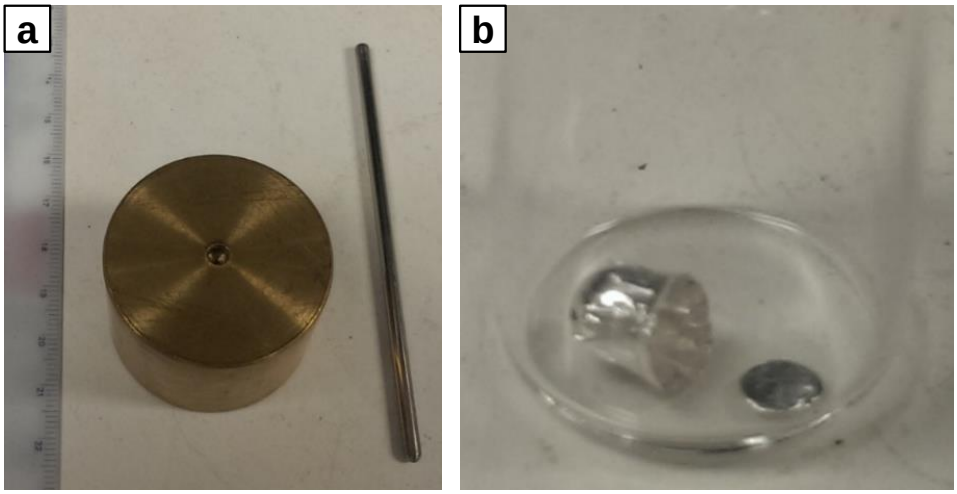

Figure 3.16 (a) Brass punch and rod used for preparing VSM sample cups. (b) Silver cup/cap inside of a glass vial.

regions of non-uniform fields, such as domain walls, displaying what are known as Bitter patterns.

X-ray diffraction (XRD) patterns were measured with a Bruker D7 powder diffractometer with a LynxEye™ detector in the Bragg-Brentano geometry. In order to minimize powder oxidation during measurement, powders were loaded into a sealed glass bottle in an argon glove box. For measurements, petroleum jelly was quickly introduced to the bottle and mixed with the powder. The jelly was smeared onto an amorphous silicon sample holder for measurement. For even better protection, the alternative method of sealing powders with packaging tape was also used (Figure 3.17). This method reduces oxidation but also contains several backgrounds peaks and generates an overall peak shift due to refraction.

The densities of the ingots were measured by the Archimedes method.

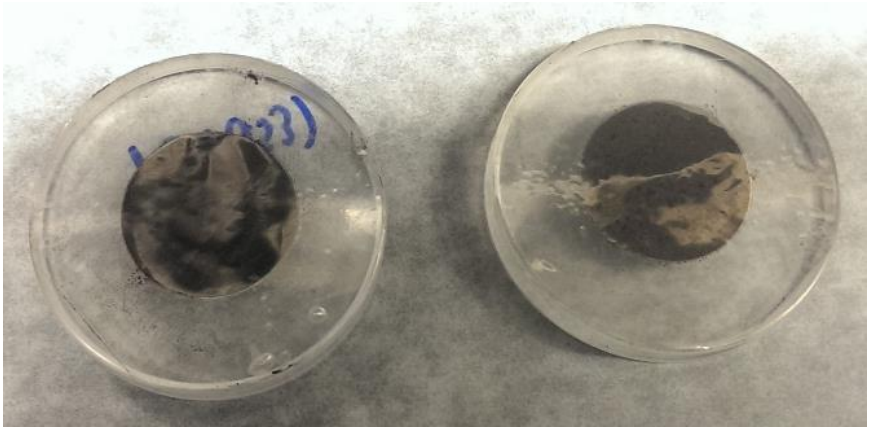

Figure 3.17 Powder x-ray diffraction (XRD) samples. To best prevent oxidation during measurement, powder samples are sealed in argon using packaging tape. The tape adds a background peak and causes an overall peak shift due to refraction.

3.2.5 Magnetic Alignment

About 0.5 grams of spark-eroded MnBi was mechanically cold pressed in the argon glove box by using the screw-press tool shown in Figure 3.18. In this figure, the cross-section of the tool is shown, and the resulting 0.25 inch diameter green body is compared to a U.S. dime. The pressure was determined to be around 600 MPa.

The pressed sample was encased in copper foil and mounted on a "VSM Oven" component provided by Quantum Design, Inc for heating in a superconducting magnet. The heater rod with the mounted sample was placed in a VersaLab™ in which annealing at 300°C for 5 min in 3 T field and high vacuum was carried out. The moment of the sample was measured prior to, during, and after the heating process. This, along with the field and temperature was recorded and shown in Figure 3.20.

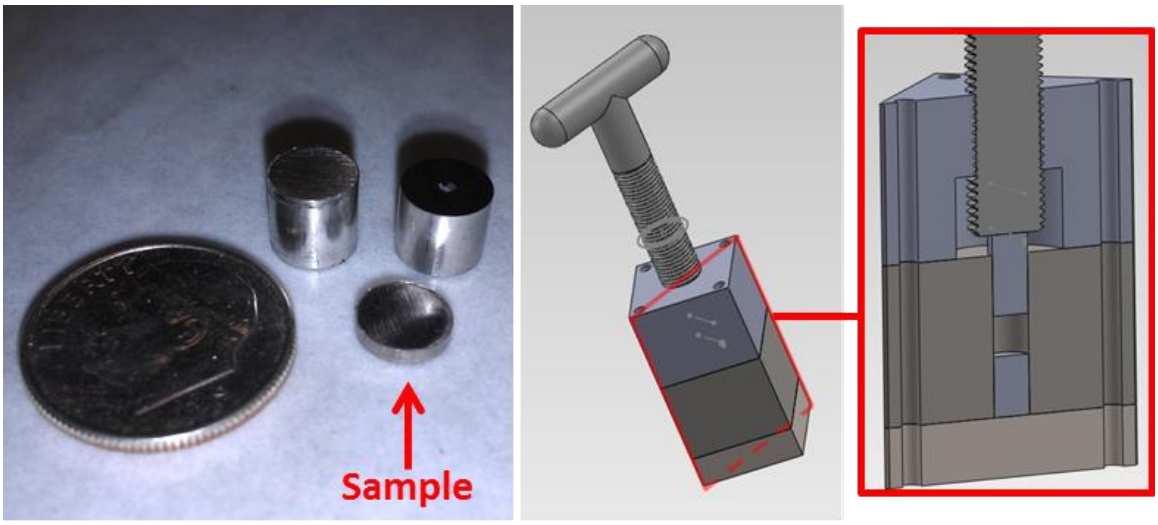

Figure 3.18 A cold-pressed pellet made from spark-eroded powder compared to pressing pistons and a U.S. dime. The pellet was made using a custom screw-press tool that applies an approximated 600 MPa to the powder sample while inside an inert glove box. The cross section of this fixture is also displayed.

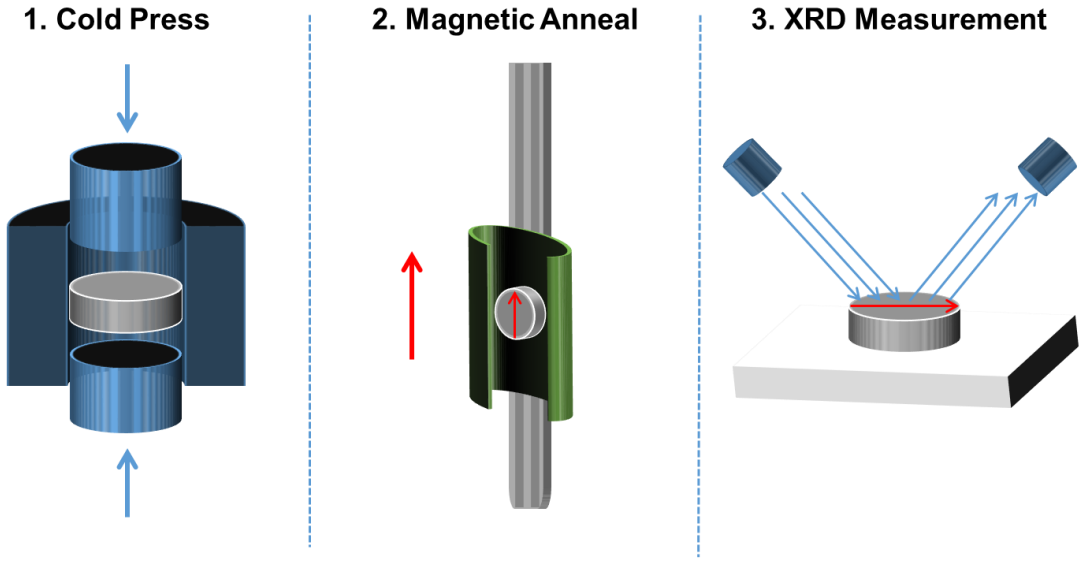

Figure 3.19 The process for orienting spark-eroded MnBi green compacts by directional crystallization of the amorphous component in a magnetic field. The sample is first cold pressed, and then it is mounted onto a heater rod that is inserted into a superconducting magnet. The direction of the applied field is shown by a red arrow. The orientation of the compact during XRD measurement is also shown by a red arrow.

In order to characterize the crystallographic orientation of the magnetically annealed sample, the direction of the applied field is noted when removing the pellet for XRD measurement. The pellet was placed flat on the XRD sample holder as shown in Figure 3.19.

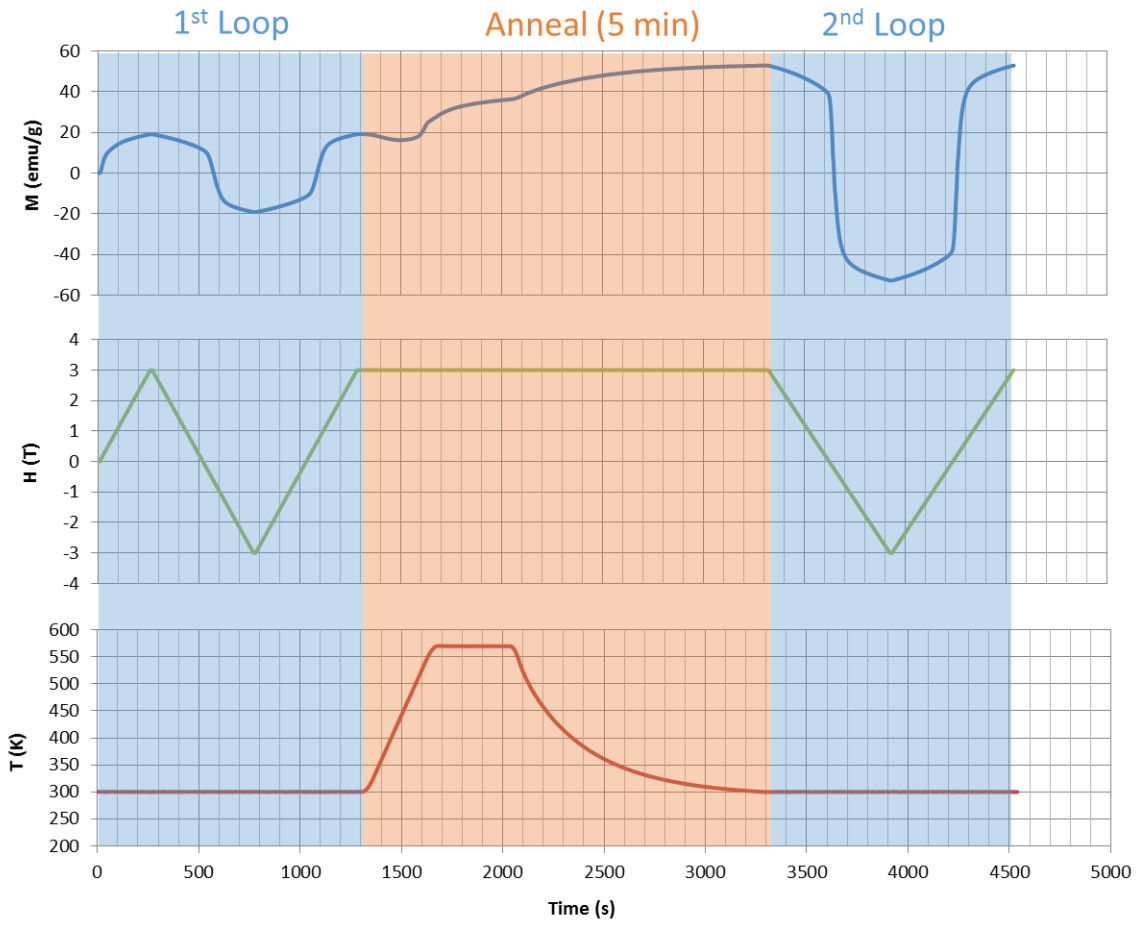

Figure 3.20 Measurement and annealing profile showing magnetization, applied field, and temperature versus time. A large increase in moment during annealing can be seen. The 1st and 2nd loops represent the room-temperature M-H loops of the sample before and after annealing. In the interim, the temperature is increased to 573 K, held for 5 minutes, and then cooled to 300 K, all while the field is held at 3 T.

3.3 Results and Discussion

3.3.1 Bulk MnBi Ingots

Figure 3.21 shows that the higher the magnetization of the starting charge, the higher that of the resulting powder. It is due to the difficulties in achieving pure LTP-MnBi that the bulk ingots were formed by two methods.

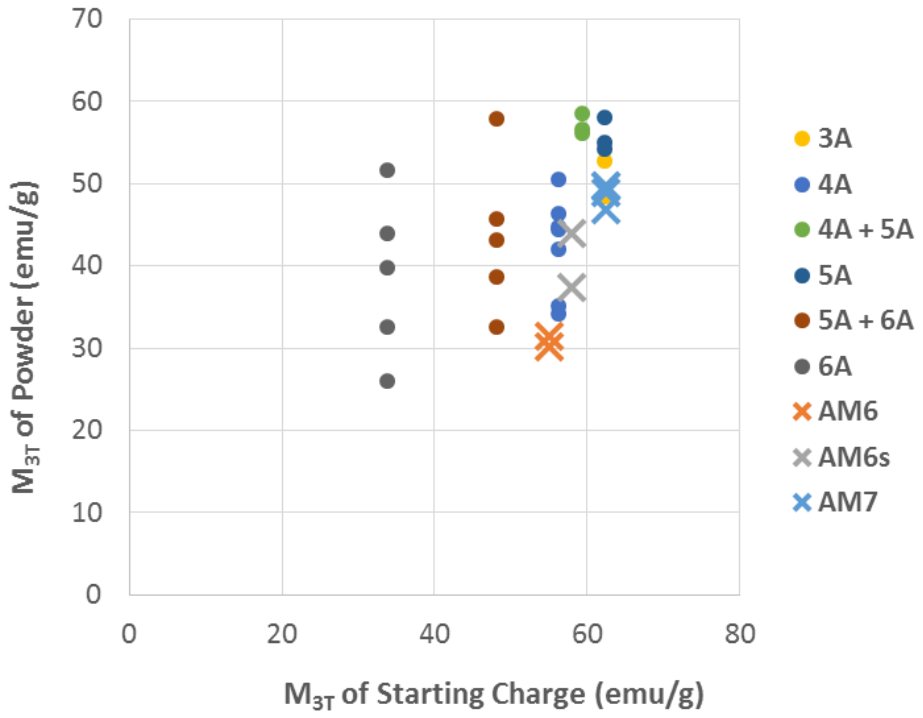

Figure 3.21 MnBi spark erosion runs plotted by the magnetization of the charge versus that of the resulting spark-eroded powder for several chill-cast and arc-melted ingots (no label denotes chill-cast, "AM" denotes arc-melted)

3.3.1.1 Bulk MnBi by Chill-Casting

The M-H loop measured at 300 K shown in Figure 3.22 shows a moment of 73.5 emu/g in 70 kOe for an annealed chill-cast ingot. This value is the best among several iterations of chill-casting and is the highest reported value for bulk MnBi ingots in the literature. The high slope at low applied fields suggests a nucleation mechanism for magnetic domain reversal, which would explain the low H_C in a fine-grained sample. The high field (70 kOe) required for saturation confirms the high magnetocrystalline anisotropy of LTP-MnBi.

The microscopic cross-sections of the chill-cast ingots before and after annealing are shown in Figure 3.23. The images display three phases. There are black precipitate-like facets dispersed over a dominant "darker" region shared with a "lighter" region.

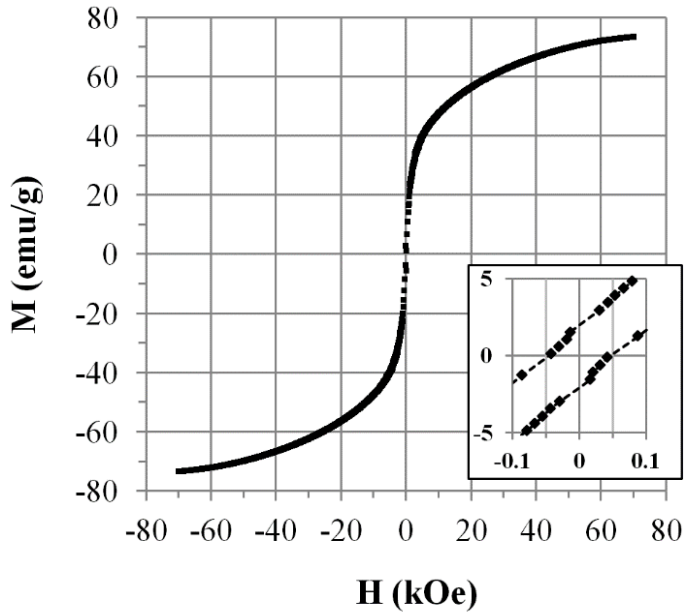

Figure 3.22 M-H loop of the bulk polycrystalline sample showing M_S of 73.5 emu/g at 300 K. The inset shows the low field (100 Oe) region showing $H_C \approx 50$ Oe.

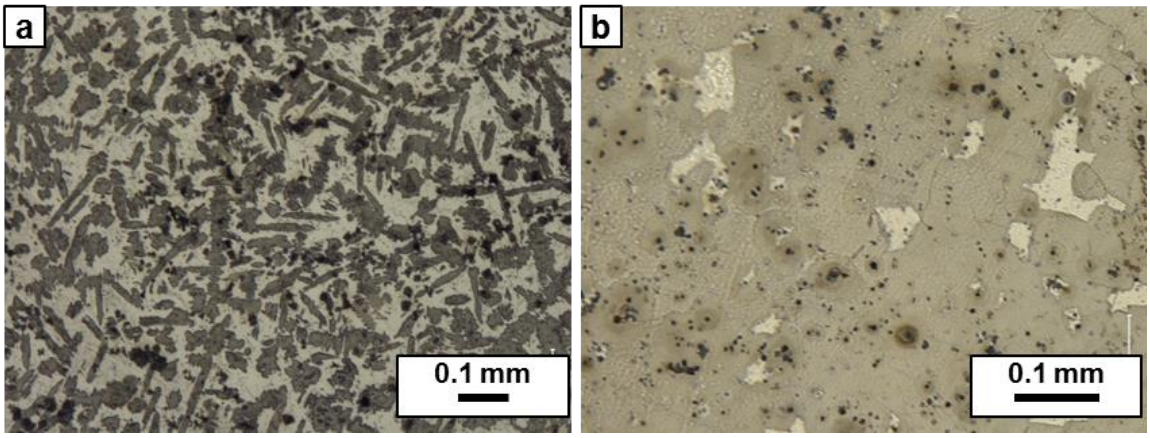

Figure 3.23 Cross-sectional optical microscopy images of a chill-cast ingot (a) before and (b) after annealing showing black precipitates over a dark and light phase. The fraction of dark phase (LTP-MnBi) increases after annealing.

Based on the moment of the magnetization curve, it is reasonable to believe that this "darker" region is the LTP-MnBi phase.

When a 50/50 at % Mn-Bi melt begins to cool from the liquidus to the peritectic temperature, it undergoes phase segregation of Mn, leaving a liquid that is rich in Bi. Once this peritectic temperature is reached, the MnBi alloy begins to solidify leaving a melt still rich in Bi. Upon further cooling to the eutectic temperature the entire melt solidifies into MnBi and a significant portion of Bi. It is reasonable to infer that the precipitate-like black facets are the Mn that segregates during cooling, and the "lighter" region resembles the Bi formed upon solidification.

The elemental mapping by EDX in Figure 3.24 shows Mn to be present in the black facets and "darker" region; Bi is present in the "darker" region, but more strongly detected in the "lighter" region; and oxygen is found in the black facets. This suggests that the black facets are indeed Mn (oxidized), the "lighter" region is Bi, and the "darker" region is the magnetic MnBi phase.

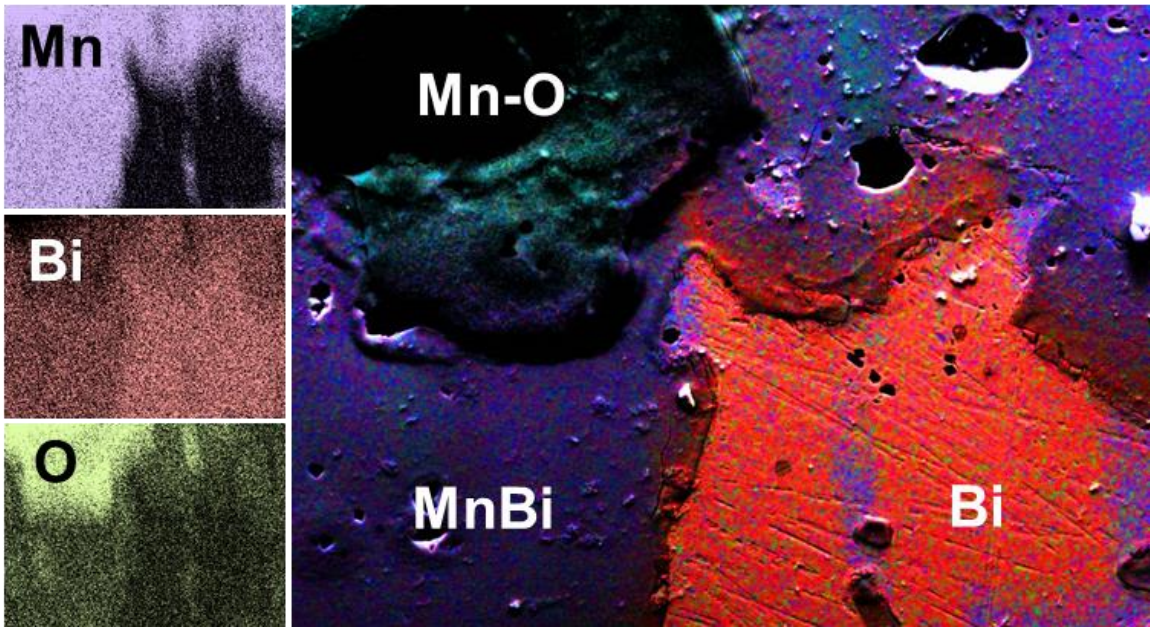

Figure 3.24 Elemental mapping of the annealed chill-cast ingot by EDX, which aids in identifying the Mn, Bi, and MnBi phases. For the individual element maps, white denotes the existence of the element.

The XRD pattern of the polished surface of the ingot sample is shown in Figure 3.25. In view of the high moment, we expected a diffraction pattern dominated by LPT-MnBi peaks. However, the diffraction pattern shows only the Bi phase. The puzzle was investigated by examining a powder prepared by lightly hand grinding some of the sample in an agate mortar and pestle in an argon atmosphere. For the ground sample, the LTP-MnBi peaks appear with much higher peak intensities than the Bi peaks. The most likely explanation for this is that the LTP-MnBi grains in the sample are very large relative to the irradiated area, effectively behaving like single crystals, with minimized regions properly oriented for signals in the Bragg-Brentano geometry.

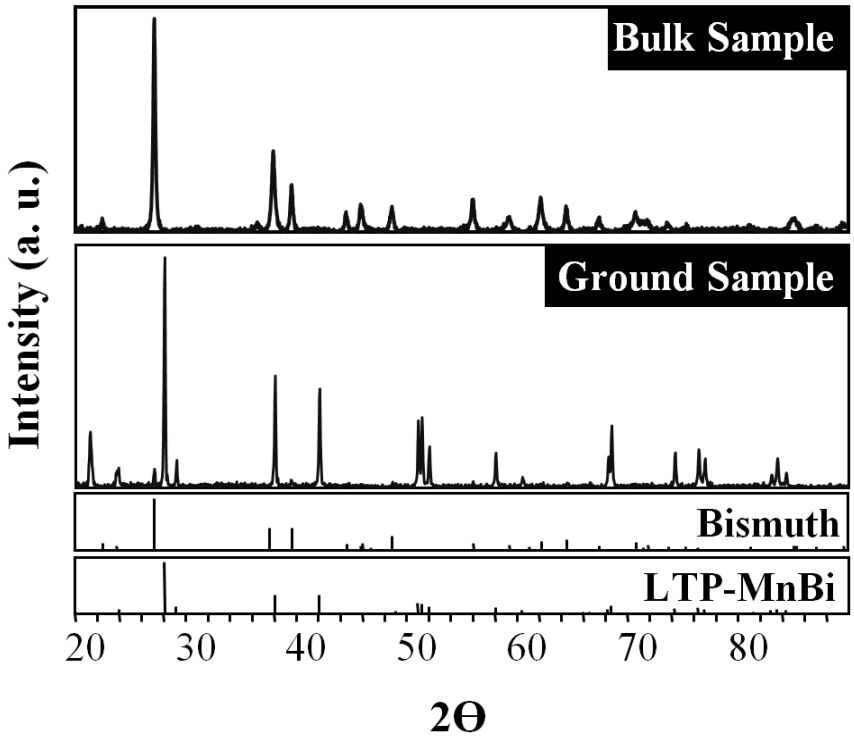

Figure 3.25 X-ray diffraction pattern of the bulk chill-cast ingot in bulk and powder form (from mortar and pestle grinding). Large grains in the bulk sample do not provide a random enough crystal orientation distribution, and thus MnBi peaks cannot be detected.

The domain wall structure for MnBi is evident in the Bitter pattern in Figure 4.26.[18] The hexagonal c-axis, the easy axis, runs parallel to the striations seen in Figure 3.26. Therefore, a distribution of crystal orientations can be observed ranging from these striations, axes oriented in the plane of observation, to the dots that represent easy-axes pointing out of the plane of observation. The image also shows that the crystallite sizes are on the order of 100 μm, which supports the discussion of the XRD patterns in Figure 3.25. The individual crystallites in Figure 3.26(b) exhibit sharp edges and corners which can be sites for nucleation of reverse domains. This is consistent with the high slope seen in the M-H loop.

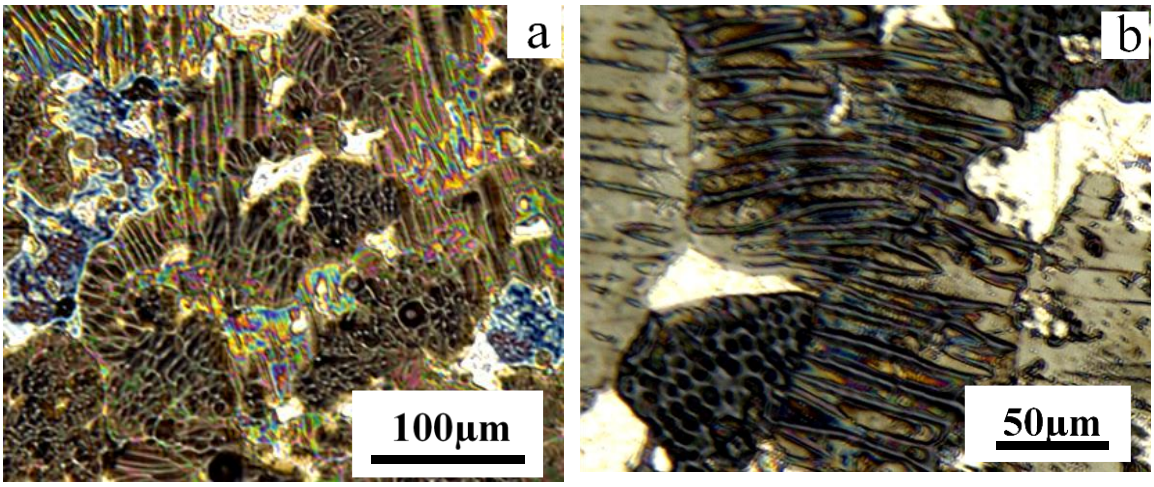

Figure 3.26 Optical microscopy image of the LTP-MnBi chill-cast ingot after application of "Bitter Juice". The resulting Bitter pattern shows a randomly-oriented, multi-domain, polycrystalline sample.

It was expected that grinding the bulk sample into particles in the single domain size range[19], would increase the coercivity. The M-H loop of a milled sample in Figure 3.27 shows an increase of coercivity to 4.5 kOe at 300 K. The moment has decreased to 65 emu/g, possibly due to oxidation. The SEM image included in Figure 3.27 verifies the presence of particles well below the single domain size. In addition, larger particles are present; these are likely multidomain. Furthermore, the bifurcation field of the M-H loop is about 20 kOe, on the order of the anisotropy field.

In Figure 3.28, the entire as-cast ingot is sectioned off into the largest samples that can be cross-sectioned, polished, and observed by microscopy. The results micrographs are re-stitched together, and by careful analysis, it was determined that the entirety of the ingot is homogeneous.

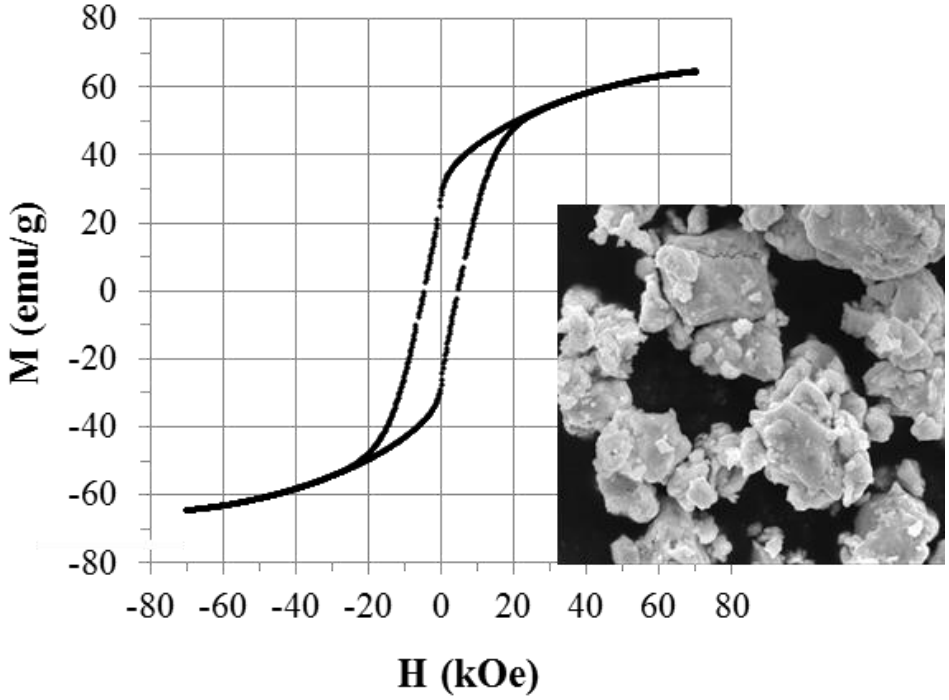

Figure 3.27 M-H loop at 300 K for particles formed by attrition milling of the chill-cast ingot and the SEM image of this sample.

A large disadvantage in chill-cast ingots, however, is the inconsistency in their formation due to the large number of variables associated with the casting process. For this reason, the chill-cast ingot presented in this section was the best among several castings. Some variables that may affect the structure are the melt temperature (the measurement of this is nontrivial), rate of pouring, location of pouring, mixture, etc. Since the ingot has been found to be homogeneous, it is believed that the main cause for poor properties occurs when the ingot begins to cool prior to being poured, although this has yet to be fully studied.

Figure 3.28 The complete polished cross-section of the chill-cast ingot. The ingot was determined to be homogeneous despite an expected temperature gradient from directional quenching.

3.3.1.2 Increased Magnetization by Vacuum Annealing

Due to inconsistencies with chill-casting, another technique was developed in order to obtain high M_S in bulk ingots. Arc-melted MnBi ingots do not achieve high M_S. Improvement involves the extraction of bismuth from arc-melted ingots by annealing in vacuum. During this process, it is essential to use a mesh screen in order to allow molten bismuth to depart from the ingot. The resulting Bi that gathers can be seen in Figure 3.29(c).

After all annealing processes on arc-melted ingots, the shape of the ingot remains nominally unchanged. When the ingots are placed directly atop the mesh (Figure. 4.10a), bismuth also accumulates along the edge of the ingot (Figure. 4.29b). This bismuth mass is presumed to have formed from the molten state since bismuth melts at 271ºC, which is below the annealing temperature. The bismuth is not seen when a MnBi ingot is annealed

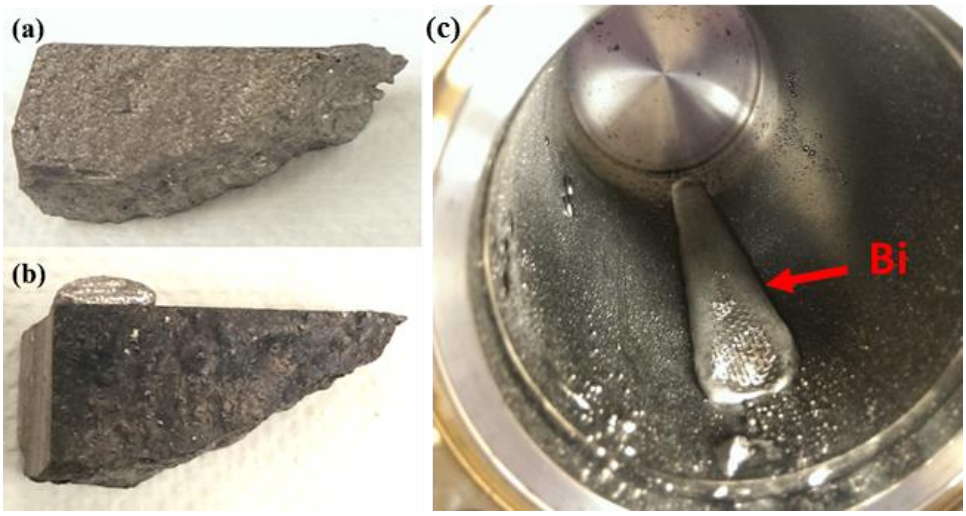

Figure 3.29 Photograph of the arc-melted ingot a) before and b) after vacuum-annealing. After vacuum-annealing, a large mass of Bi is found at the bottom of the annealing chamber.

in argon. Therefore, it is believed that the vacuum, which creates a pressure differential between the interior and exterior of the ingot, effectively extracts molten Bi from the MnBi ingot. Gravity forces the bismuth downwards towards the mesh. Most of the bismuth flows through the mesh, accumulating at the bottom of the chamber.

Figure 3.30 shows M_S of ingots of various thicknesses, annealing time, and relative measurement location on the bulk ingot. Increasing the ingot thickness to 0.375 inch from 0.25 inch does not appear to change the average M_S. However, further increasing the thickness to 0.5 inch decreases M_S. Increasing ingot thickness appears to increase the difference of M_S between samples taken from the center versus the edge of the ingot. In addition, increasing the anneal time also widens this gap. This suggests bismuth migration out of the ingot. As expected, the poorest properties occur at the edge of the sample, in the largest ingot, annealed for the longer duration.

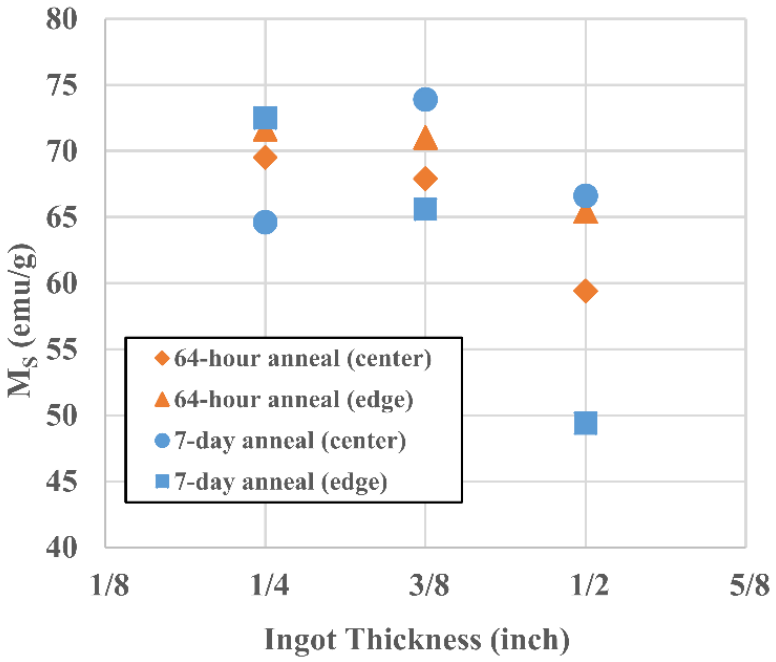

Figure 3.30 Magnetic properties versus size, annealing time, and sampling position. Saturation Magnetization of $Mn_{1.1}Bi$ bulk ingots of varying thicknesses, annealing duration, and measurement location.

While the metallic phases of an as-cast ingot are relatively homogeneous (not depicted), the vacuum-annealed ingot shows a bismuth-rich region at the bottom of the micrograph, which is enlarged in the Figure 3.31 inset. This region of higher bismuth density corresponds to the bottom of the ingot contacted with the stainless steel mesh where bismuth appears to accumulate. The mesh, or contact with another ingot, blocks the bismuth from extraction. This bottom surface can be removed mechanically by grinding or sandblasting, but it is much simpler to remove the source of blockage. In the fixed, oriented ingots, the amount of blockage is reduced, and hence Bi can freely flow out (Figure 3.32). The contact points on the side of the ingot do not accumulate bismuth, which is consistent with the observation that bismuth is pulled downwards by gravity.

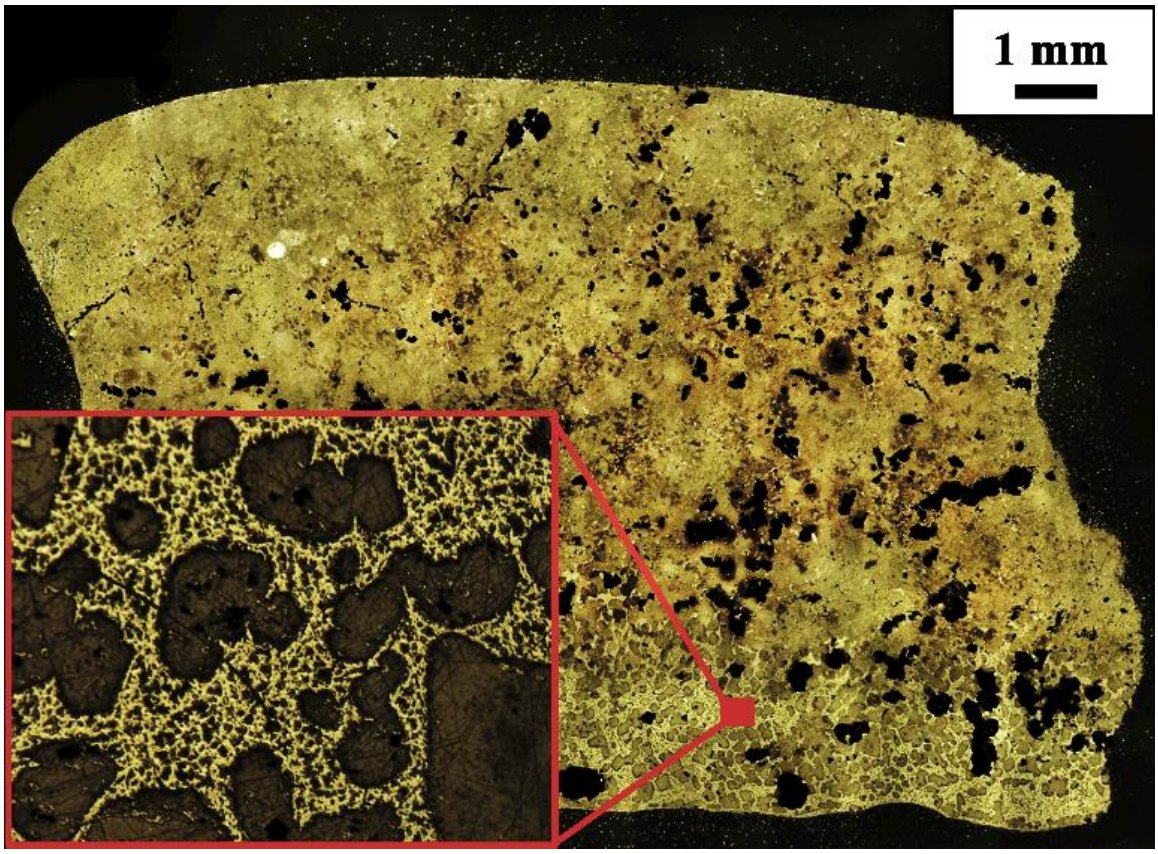

Figure 3.31 Cross-section of ingot showing Bi preference on one edge. The inset shows MnBi islands in a matrix of Bi (Bi-rich region of MnBi formed due to blockage of Bi extraction).

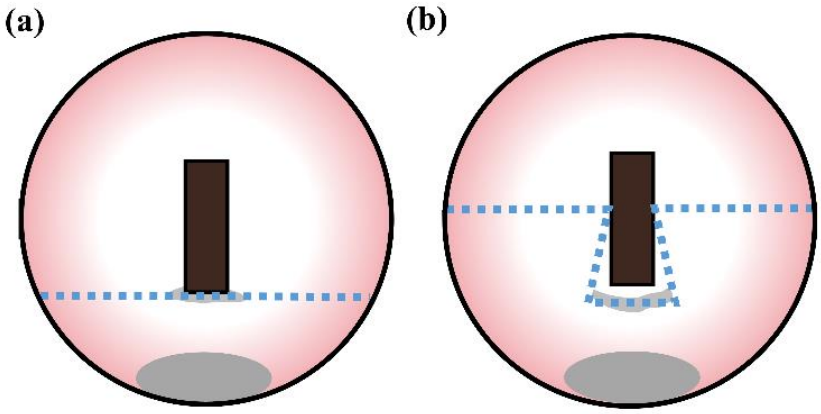

Figure 3.32 Diagram of the vacuum-annealing chamber with ingots (a) placed atop a stainless steel mesh (b) suspended by a fixture made of stainless steel mesh. When suspended, bismuth can freely flow away from the ingot.

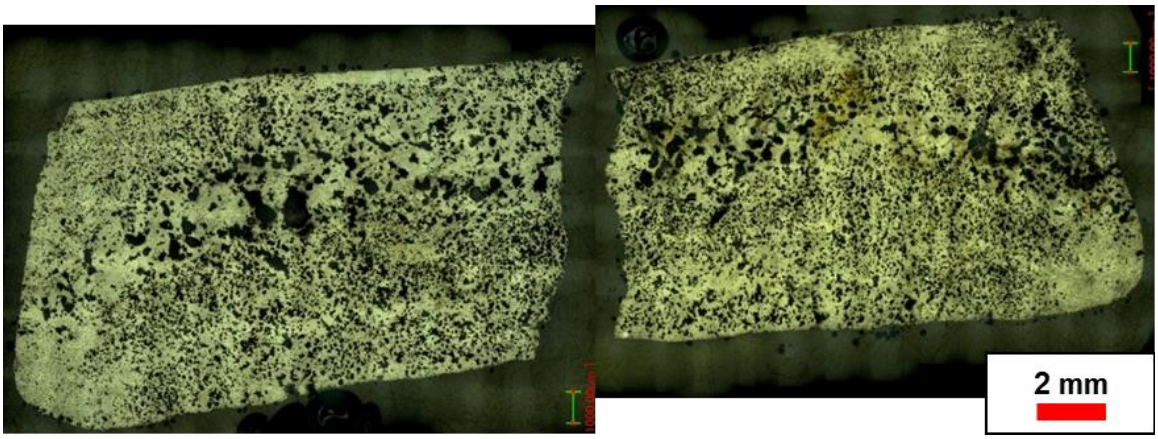

Figure 3.33 The full cross-section of a vacuum-annealed ingot showing little Bi content but high porosity.

Optical micrographs were digitally stitched in order to show the full cross-section of the vacuum-annealed ingot in which all bismuth has been extracted (Figure 3.33). However, a depth profile in Figure 3.34 shows that the majority of dark regions in the post-annealed ingot are concave below the ingot surface, which implies that they are voids. Most pores are large enough to be observed without the aid of a microscope. The porosity is not uniform and does not appear to occur in particular locations.

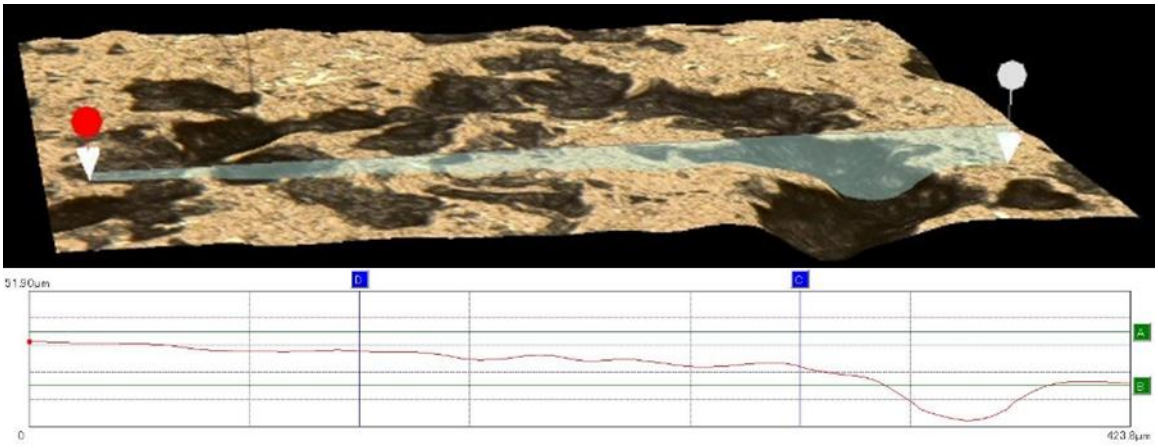

Figure 3.34 Depth profile using of the vacuum-annealed ingot obtained by using a digital optical microscope in which the software detects areas that are in focus.

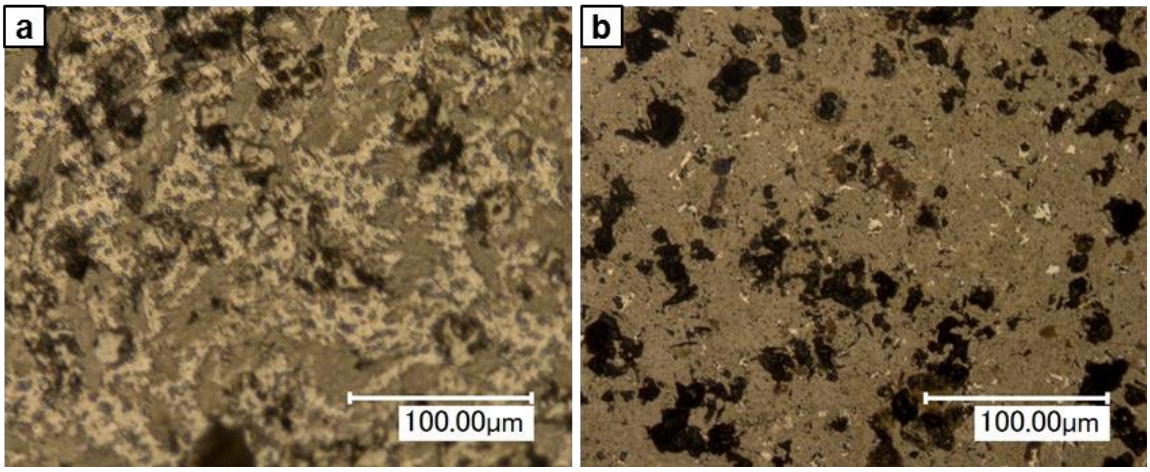

Figure 3.35 Cross-sectional optical microscopy of an arc-melted MnBi ingot, (a) before and, (b) after vacuum-annealing at 400X magnification. After vacuum-annealing, the dark phase has increased at the expense of the light phase.

The ingot before and after the vacuum-annealing can be observed in the cross-sectional optical micrographs taken near the center of the ingots (Figure 3.35). The micrographs show an increased amount of black regions (manganese or pores) and a decreased amount of white regions (bismuth) after vacuum-annealing. These micrographs show that the vacuum-annealing process promotes the formation of MnBi phase, reduces the fraction of Bi phase, and increases the sample porosity.

The magnetization curves of the vacuum-annealed ingot, argon-annealed ingot, and as-cast ingot are plotted in Figure 3.36. These ingots have M_S of 72 emu/g, 43 emu/g, and 28 emu/g, respectively. M_S of 72 emu/g is among the highest achieved in bulk MnBi, where 43 emu/g is typical. This is close to the best M_S achieved by chill-casting.

The fraction of low-temperature phase MnBi can be determined by comparing the measured M_S to the theoretical M_S of 80 emu/g since the other significant phases (Mn, Bi, void) have negligible contribution to the magnetic moment. Combining these values

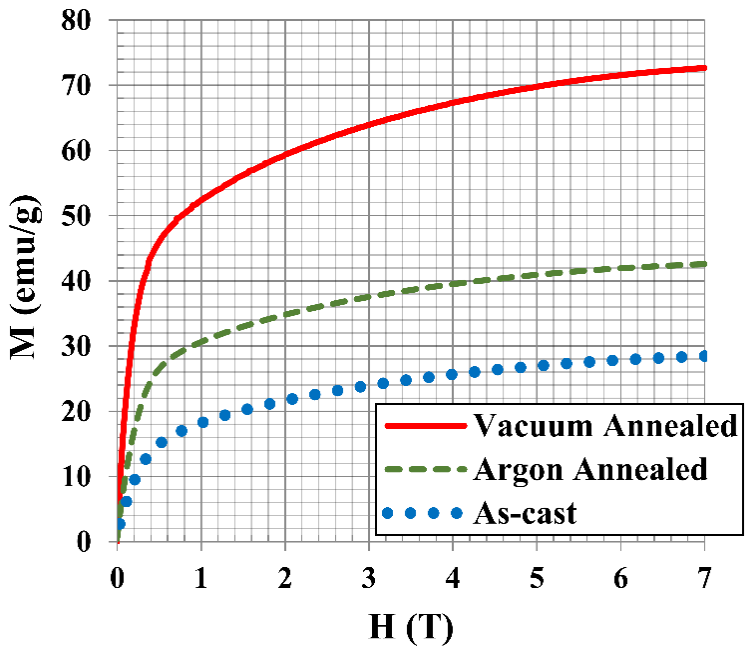

Figure 3.36 Magnetization curves of arc-melted MnBi ingots as-cast (pre-annealed), annealed in argon, and annealed in high vacuum.

with the measured density, the relative phase quantities are calculated, listed in Table 3.1, and depicted in Figure 3.37.

The pre-annealed, as-cast ingot is determined from M_S to consist of 35 wt % MnBi. Since the nominal composition of the ingot is known, the relative weight fractions of the non-magnetic phases can also be determined. Using the densities of the constituent phases, the weight fractions can be converted into volume fractions, and the overall ingot density can be determined. Here, the ingot is assumed to be 100% dense (no voids), which is reasonable for arc-melted ingots. The calculated density of the ingot is 9.05 g/cc. When this density is experimentally measured, a value of 9.02 g/cc is obtained. For reference, the "ideal formation", the highest achievable fraction of MnBi using the starting composition of 52.4 at % Mn, is determined to have M_S of 78.4 emu/g. The value

Table 3.1 Relative fractions of phases in arc-melted MnBi ingots.

	wt % MnBi	wt % Mn	wt % Bi	wt % MnBi (formed)	vol % Mn	vol % Bi	vol % MnBi	vol % voids	projected density (g/cc)
(a) Pre-Annealed	35.00*	15.15	49.85	0.00	18.44	45.98	35.57	0.00	9.05
(b) Ideal Formation	97.96	2.04	0.00	62.96	2.43	0.00	97.57	0.00	8.86
(c) Argon-annealed	53.75*	11.24	35.01	18.75	13.61	32.09	54.30	0.00	8.99
(d) Vacuum-annealed	90.00*	6.21	3.79	30.23	6.70	3.10	81.05	9.15	8.02*

** measured values (density or from M_S)*

is lower than pure MnBi because of the excess manganese that cannot be removed from the ingot by any annealing process. The pre-annealed ingot would require 62.96 wt % of additional MnBi to be formed (Table 3.1, fourth column) in order to achieve this "ideal formation". The argon-annealed ingot, comparable to typical bulk MnBi, has formed only an additional 18.75 wt % MnBi due to the slow diffusion. [11]

The vacuum-annealed ingot has M_S that is further increased by means of removing non-magnetic Bi. However, the phases of the vacuum-annealed ingot cannot be determined by previous means because the amount of Bi remaining in the ingot is unknown. Since the shape and volume of the ingot remained nominally unchanged after vacuum-annealing, the voids in the ingot are thus formed from vacated Bi, and so the volume of porosity is equivalent to the volume of Bi removed. The density of the ingot can be measured in order to determine the fraction of Bi remaining in the ingot. In addition, Table 3.1 shows that total removal of the Bi phase from either the pre-annealed or argon-annealed ingots would not sufficiently increase M_S – additional MnBi must be formed in both cases. The final proportion of phases is thus a balance between the

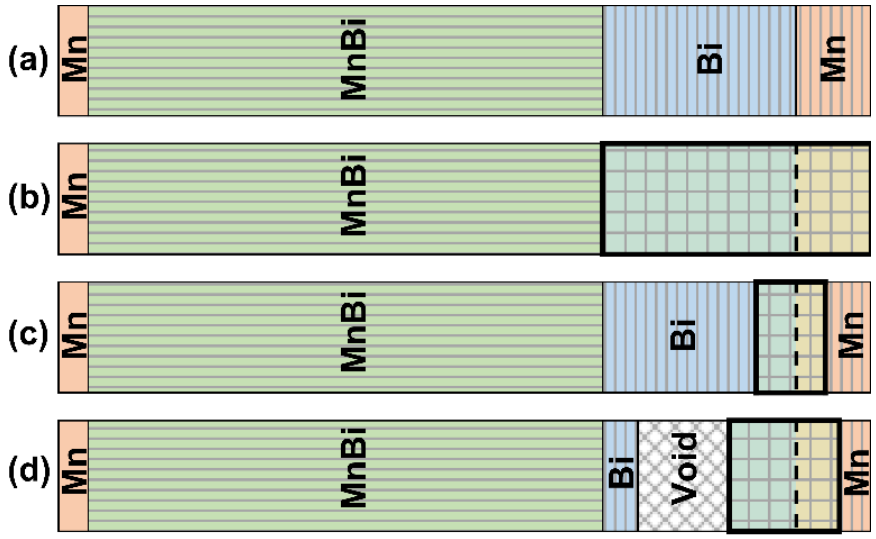

Figure 3.37 Volume fractions of phases in (a) as-cast, (b) "ideal", (c) argon-annealed, and (d) vacuum-annealed ingots. Excess Mn (left) is partitioned from unreacted Mn (right). MnBi that is formed relative to the as-cast ingot boxed by a bold outline. The Bi and Mn portions that react to form this additional MnBi is separated by a dashed line.

amount of MnBi formed at the expense of unreacted Mn and Bi phases (increasing net density and moment) and the amount of Bi extracted (decreasing net density while also increasing net magnetization). The resulting density is 7.81 g/cc, indicating 3.79 wt % Bi, 11.4 vol. % porosity, and a MnBi formation of 30.23 wt % relative to the pre-annealed ingot. The significant increase in the formation of MnBi compared to the argon-annealing is attributed to the increased opportunities for Bi to react with Mn as it is being extracted from the ingot. The volume percentages generally agree with the areal fractions observed in Figure 3.35b.

When vacuum-annealed ingots for varying composition are compared, all ingots show a large increase in magnetization after vacuum-annealing (Figure 3.38). There does not appear to be a strong magnetic correlation with composition. From the discussion above, this would imply that when the Mn composition is raised, it makes for a higher

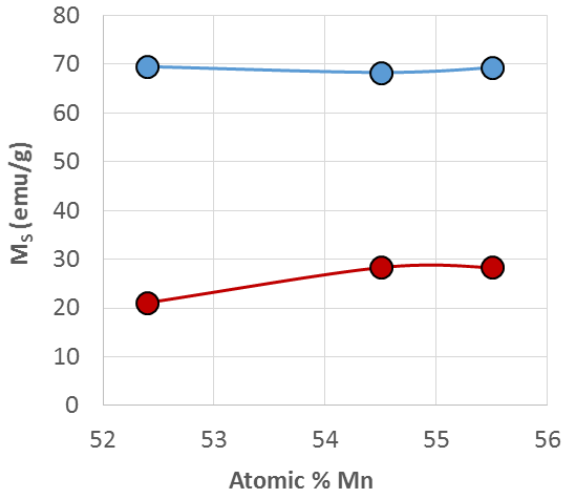

Figure 3.38 Saturation magnetization of vacuum-annealed ingots for various compositions before (red) and after (blue) vacuum-annealing. All compositions increase to about 70 emu/g after vacuum-annealing.

amount of molten Bi that is flowing to react. Therefore, slightly more reaction occurs and, the increase in Mn content is negligible.

3.3.2 MnBi Particles

3.3.2.1 High Energy Density Particles & Characterization

The phases of the as-sparked and annealed powders were studied by observing the powder x-ray diffraction patterns shown in Figure 3.39. Both powder samples show all lines of LTP-MnBi[10] and Bi phases. The diffraction pattern of the as-sparked powder is dominated by the Bi phase, with LTP-MnBi as the minority phase. The annealed powder shows a dramatic rise of the LTP-MnBi major line, now the dominant phase. A weak

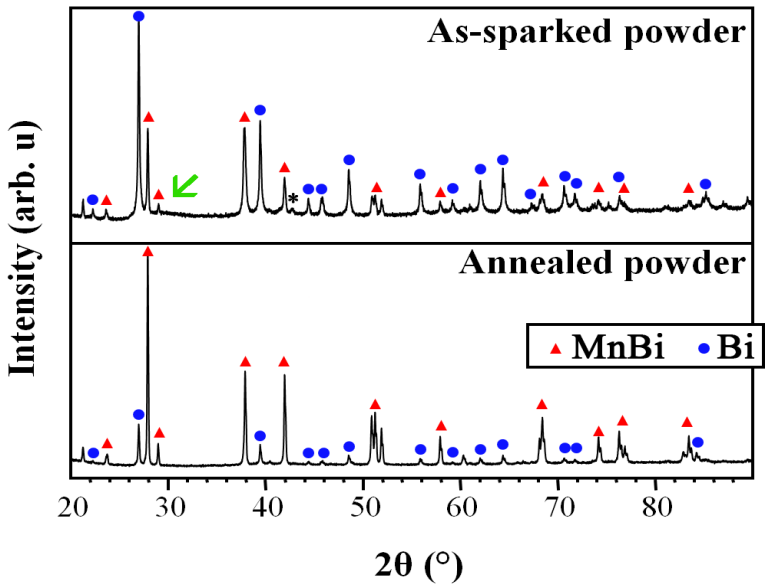

Figure 3.39 Powder x-ray diffraction patterns for as-sparked and annealed powders. The arrow (↙) points to the amorphous background. The asterisk (*) represents the lone Mn peak. Annealing greatly enhances the MnBi peaks.

amorphous background can be seen in the as-sparked powder around 2θ = 28°. This background lies under the line representing the (002) plane, a low-order d-spacing, as expected in amorphous metals. This is consistent with work by Guo *et al*[11] on the diffraction pattern of amorphous MnBi formed by melt spinning and is expected in a rapid quench technique of spark erosion.

All lines in the annealed powder are narrower than those of the as-sparked powder. A simple strain plot of the FWHMs estimates internal strain to be negligible in both patterns, and thus broadened lines are suspected to be due only to crystallite size. By using the Scherrer equation, the crystallite size of MnBi and Bi in the as-sparked powder is determined to be 42 nm and 37 nm, respectively. The crystallite sizes of the annealed powder are calculated to be 71 nm and 62 nm for MnBi and Bi, respectively. These values indicate significant crystallite growth during the short, low temperature anneal.

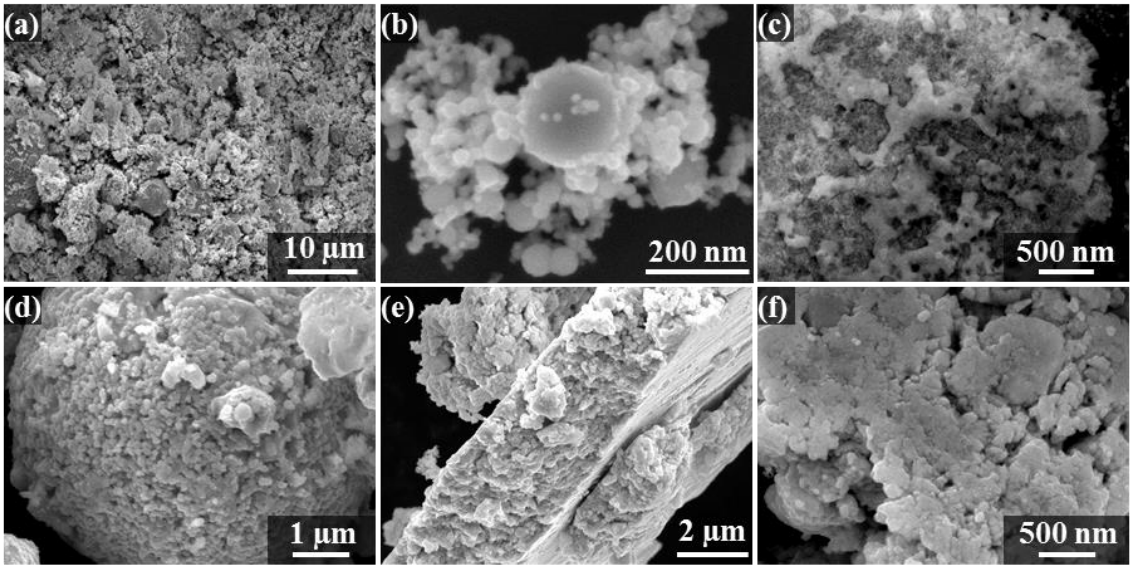

Figure 3.40 SEM images of (a) as-sparked powder at low magnification, (b) as-sparked powder at high magnification, (c) cross-section of a sphere in the as-sparked powder, (d) cluster of the annealed powder, (e) edge of a platelet produced by milling, and (f) milled powder at high magnification.

Figure 3.40(a) shows a macroscopic image of the as-sparked powder with a distribution of particle, aggregate, and cluster sizes. From this coarse magnification, there appear to be large textured clusters of irregularly shaped aggregates as well as some fraction of large spheres. Upon closer examination in Figure 3.40(b), these smaller clusters can be resolved to show that they consist of spheroidal nanoparticles 20-50 nm in diameter, below the single-domain particle size.[19] These appear to constitute the major volume of the sample. Figure 3.40(c) shows the cross-section of a sphere, which appears to be porous and made up of finer particles. It is unclear whether multi-domain particles exist within these spheres.

When the powder is annealed, the loosely bound aggregates form denser clusters as seen in Figure 3.40(d), assisted by increased dipolar interactions upon crystallization

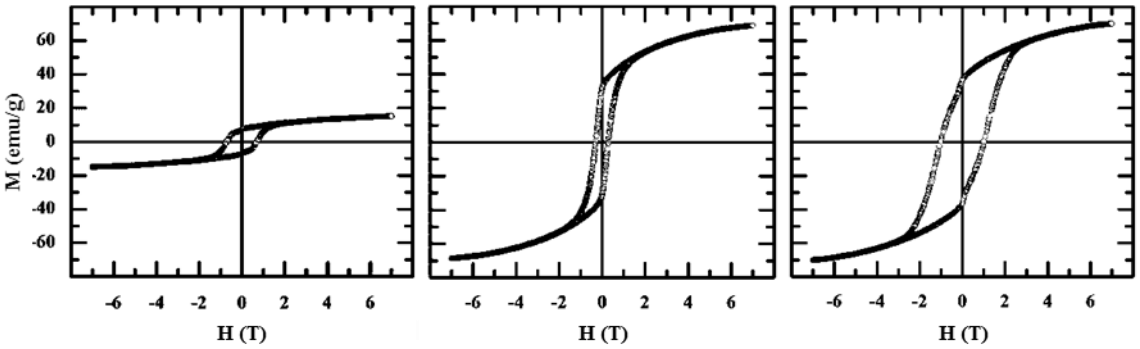

Figure 3.41 M-H loops of (a) as-sparked, (b) annealed, and (c) annealed + milled spark-eroded MnBi powders at room temperature. The annealed and milled powder demonstrates a $(BH)_{MAX}$ of 3.0 MGOe.

of the non-magnetic amorphous particles into single domains. The nanoscale features are retained, albeit with some necking among the nanoparticles. This structural change is somewhat surprising given the short annealing time and low temperature of the heat treatment. When milled, the powder sample forms into platelets of varying size and about 2 μm in thickness. The edge of a platelet is seen in Figure 3.40(e) and is representative of the entire sample. Still, the platelets can be seen to be made up of tightly-packed nanoparticles.

Figure 3.41 shows the hysteresis loops measured for the as-sparked, annealed, and milled particles. The as-sparked powders have M_S of 15 emu/g at room temperature in 7 T. After annealing, M_S increases to 69 emu/g, which implies that the sample is > 90 % LTP-MnBi.[17] When the annealed powder is milled, M_S remains unchanged though H_C increases. This milled powder exhibits a $(BH)_{MAX}$ of 3.0 MGOe, a large value for a randomly oriented sample. High magnetization is critical to achieving this value – care must be taken to assure that particles do not oxidize and are not contaminated during

milling. Additionally, the milling proceeded at relatively low energy so to avoid phase segregation of Bi often observed in ball-milling.[20]

H_C of the as-sparked powder is 0.7 T at room temperature, lower than the anisotropy field of MnBi[8]. This reduction may be due to the presence of multi-domain, amorphous, or superparamagnetic particles. After annealing, the particle necking seen in Figure 3.40(d) increases exchange interactions, thereby reducing H_C to 0.4 T. Grain growth of multi-domain particles, suggested by the diffraction pattern (Figure 3.39), would also reduce H_C When milled, the necking bonds are broken, which increases the sample H_C to 1.0 T.

The dramatic increase in M_S with only a very short, low-temperature anneal is the result of an amorphous to crystalline transformation[21] indicating that the majority of the as-sparked powder is amorphous. Given the size and volume fraction, it would appear

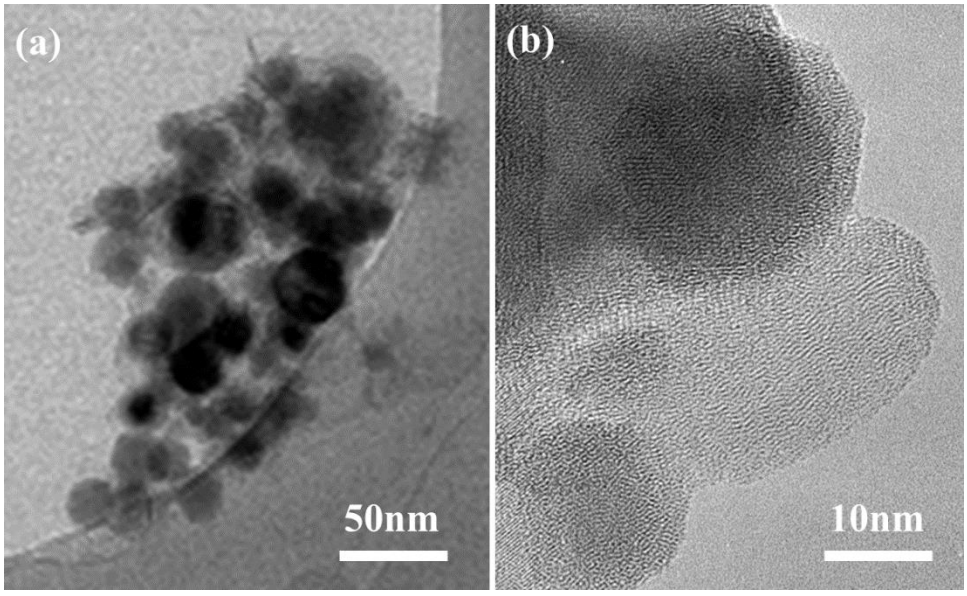

Figure 3.42 Transmission electron micrographs of as-sparked particles at (a) lower magnification and (b) higher magnification, showing lattice fringes ending abruptly, changing orientation, etc., indicating poor crystallization.

that the nanoparticles in Figure 3.40(b) are the amorphous component in the as-sparked powder. Figure 3.42 shows transmission electron micrographs of some of the as-sparked nanoparticles. Some irregularly crystallized particles are shown in Fig. 4.42(b), in which lattice fringes end abruptly, change orientation, etc.

In order to characterize the superparamagnetic component in the spark-eroded and annealed powders, ZFC/FC curves were measured (Figure 3.43). The mean blocking temperature, T_B, which is proportional to the particle volume, is the maximum of the ZFC. The as-sparked powder shows T_B of about 135 K while the annealed powder shows T_B of about 125 K. The smaller mean T_B in the annealed sample may be due to the crystallization of smaller amorphous particles.

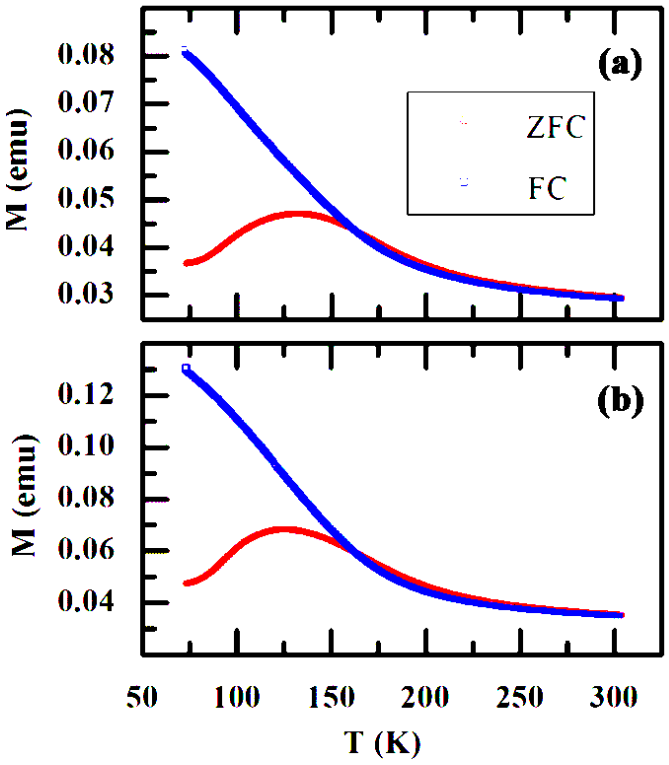

Figure 3.43 Zero-field-cooled and Field-cooled curves for (a) as-sparked and (b) annealed powders confirming a presence of a very small fraction of superparamagnetic particles.

M_r of these powder samples is about half of M_S. This is the expected value for randomly-oriented, single-domain particles, suggesting that any superparamagnetic fraction is small.

Chemical analyses were about the same for as-sparked and annealed samples. The oxygen content was 1.46 ± 0.27 wt %, and the Mn/Bi wt % ratio was 21.5/78.5 ± 1 wt %. Using the M_S measured in Figure. 4.41(b) for the annealed sample, the LTP-MnBi phase can be estimated at 90.9 wt % with 0 % amorphous phase. Thus, the remaining 9.1 % is calculated to be 5.4 wt % Bi phases and 3.7 wt % Mn phases, with oxides able to form with either element. Assuming no Bi-oxide, the relative integrated intensity ratios of the max peaks of MnBi and Bi can be determined from the diffraction pattern of the annealed sample. Using this ratio from the diffraction pattern of the as-sparked sample, the amorphous fraction is calculated to be 50-60 wt %, which is consistent with the magnetic measurements.

Even though only 3.7 wt % Mn phase is estimated for the annealed sample, it is surprising that no Mn-based peaks can be seen in the XRD pattern. A single Mn peak representing the (330) plane can be seen in the diffraction pattern of the as-sparked powder, in which the Mn phase is estimated to be about 8 wt %.

The temperature dependence of H_C is plotted in Figure 3.44 for the annealed and lightly-milled powders. In the milled sample, H_C reaches 2 T at 400 K and is maximum at 540 K, which is in agreement with other reports[15, 16]. The annealed sample follows the same trend, but is displaced by a constant value. The constant displacement indicates that the increased H_C of the milled sample is due to the dispersion of the aggregated particles.

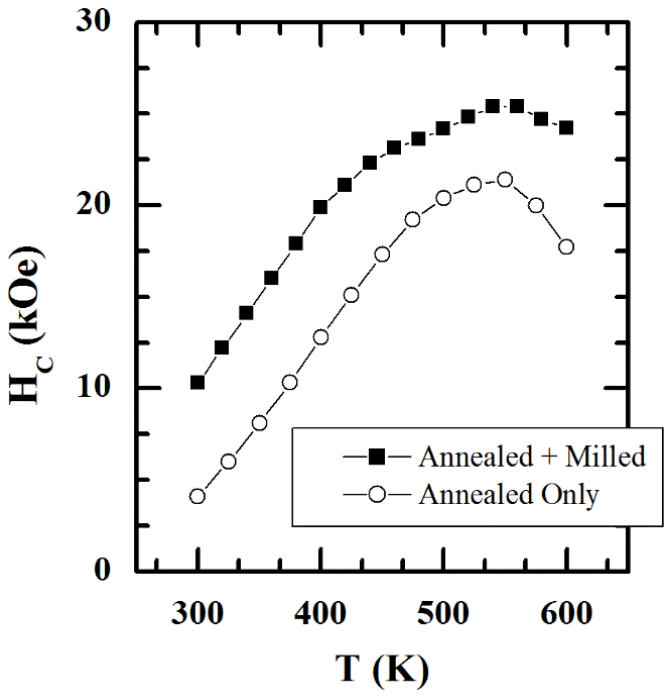

Figure 3.44 Coercive force versus temperature for annealed and milled powders demonstrating a positive temperature coefficient of coercivity.

The yield for spark-eroded single domain particles of MnBi offers an impressive economic advantage over other preparation methods. All of the powders reported here were made in the 10 cm diameter laboratory cell illustrated in Figure A.2. The yield for the powders discussed was > 100 g/hr. Under optimized conditions, MnBi has since been spark-eroded with a yield of ≈ 360 g/hr in the same 10 cm diameter cell. Considering that it has been shown that spark erosion is a readily scalable technique with high energy efficiency[22], with only modest processing required to obtain optimum properties, it seems likely that this production technique should be very competitive in the marketplace.

3.3.2.2 Effects of Ball-Milling of Spark-Eroded Powder

The milling of spark-eroded particles offers a way to enhance their magnetic properties, as previously shown, by breaking apart slight-attached clusters. The milling of spark-eroded particles is different from milling the bulk due to the fine particle size and structure. As been shown, even a light milling provides enough energy to change macroscopic properties.

Figure 3.45 shows the hysteresis loops for spark-eroded particles that have been ball-milled for 19 hours. As previously noted, H_C increased to 2 T at room temperature for randomly-oriented particles. The large increase in H_C is like due primarily to the breaking of clusters. The energy of milling was sufficient to crystallize some of the amorphous powder, thereby increasing M_S by 50%. The XRD patterns for both powders

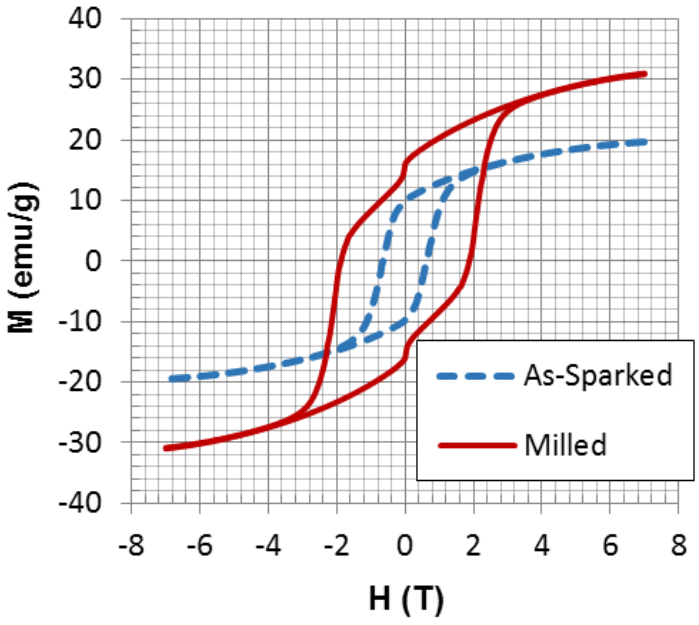

Figure 3.45 M-H loops for spark-eroded MnBi before and after 19 hours of ball-milling. Ball milling increases both M_S and H_C of as-sparked powder.

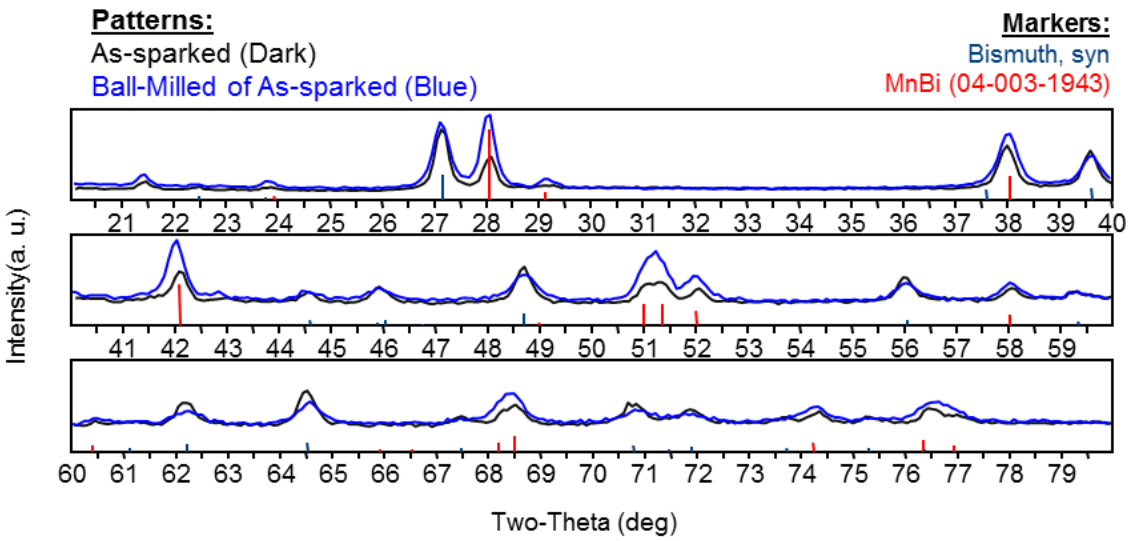

Figure 3.46 XRD Patterns for spark-eroded MnBi before and after ball-milling. Ball-milling increases the intensity of MnBi peaks.

are shown in Figure 3.46. There is an increase of peak intensities in the LTP-MnBi peaks relative to Bi peaks.

When this milled powder is annealed, M_S is lower than that of annealed powder that has not been milled (Figure 3.47), and H_C drops to 1 T. When the annealed powder is milled, the same drop in M_S is observed, but H_C is 2 T. Since measures were taken in preventing oxidation during milling, the lower M_S is due to irreversible phase segregation that occurs during ball-milling, which has previously been reported[20], or more likely, due to the separation of aggregates, which creates magnetically disordered surfaces. The SEM images in Figure 3.48 of the powder milled and annealed, and the reverse, show some necking of the particles when annealing is last. This is a major reason for the difference in H_C.

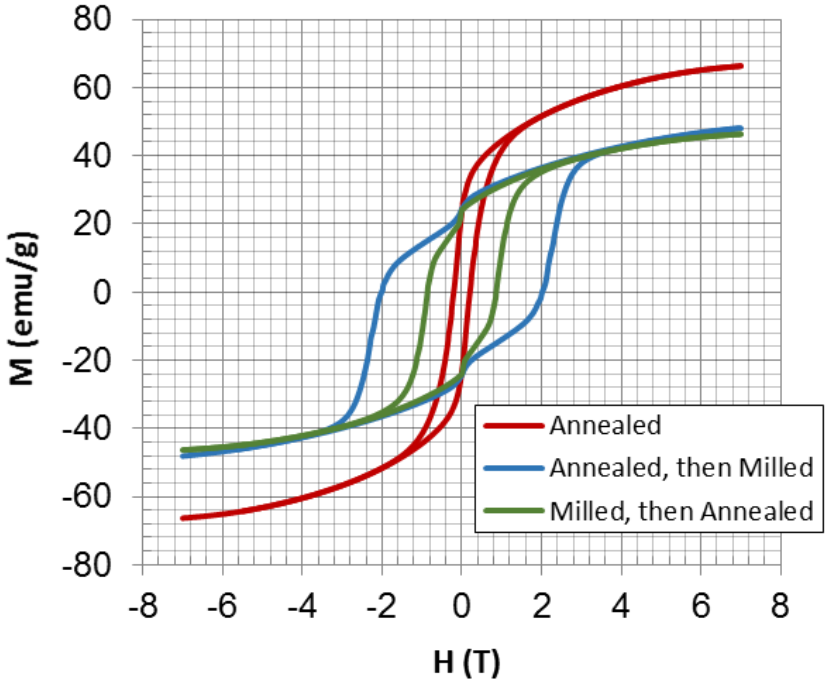

Figure 3.47 M-H loops for spark-eroded MnBi annealed, annealed then milled, and milled then annealed. Ball-milling inherently reduces M_S whether performed before or after annealing. Annealing reduces H_C of a milled sample to 1 T, while milling increases H_C of an annealed sample to 2 T.

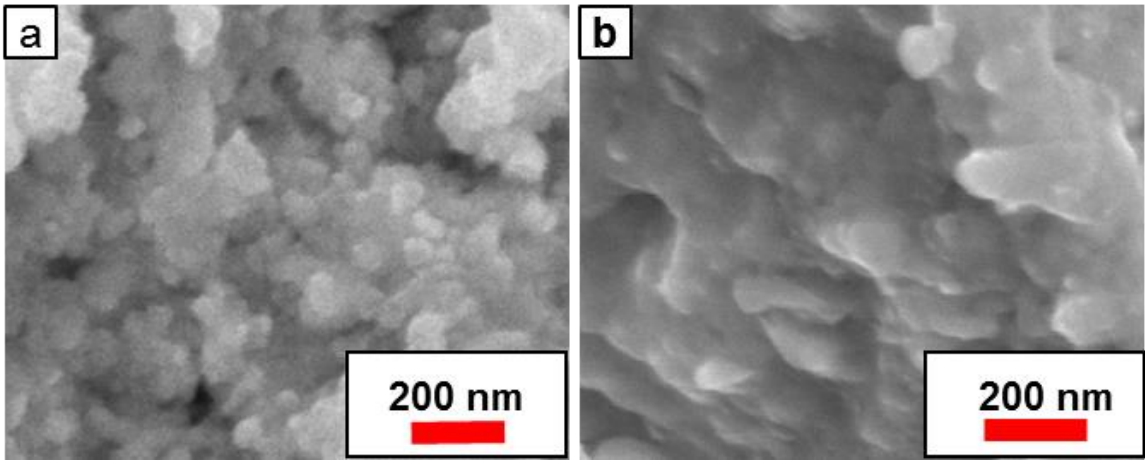

Figure 3.48 SEM imaged for spark-eroded MnBi (a) annealed then milled, and (b) milled then annealed. When annealing is the final step, there is evidence of necking.

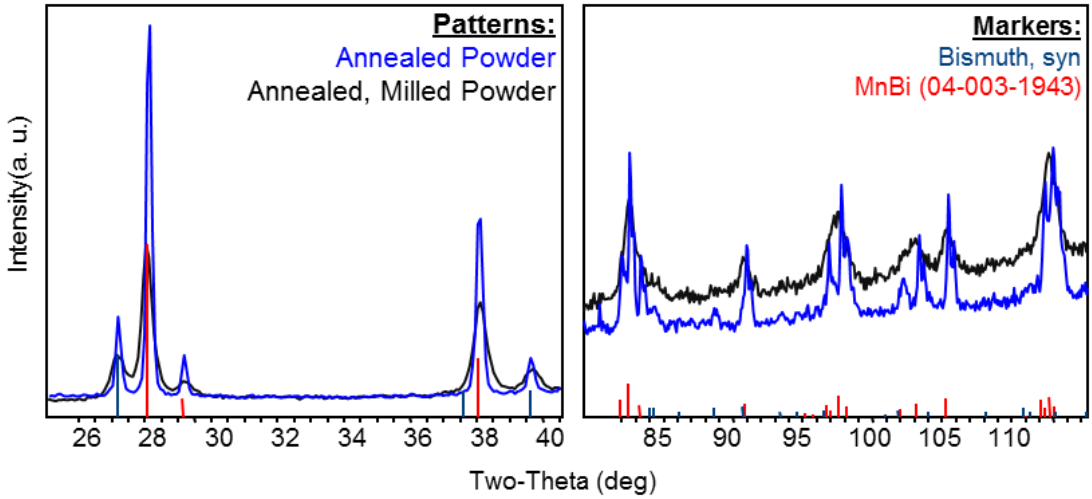

Figure 3.49 XRD Patterns for annealed spark-eroded MnBi before and after ball-milling. Milling broadens peaks and reduces the intensity of MnBi peaks.

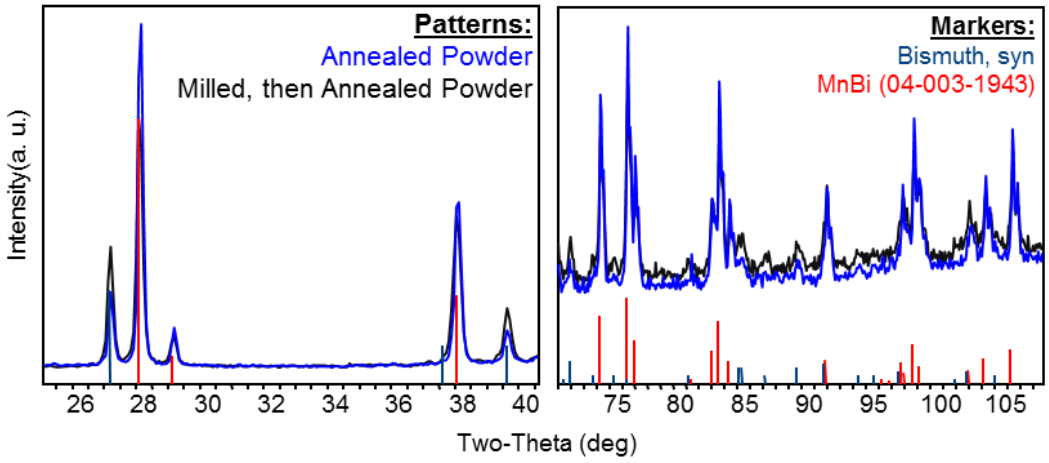

Figure 3.50 XRD Patterns for annealed spark-eroded MnBi powder that has and has not been milled. The milled sample has reduced MnBi peaks that could not be restored by annealing.

The XRD patterns for the annealed powder before and after ball-balling are shown in Figure 3.49. The ball-milled peaks are broadened. The diffraction pattern of the annealed powder shows several peaks that cannot be seen in the ball-milled powder due to broadening. No additional peaks can be identified in the region. All of these peaks can

be identified as Bi or LTP-MnBi. Similarly, Figure 3.50 shows the XRD patterns for spark-eroded powder that has been annealed and the same powder that has been ball-milled before annealing (annealed versus milled, then annealed). The patterns show that all peaks are distinct and not broadened. Additionally, the ratio of Bi to LTP-MnBi appears to have increased when the sample is ball-milled before annealing. This is may be evidence that milling causes some phase segregation.

3.3.2.3 Surface Dead Layer

As was shown in Figure 3.21, the properties of spark-eroded powder depend on those of the starting charge material. The correlation, however, is rather complex. It has been found that while vacuum-annealed arc-melted ingots exhibit the same M_S as chill-cast ingots, when the arc-melted ingots are spark-eroded, the resulting powder had M_S ~ 58 emu/g, far less than the anticipated 70 emu/g powder that was previously achieved by spark-eroding chill-cast ingots with high M_S. Figure 3.51 shows the demagnetization curves for several spark-eroded powders that have been made from vacuum-annealed ingots with high M_S.

The lower moment is not believed to be due to processing, but to a difference in the target material that leads to different properties in the spark erosion yield. The possible reasons for the decreased moment are as follows:

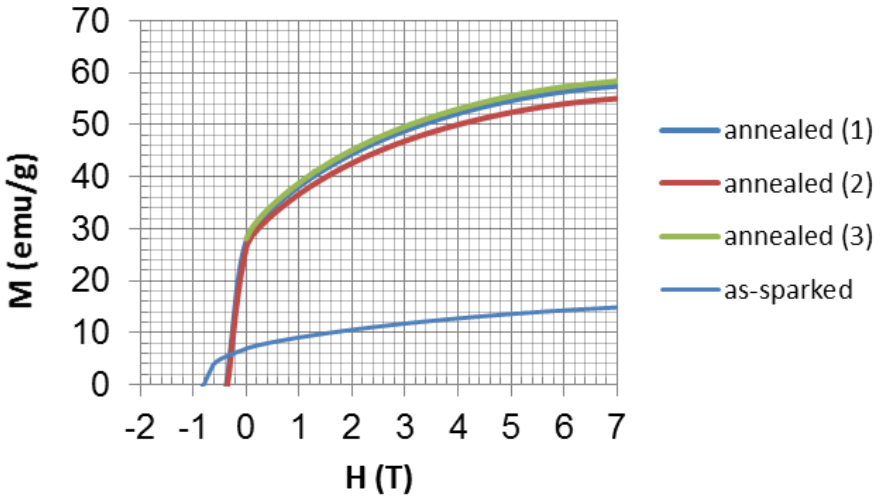

Figure 3.51 Demagnetization curves for the spark-eroded powders made from vacuum-annealed ingots, and after annealing, demonstrating generally lower than expected M_S from a starting ingot with M_S of 72 emu/g.

1) **Phase segregation.** At 72 emu/g, bulk ingots, whether arc-melted or chill-cast contain about 10 weight percent non-magnetic phases. Since the high M_S of chill-cast ingots are a result of MnBi formation alone, all phases are likely in close proximity. Thus, a spark plasma may affect a macroscopic area that consists of fine, unreacted, non-magnetic Bi and Mn phases, which helps to homogenize this region and produce more pure MnBi. The vacuum-annealed ingot, however, is porous due to phase migration during the Bi extraction process. This migration could lead to dispersion of non-magnetic phases in the ingot that remain unreacted in the yield.
2) **Oxidation.** When Bi is extracted from the bulk ingot by vacuum, voids remain. When removed from the annealing chamber, these voids may slowly fill with air (previously identified as 11 percent by volume). When this bulk is spark-eroded, they are submersed in liquid nitrogen, perhaps trapping the air and allowing some

level of oxidation to occur during the spark erosion process. XRD, however, was unable to identify any oxide peaks.

3) **Surface effects.** The surfaces of fine ferromagnetic particles often do not contribute to the magnetic moment due to their magnetically disordered surfaces. If we consider a thin magnetically "dead" layer that surrounds each MnBi particle, then the magnetization will decrease as the average particle size decreases. This is governed by the following equation:

$$\frac{M}{M_S} = \left(1 - \frac{t}{R}\right)^3 \tag{4.2}$$

If the dead layer thickness is taken to be the c lattice parameter of hexagonal MnBi[23], then it can be seen that the "dead layer" has a large effect on particles 20~30 nm in diameter in Figure 3.52.

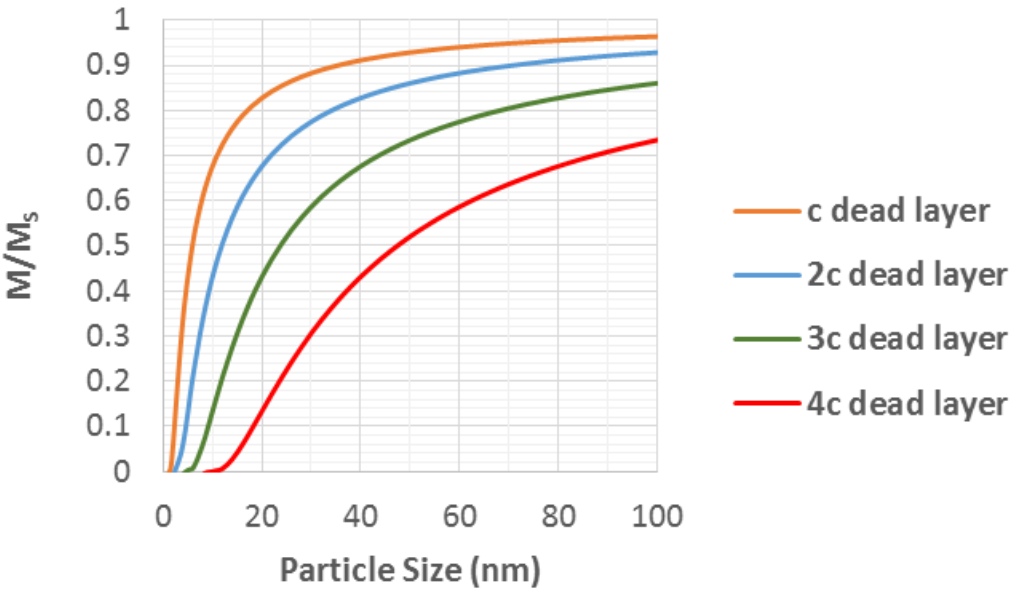

Figure 3.52 Effect on the magnetization of a MnBi particle (diameter) for various "dead" layer thicknesses (multiples of hexagonal c-lattice parameter).

3.3.3 Magnetic Alignment

3.3.3.1 Partially-Aligned Compacts by Annealing in a Field

When green compacts of spark-eroded MnBi particles are crystallized by annealing in 3 T, the resulting compact is partially aligned crystallographically. Figure 3.53 shows the M-H loops of the compact before and after annealing in a magnetic field. Before annealing, the green compact properties are similar to that of as-sparked powder, as expected. After the compact was annealed, it was measured with the applied field in the same direction as the annealing field. The resulting M-H loop has an increased "squareness", an increased M_r/M_S ratio of up to 0.8 from a ratio of 0.5 in a randomly-

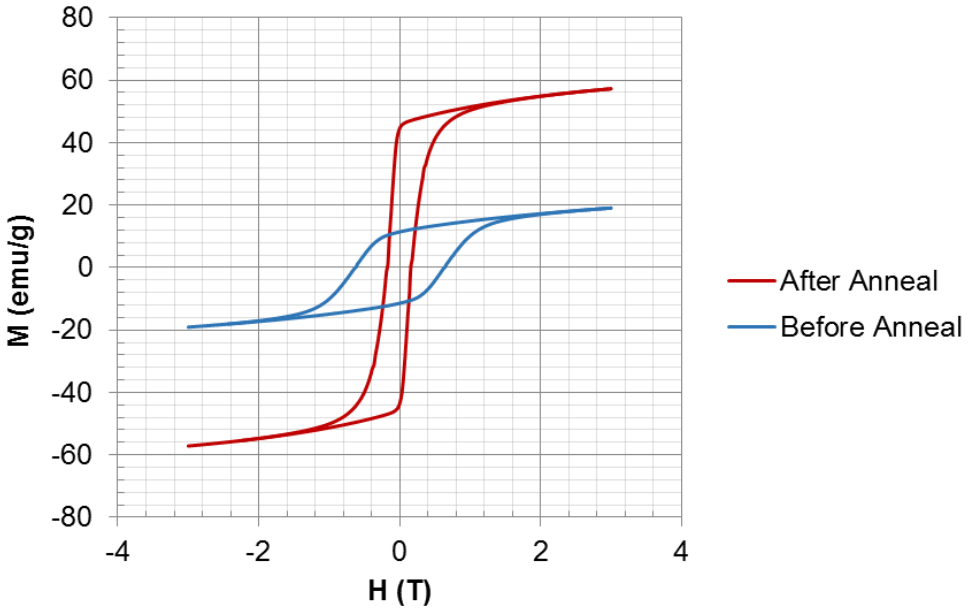

Figure 3.53 M-H loops of a spark-eroded, cold-pressed MnBi sample before and after annealing in a 3 T field. The applied field direction for measuring is the same as the annealing field.

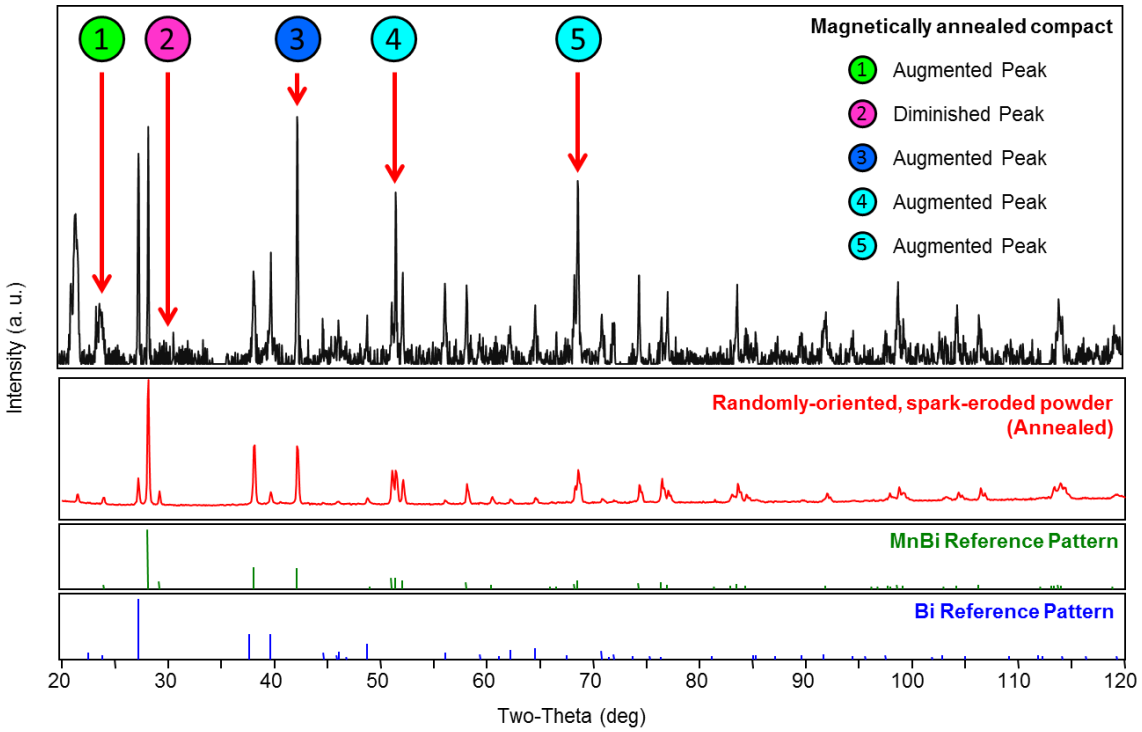

Figure 3.54 XRD pattern of the partially-aligned MnBi compact made from spark-eroded powder. Key peaks are numbered and labeled as augmented or diminished based on whether the peak intensity has increased or decreased relative to other peaks when compared to a randomly-oriented MnBi sample.

oriented sample. This suggests that the compact has been magnetically aligned along the annealing field direction. M_S has also increased by 200% and H_C has decreased, which are both expected from the discussion on annealing in Section 3.3.2.1.

The crystallographic orientation was investigated by XRD. The aligned sample is mounted such that the direction of the alignment is orthogonal to the direction of the x-ray source and detector (See Figure 3.19). The resulting pattern is shown in Figure 3.54. By comparing this pattern to the reference pattern for LTP-MnBi, which is the same for randomly-oriented MnBi powder, it can be seen that certain peak intensities are increased

while others are decreased relative to each other. Key peaks are numbered and labeled as augmented or diminished

The key peaks are indexed and the resulting planes are depicted within the MnBi unit cell in Figure 3.55. The peaks that are augmented suggest that the x-ray radiation is coming from a direction normal to the planes. Likewise, peaks that are diminished represent planes in which the x-ray radiation is parallel to the planes and thus do not

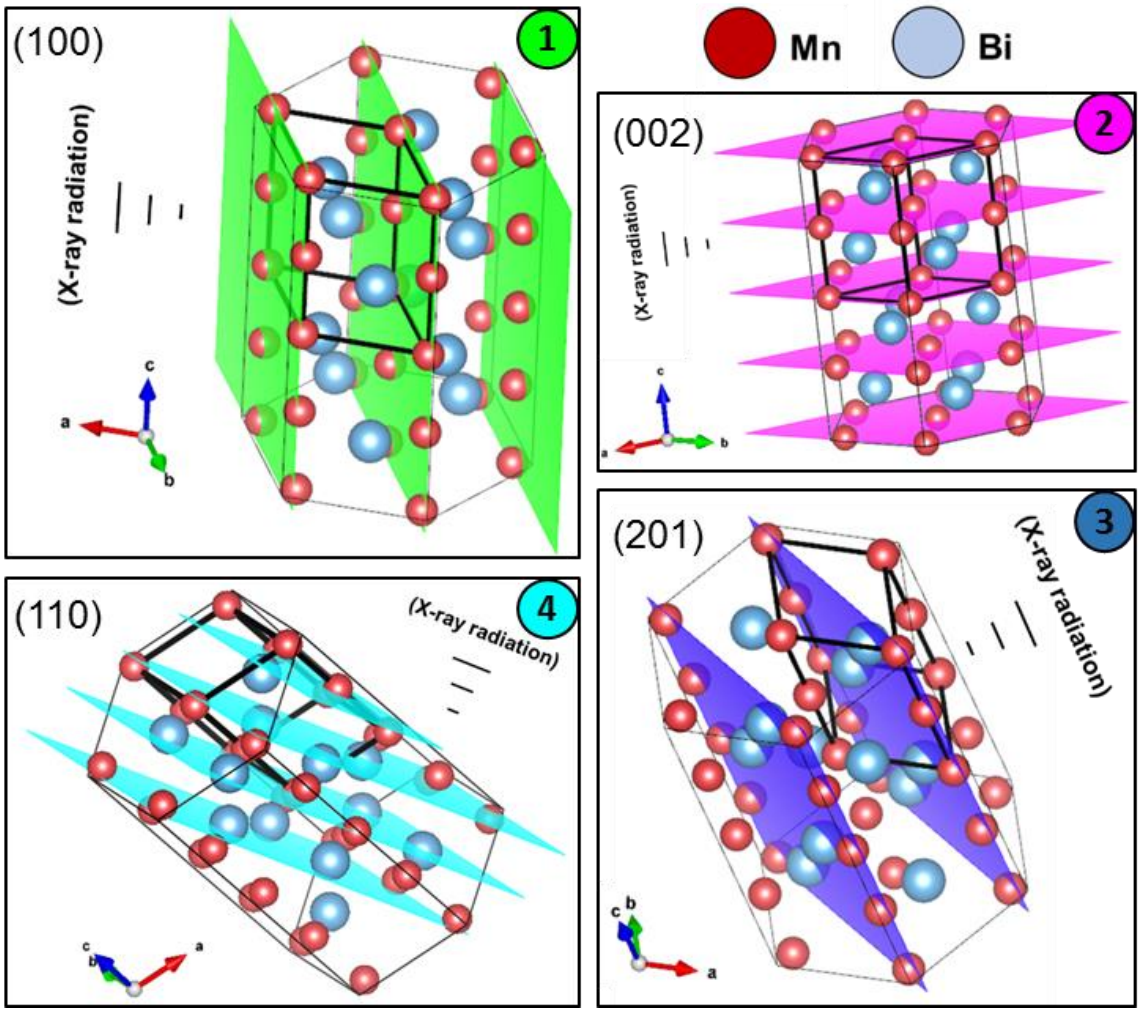

Figure 3.55 The MnBi crystal structure (NiAs structure)[23] showing several atomic planes. The relative position of the x-ray source is suggested based on the corresponding relative peak intensity from the XRD pattern.

diffract. Indexing has identified that the (100), (002), and (110) planes are augmented while the (201) plane is diminished. In Figure 3.55, the location of the x-ray source is determined based on whether the representing peaks were augmented or diminished (e.g. in the (002) plane, since the peak is diminished, the x-ray radiation must come from a direction that is parallel to the planes). Since the location of the x-ray source is known, all changes of the changes in peak intensity suggest that the x-ray radiation is coming from a direction that is orthogonal to the c-axis. This implies that the c-axis is parallel to the sample holder, which is the same direction as the magnetic field during annealing, proving that some crystallographic alignment has been achieved.

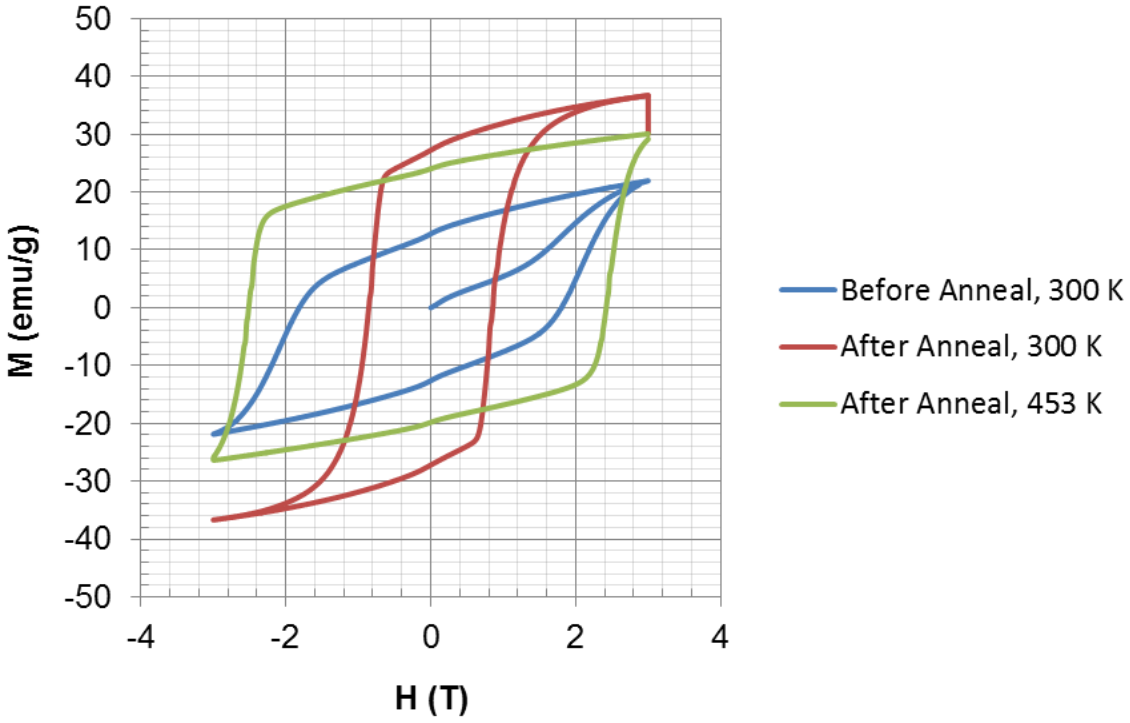

Figure 3.56 M-H loop of spark-eroded, milled, and cold-pressed sample before and after annealing in 3 T field and at higher temperature. The applied field direction for measuring is the same as that for annealing.

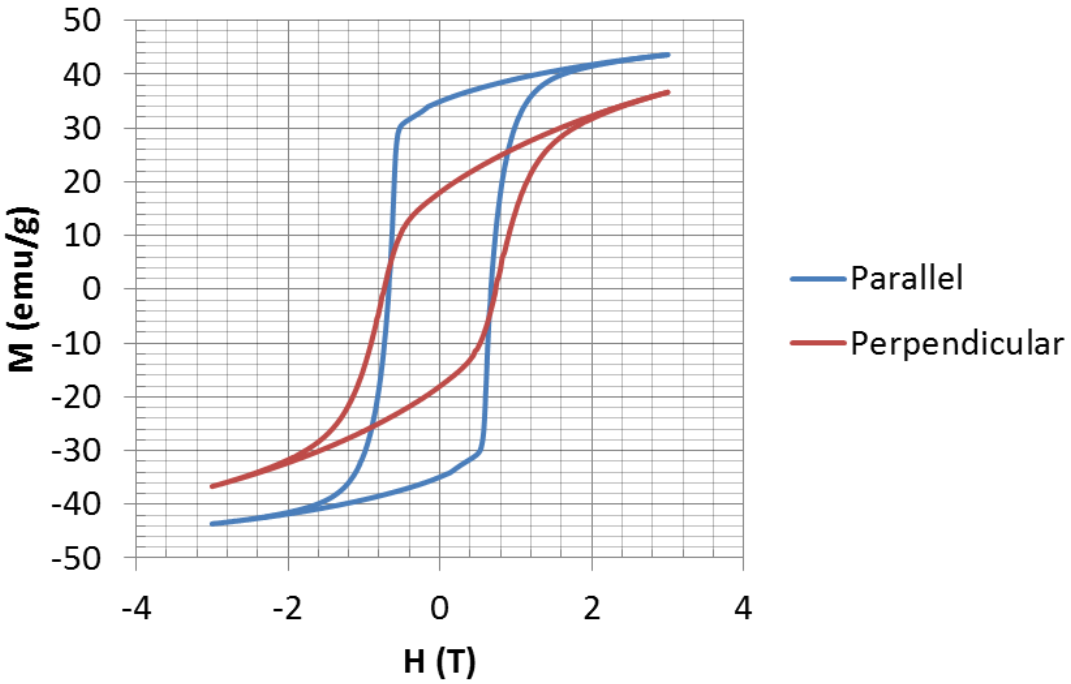

Figure 3.57 Parallel vs. perpendicular measurements on a magnetically aligned compact made from spark-eroded powder that has been milled. The parallel/perpendicular marker indicates the measurement direction relative to the alignment direction.

The same magnetic alignment procedure was performed on spark-eroded MnBi powder that was ball-milled. The resulting M-H loop is shown in Figure 3.56. The characteristic "squareness" is observed in the aligned sample. H_C is about 1 T, the expected value of spark-eroded powder that has been milled and annealed (Section 3.3.2.2). M_S is lower in the milled sample, as expected.

When the sample is rotated 90° such that the direction of alignment is orthogonal to the measurement direction, the resulting M-H loop is shown in Figure 3.57. As expected, the "squareness" is eliminated, and the magnetization is lower.

3.3.3.2 Crystallization Study

The amorphous to crystalline transition can be observed by changes in magnetization during the annealing process (Figure 3.58). At room temperature, the sample magnetization has a non-zero moment due to the crystalline component. This magnetic moment decreases slightly due to the intrinsic temperature dependence of magnetization of MnBi. The magnetization begins to increase near 400 K. The inflection point is near the melting point of Bi where Guo *et al* shows by calorimetry curves is the start of LTP-MnBi formation.[21] The rate of moment increase is maximum at 600 K. Shortly after 600 K paramagnetic HTP forms; this continues until melting near 700K.

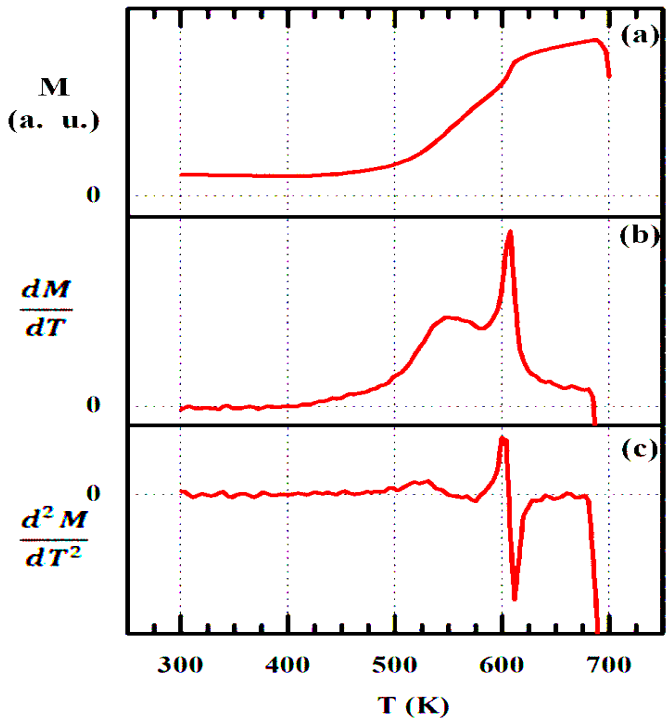

Figure 3.58 (a) Magnetization of as-sparked sample in 50 Oe measured as a function of temperature from 300K to 700 K with a heating rate of 10 K/min. The derivative (b), and second derivative (c) are shown to accentuate changes in magnetization.

3.3.4 Composites (Fe, Co, FeCo)

3.3.4.1 Milled Mixtures

Since milling breaks up clusters and aggregates of spark-eroded MnBi (Section 3.3.2.2), this technique was used to try to obtain an intimate mixture of MnBi particles with soft, high magnetization particles. This would break up aggregates that ultrasonication was unable to accomplish (see Appendix C). Figure 3.59 shows the hysteresis loops of ball-milling annealed, spark-eroded MnBi powder with Fe. Compared to the expected loop (dashed), the moment is lower due to the irreversible milling effects reported in Section 3.3.2.2.

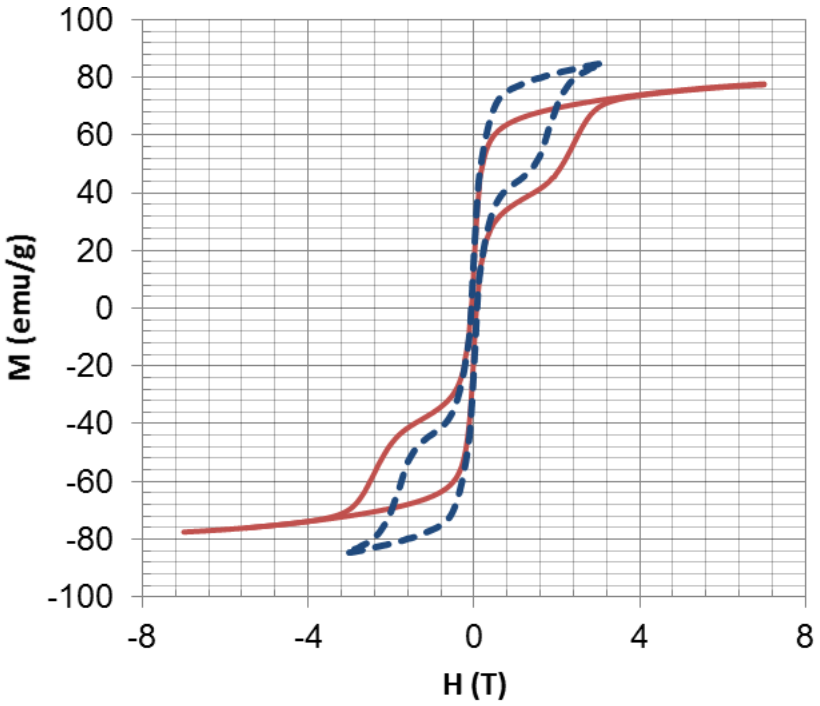

Figure 3.59 Experimental mixture of annealed, spark-eroded MnBi with 10 wt. % spark-eroded Fe after ultrasonication in hexane, compared to theoretical mixture (dotted)

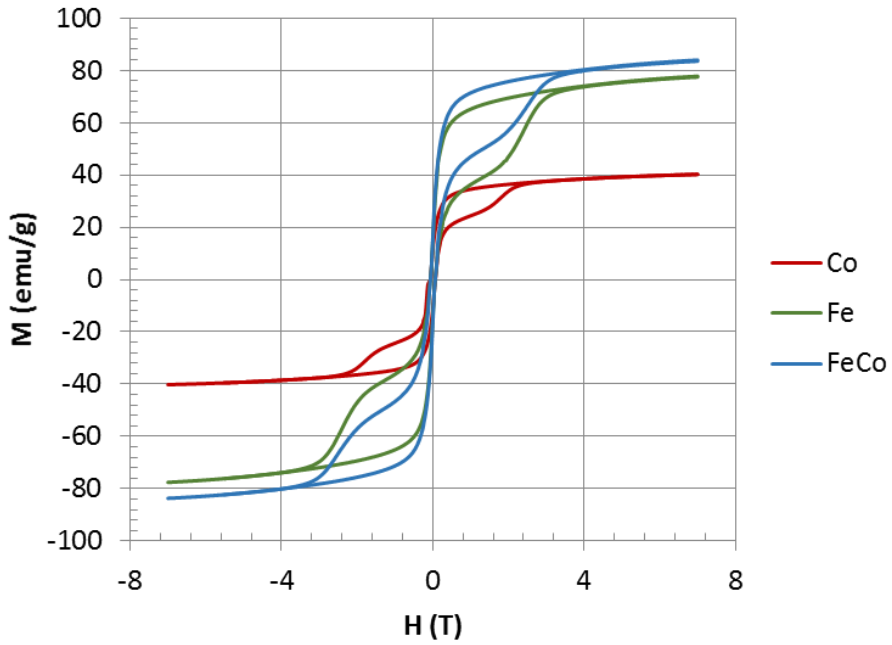

Figure 3.60 Ball-milled mixtures of annealed, spark-eroded MnBi powder with Fe, Co, and FeCo. Fe and FeCo appear to increase M_S, while Co decreases M_S.

In Figure 3.60, the M-H loops of annealed MnBi from spark erosion is mixed with other soft phases by ball-milling. Co reduces the magnetization, likely due to anti-ferromagnetic coupling. Fe and FeCo form satisfactory mixtures, albeit with lower-than-expected M_S due to aforementioned milling effects.

When the mixtures are compacted by RPS in order to consolidate and form better interfacial contact, some adverse effects are observed. In Figures 3.61, 3.62, and 3.63, a comparison of the Co, Fe, and FeCo powder mixtures and their compacts are compared, respectively. When the cobalt mixture is consolidated, a total loss of hysteresis occurs, and M_S is further reduced. The Fe mixture has a similar effect, except that the presence of a two-phase mixture is evident. The FeCo mixture shows no changes due to compaction.

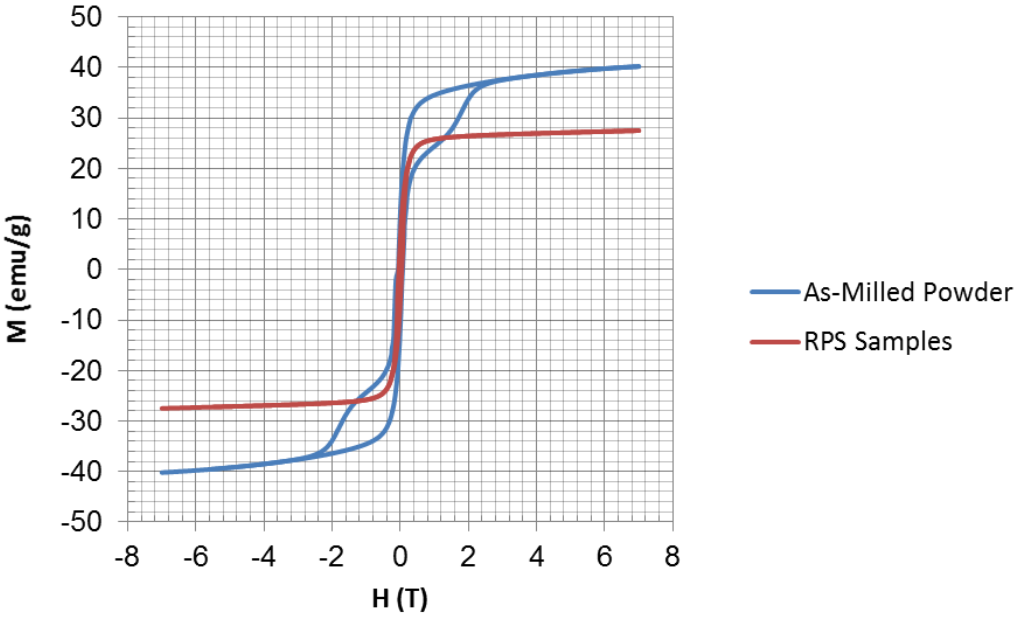

Figure 3.61 Annealed, spark-eroded MnBi powder mixed with 27 wt % Co nanoparticles by ball-milling, and compacted by RPS before and after compaction, showing loss of hysteresis after RPS.

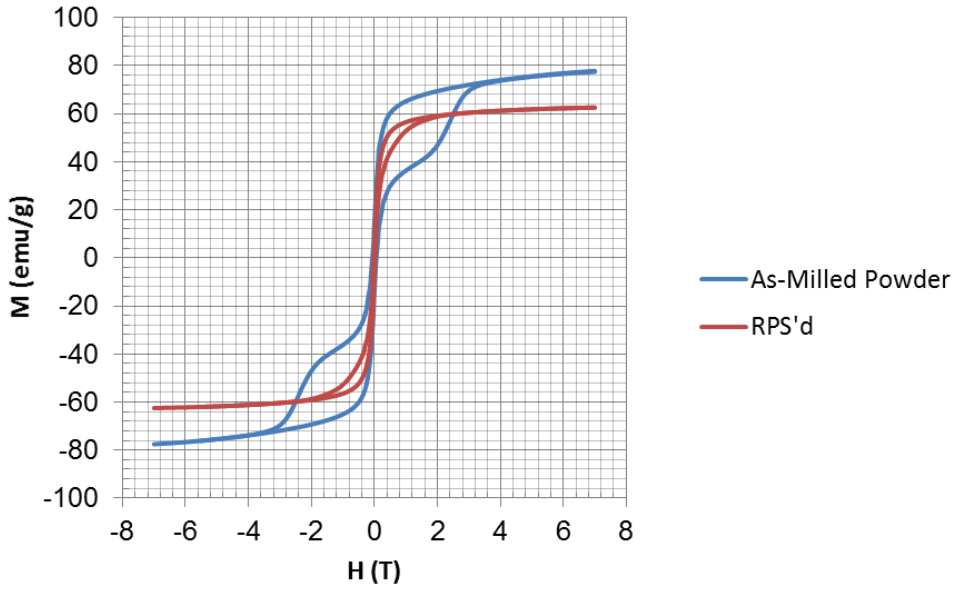

Figure 3.62 Annealed, spark-eroded MnBi powder mixed with 25 wt. % spark-eroded Fe particles by ball-milling and compacted by RPS before and after compaction, showing some loss of hysteresis after RPS.

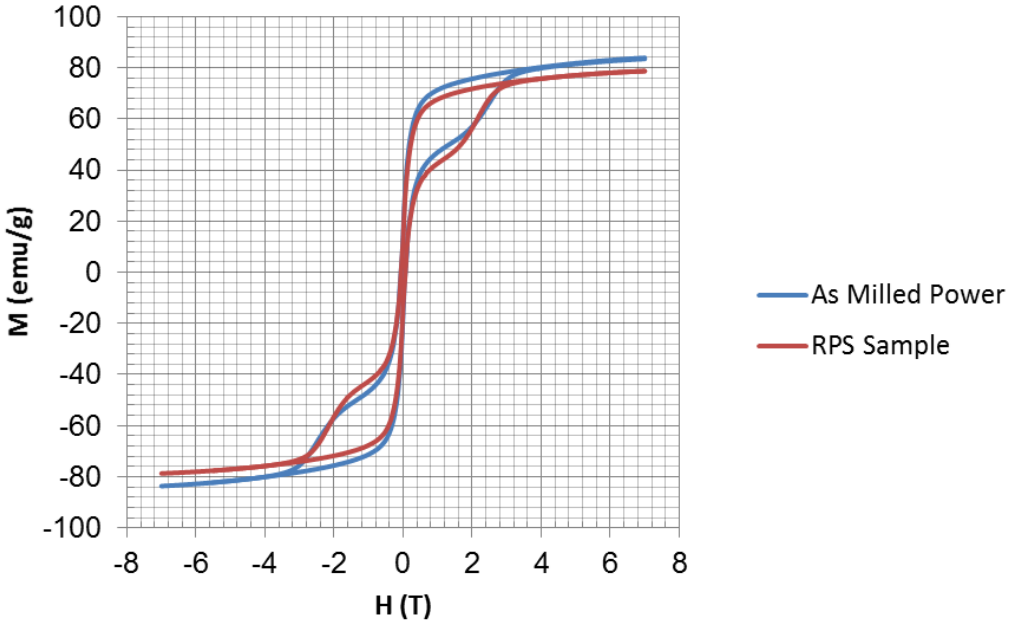

Figure 3.63 Annealed, spark-eroded MnBi powder mixed with 26 wt. % spark-eroded FeCo particles by ball-milling and compacted by RPS before and after compaction, showing no loss of hysteresis after RPS.

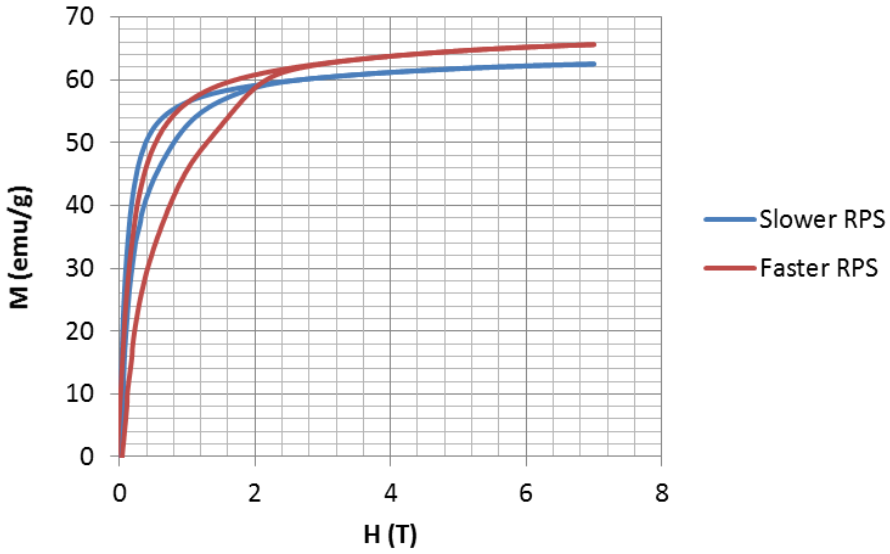

Figure 3.64 Annealed, spark-eroded MnBi powder mixed with 25 wt. % spark-eroded Fe particles by ball-milling and compacted by RPS at different heating rates. The slower rate appears to have a greater loss of hysteresis.

That the Fe mixture deteriorates after RPS is consistent with a report that Fe substitutes for Mn in MnBi thin films with an antiferromagnetic interaction[24]. The M-H loop in Figure 3.64 shows that a "faster" RPS (faster heating rate and shorter hold time) produces a compact with slightly higher moment and a larger hard component. The properties of the Co mixture after just mixing suggests that the mixing was very intimate, and that it promoted a strong magnetization decrease, possibly due to an antiferromagnetic exchange interaction. The FeCo mixture was unaffected by RPS, indicating a remarkable absence of any exchange interactions.

An EDX elemental mapping and SEM of the polished FeCo mixture compact confirms the homogeneity of the phases (Figure 3.65). By comparison, Figure 3.66 shows EDX mapping of a lightly SPEX milled mixture showing large aggregates of MnBi and a large particle of FeCo not well-integrated. The ball-milled mixture shows homogeneity and the breaking of any clusters or particles. This is evidently inadequate to produce an exchange-spring magnet.

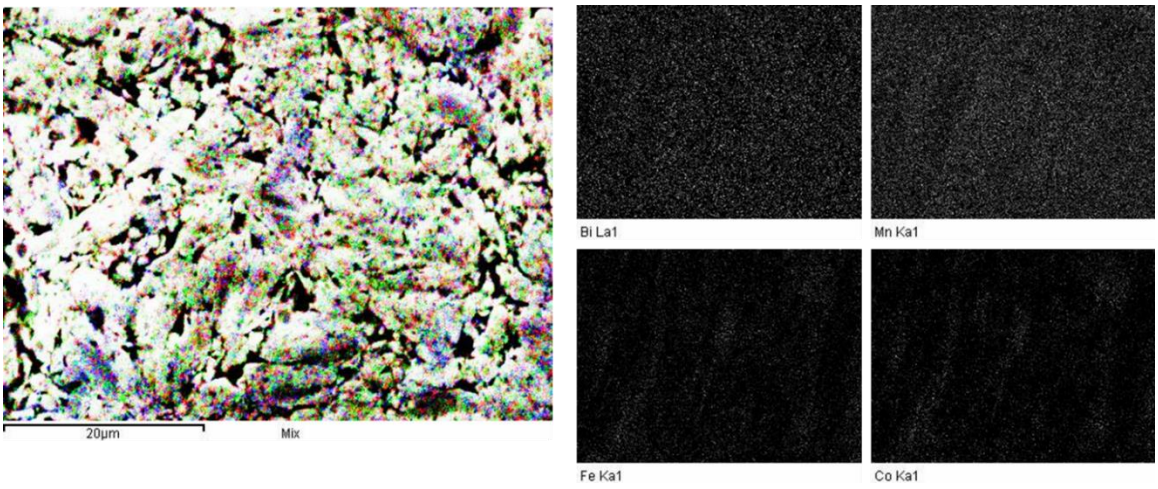

Figure 3.65 EDX elemental mapping of the MnBi-FeCo ball-milled mixture showing relative homogeneity at the micron scale.

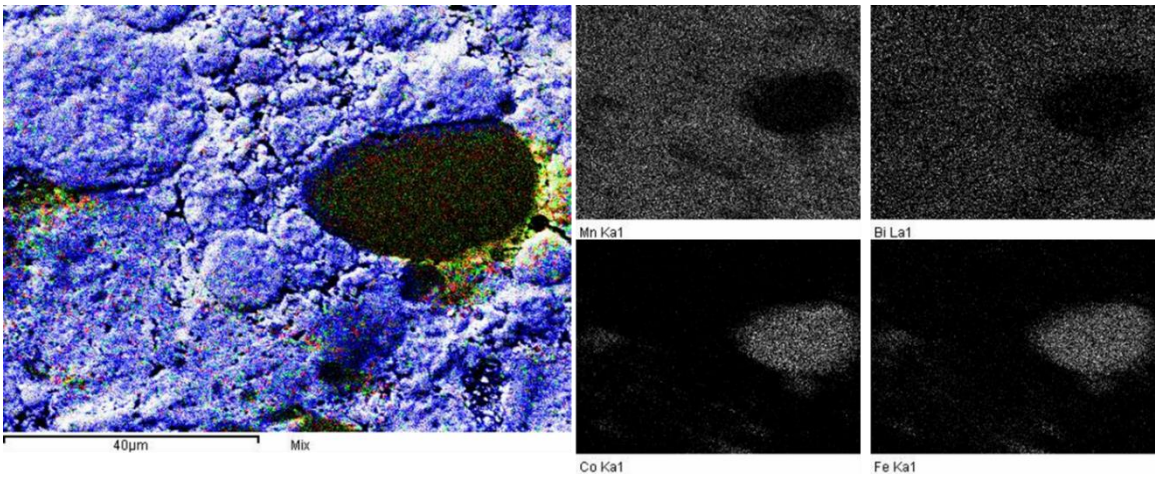

Figure 3.66 EDX elemental mapping of the MnBi-FeCo lightly-milled mixture showing a large particle of FeCo.

The effects of magnetically aligning these mixtures when mixed with as-sparked, amorphous MnBi powder was investigated. The resultant properties of an Fe mixture (10 wt % only) are shown in Figure 3.67. When the powder is compacted and magnetically annealed, the increase in moment is only slight (50 emu/g at 3 T). In contrast to the previous mixture of Fe with annealed powder, the hard phase remains, with evidence of substantial multidomain presence. The properties of the same powder consolidated by RPS, with the same time and temperature profile is compared in Figure 3.68 showing a smoother curve. This two-phase curve appears smooth since the fraction of Fe is small (see Appendix C).

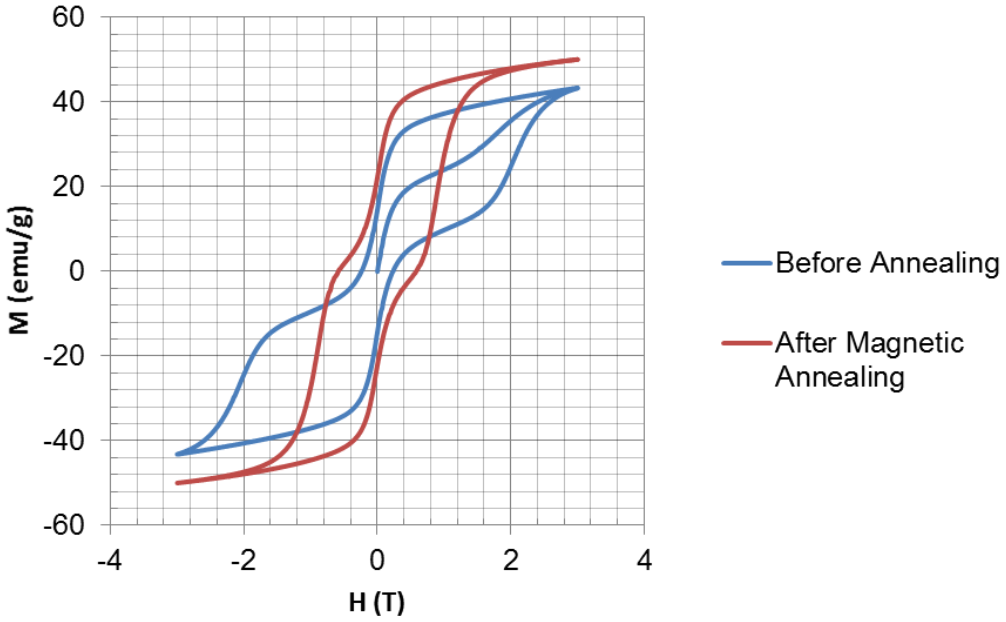

Figure 3.67 Ball-milled mixture of spark-eroded MnBi and Fe before and after annealing in a magnetic field, showing two phases with partial alignment.

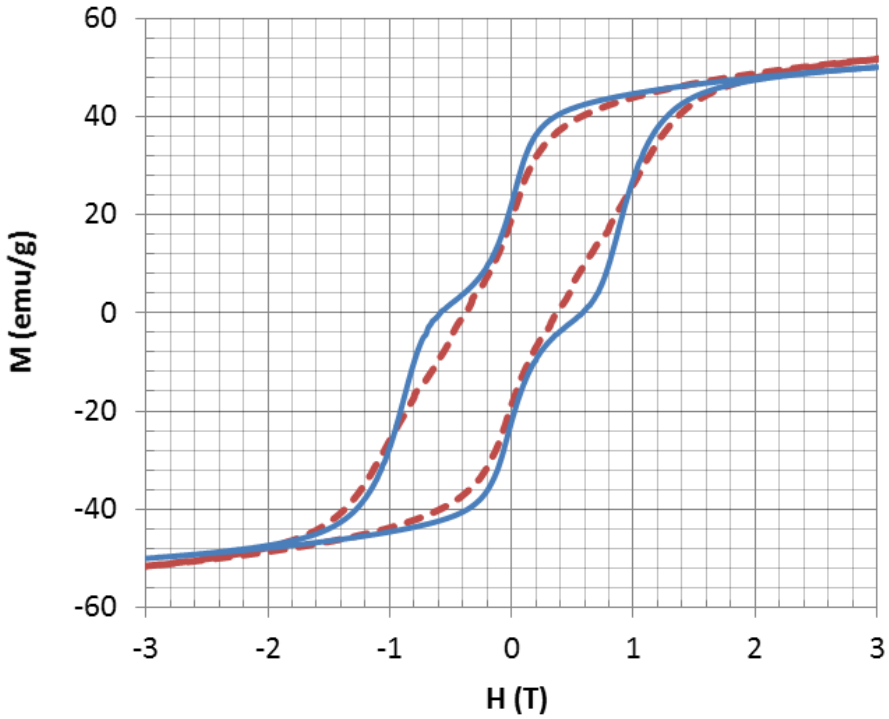

Figure 3.68 Aligned mixture of spark-eroded MnBi and Fe (red dashed) compared to the RPS compact of the same mixture, demonstrating the effects of alignment.

3.3.4.2 Coated MnBi Particles (Co)

$CoCl_2$ may be used to coat MnBi with Co. When bulk MnBi was mixed for several hours in a 0.25 M solution of $CoCl_2$ in ethanol, EDX elemental mapping found that cobalt has deposited on the outside of this ingot (Figure 3.69)

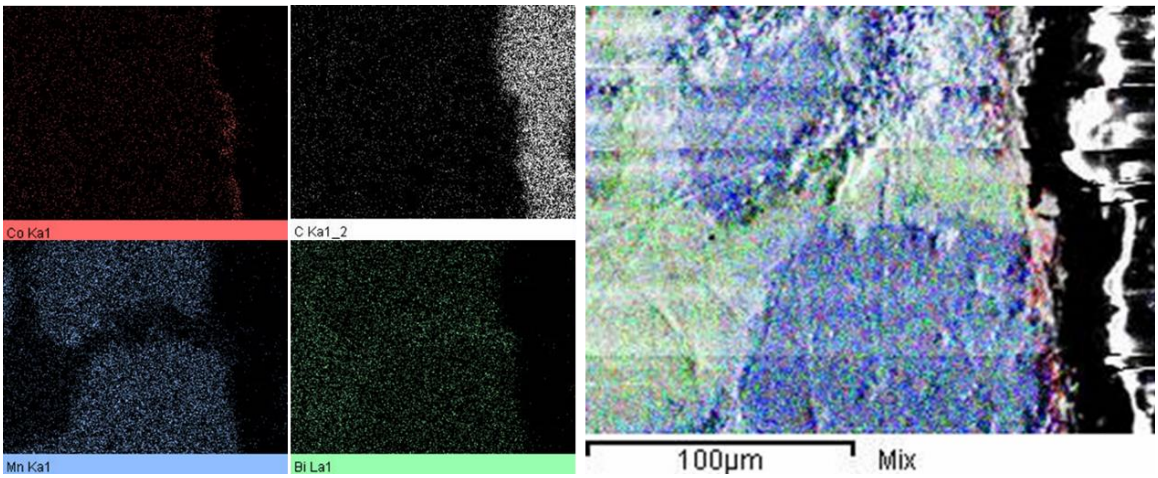

Figure 3.69 EDX elemental mapping of a MnBi bulk ingot coated with Co by stirring in a 0.25 M $CoCl_2$ ethanol solution for several hours.

When spark-eroded MnBi was annealed and milled in the same solution, M_S decreased from 45 to 22 emu/g. The resulting M-H loop was compared to the starting powder in Figure 3.70. When the powders are measured at 800 K, the soft loop was unchanged; MnBi should have decomposed. EDX of these particles detected only cobalt and bismuth (no manganese), and the atomic percent of cobalt is about a 1:1 ratio with that of bismuth. This implies that the salt solution decomposed the MnBi, replacing the manganese with cobalt. The manganese is likely to have been washed away in the ethanol solution upon drying of the powders. The resultant Co-Bi particles have a slightly lower

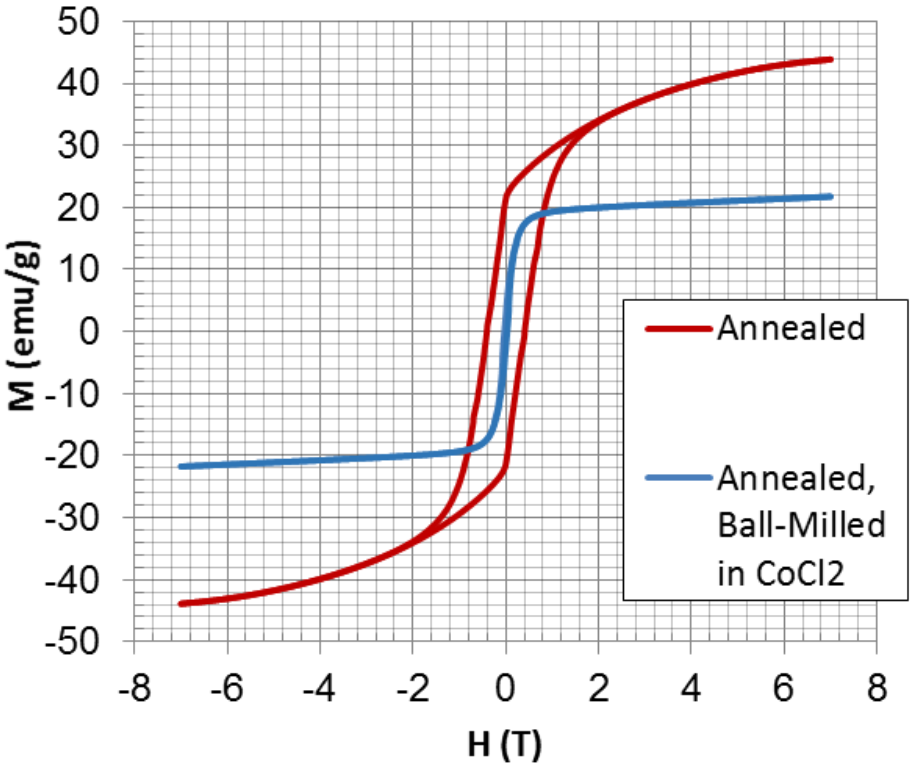

Figure 3.70 Annealed spark-eroded MnBi powder before and after ball-milling in a $CoCl_2$ ethanol solution, showing a total loss in hysteresis.

moment than that of MnBi due to the major weight fraction of bismuth, which contributes no magnetic moment. This work is promising since the composition may be biased to be rich in sacrificial Mn.

When the annealed MnBi powder is mixed with the $CoCl_2$ solution by ball-milling in glass vials, some tunability is achieved, and the resultant demagnetization curves are shown in Figure 3.71. What is important is the number of Co ions per mass of MnBi. It was thus calculated that 10 mL of the 0.1 M solution will create a 2 nm coating of Co around 1 gram of spark-eroded MnBi. For comparison, 0.05 M and 0.2 M was used. As expected, H_C increases as the molarity of $CoCl_2$ decreases. However, in all

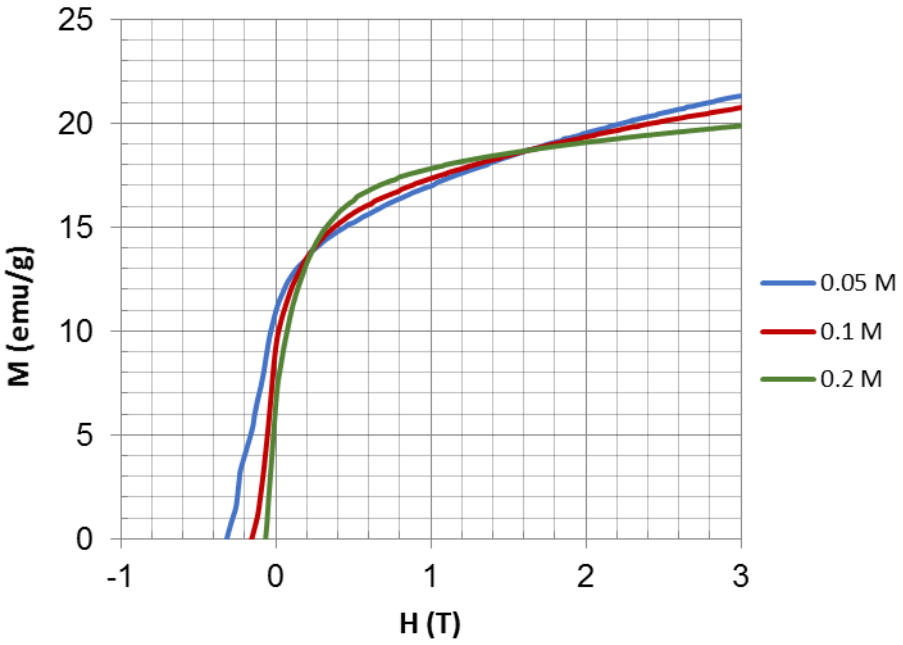

Figure 3.71 Annealed spark-eroded MnBi powder ball-milled with $CoCl_2$ ethanol solutions of various molarities in glass vials. Larger molarities decrease both M_r and H_C.

cases, H_C is still very low and the moment is significantly less than without any coating. The moment also decreases with increasing molarity.

In order to minimize the interaction of the soft and hard phase (retain only a coating), annealed MnBi was also mixed by ultrasonication. This will allow clusters to remain, but a smaller portion of MnBi will be affected. The demagnetization curves are shown in Figure 3.72 and follow the same trend of higher molarity reducing both H_C and M_{3T}. These trends are plotted in Figure 3.73. The decrease of the M_R/M_{3T} ratio with increase molarity shown in Figure 3.74 suggest an increase in soft phase.

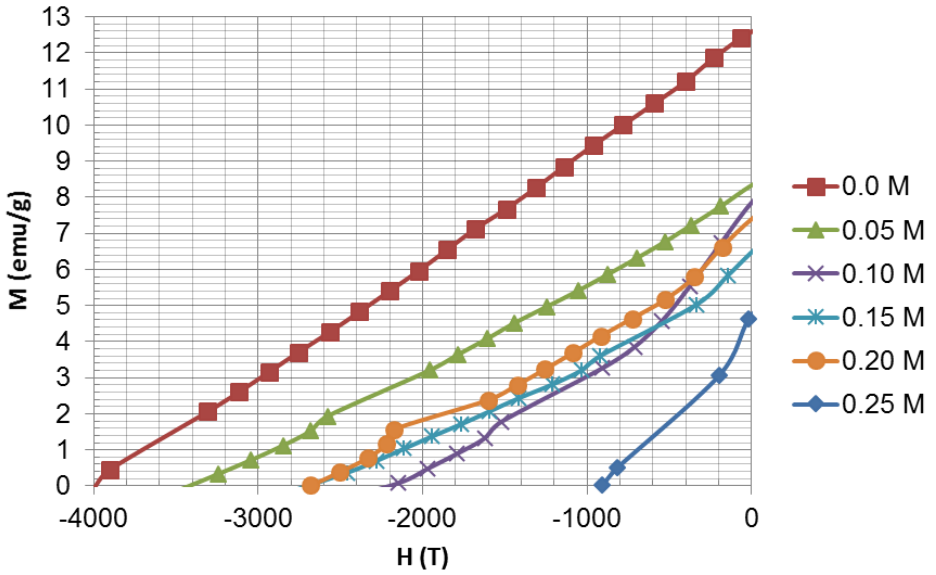

Figure 3.72 Demagnetization curves for annealed spark-eroded MnBi powder ultrasonicated in $CoCl_2$ solutions of various molarities. Higher molarities have greater loss of hysteresis.

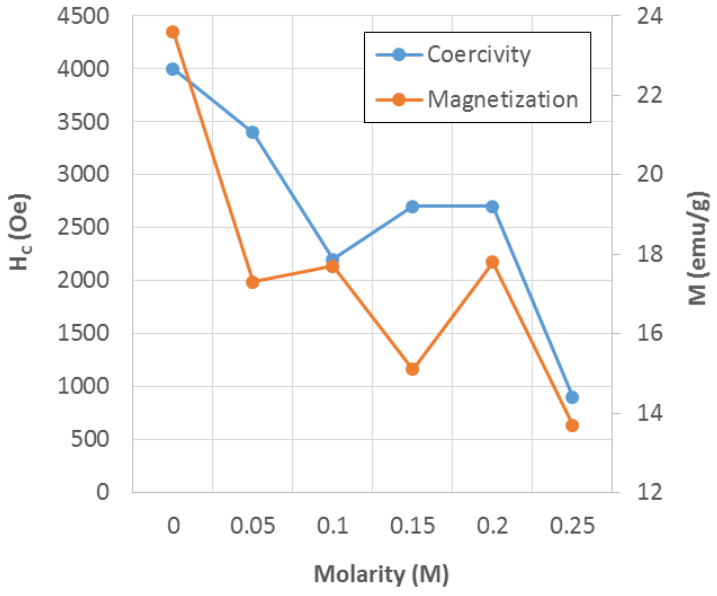

Figure 3.73 Trend of coercivity and magnetization in 3 T for powders ultrasonicated in $CoCl_2$ solution of various molarities. Both properties are decreased with increasing molarity.

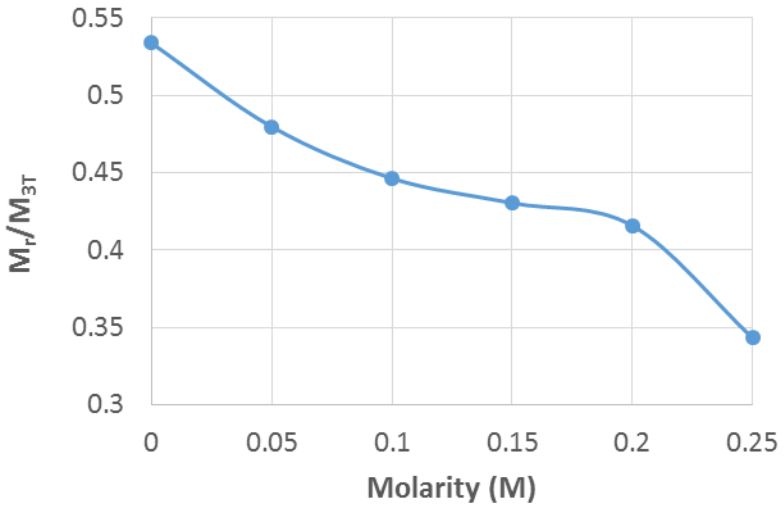

Figure 3.74 M_r/M_{3T} for powders ultrasonicated in $CoCl_2$ solution of various molarities. The decreasing trend is suggests that more soft phase is added at higher molarities.

Finally, in order to minimize any localized heating and maximize uniformity, as-sparked powder was mixed with the $CoCl_2$ at a steady rate by gentle stirring. The moment is very low, but the coercivity is high. As seen in Figure 3.75, an increase in molarity (with all other quantities fixed) produces a higher moment with negligible effect on H_C. In addition, as the molarity is increased, a kink is formed, but M_r still increases. These are the ideal trends for an exchange-spring magnet, and it is possible that some exchange-spring behavior exists, but the moment is too poor for this to be considered a success. This "minimal energy" approach is perhaps what is necessary to keep the Co from interacting with the MnBi while producing a uniform coating.

EDX analysis on the powder (Figure 3.76) confirms that the Bi portion barely changes, but that Co replaces Mn. By comparing to M-H loops in Figure 3.75, we see that the M_{3T} is tripled from the 0.05 M batch to the 0.2 M batch. This correlates to the

increase of Co in the EDX analysis suggesting that the increased moment is due to Co and that the small portion of MnBi is relatively constant. The soft Co phase increases the moment of the MnBi particles without reducing H_C.

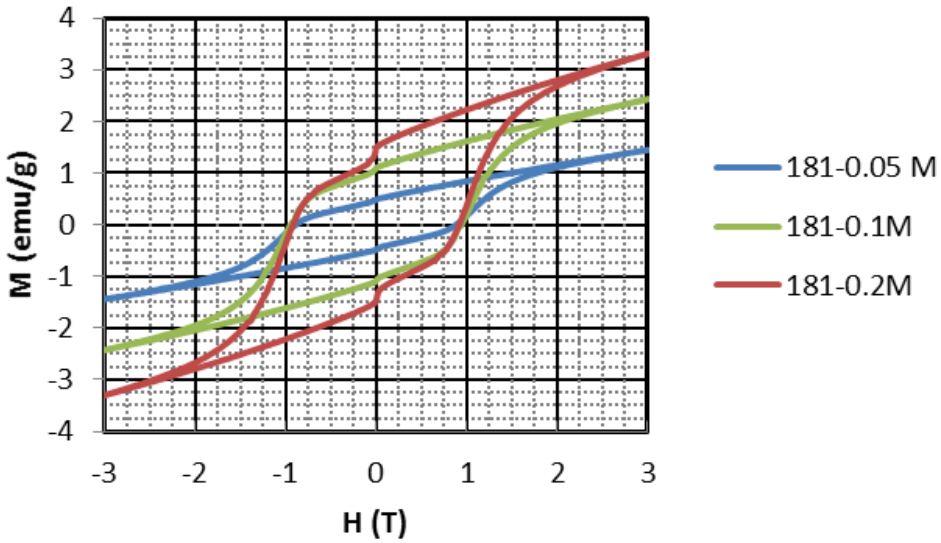

Figure 3.75 M-H loops for spark-eroded MnBi powders stirred in ethanol while $CoCl_2$ solutions of various molarities is slowly introduced by dripping.

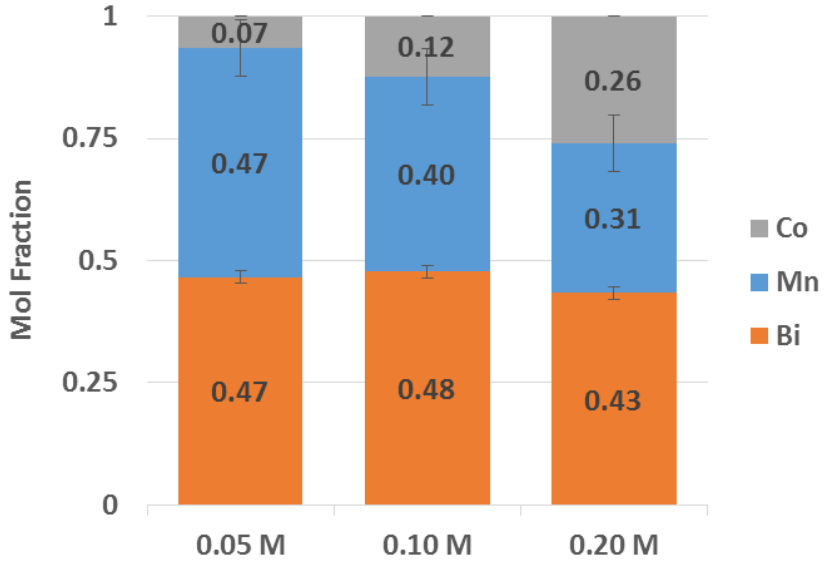

Figure 3.76 EDX analysis on the MnBi particles mixed with the $CoCl_2$ solution suggests that the Co replaces Mn.

3.4 Conclusions

High-purity bulk LTP-MnBi ingots have been achieved by chill-casting and subsequent annealing. These polycrystalline ingots, consisting of large multi-domain grains, exhibit low H_C due to the nucleation of reverse domains. Because such ingots are difficult to produce, another method for improving the magnetization of arc-melted ingots was developed. By annealing the ingots in a vacuum with a mesh fixture, molten bismuth is extracted from the ingot producing a porous ingot with M_S comparable to the chill-cast ingots.

With these bulk ingots, high-purity LTP-MnBi particles have been produced by spark erosion, followed by subsequent annealing. The spark erosion yield consists of a major portion of 20-30 nm particles formed into clusters and aggregates. A large fraction of the as-sparked powders is amorphous and crystallizes rapidly. Once crystallized, the M_S is 69 emu/g, over 90 % of bulk value. These particles can be lightly milled to increase H_C without decreasing M_S in order to yield $(BH)_{MAX}$ of 3.0 MGOe at room temperature in a randomly-oriented sample.

It was found that with further milling of these powders, room-temperature H_C of 2 T can be achieved. However, such milling reduces M_S. Annealing these milled powders does not increase M_S, but decreases H_C due to particle necking. The optimal milling intensity for high $(BH)_{MAX}$ is thus a balance of increasing H_C by breaking particle clusters and retaining M_S by avoiding phase segregation caused by localized heating.

Partially-aligned compacts of spark-eroded MnBi can be made by cold-pressing and annealing in a magnetic field of 3 T. When the amorphous component of spark-eroded MnBi is crystallized in a magnetic field, the crystals grow with their easy c-axis aligned along the direction of the applied field. The crystallographic orientation of the resulting compact was confirmed by x-ray diffraction studies on the aligned sample. Spark-eroded powders that have been milled can also be aligned, which produces a larger coercive force, albeit with lower M_S.

Finally, spark-eroded particles were mixed with Fe, Co, and FeCo soft phases by ultrasonication, ball-milling, and chemical solutions. When ball-milled and compacted by RPS, the Co mixtures exhibit the most reduced magnetic properties. Mixtures of MnBi and Fe undergo similar deterioration only when heated. The magnetic properties of the FeCo mixture do not deteriorate, but remain two-phase. Presumably, the reasons for poor properties (e.g. oxidation, contamination, surface effects, and phase segregation) prevent the Fe or Co from negatively interacting with the MnBi. The magnetization of spark-eroded particles, in which M_S was only a few emu/g, was successfully increased by the addition of Co without decreasing H_C.

3.5 Acknowledgements

We wish to acknowledge useful discussions with Prof. Yang-Ki Hong, Dr. Jun Cui, Prof. Eric Fullerton, and Dr. Frederick Spada. This work was funded by the ARPA-E REACT Project No. 0472-1554 and Grant #121770.

This chapter, in part, is a reprint of the material as it appears in Journal of Applied Physics, Volume 115, 2014, and IEEE Transactions on Magnetics, Volume 49, 2013, Phi-Khanh Nguyen, Sungho Jin, and Ami E. Berkowitz. The dissertation author was the primary investigator and author of these papers

3.6 References

[1] B. D. Cullity and C. D. Graham, “Introduction to Magnetic Materials”, John Wiley & Sons, Inc, Hoboken, NJ (2009).

[2] K, J. Strnat, “Modern Permanent Magnets for Applications in Electro-Technology”, Proceedings of the IEEE, Vol. 79, No. 6, 923 (1990).

[3] O. Gutfleisch, M. A. Willard, E. Bruck, C. H. Chen, S. G. Sankar, and J. P. Liu, “Magnetic materials and devices for the 21st century: stronger, lighter, and more energy efficient”, Adv. Mater. **23**, 821-842 (2011).

[4] M. S. Walmer, C. H. Chen , M. H. Walmer, “A New Class of Permanent Magnetic Materials For High Temperature Applications in TWT”, *IEEE Trans. Magn.* **2000**, *36* , 3376 .

[5] S. D. Bader, “Collquium: Opportunities in nanomagnetism”, Rev. Mod. Phys., Vol. 78 (2006)

[6] E. F. Kneller and R. Hawig, “The Exchange-Spring Magnet: A New Material Principle for Permanent Magnets”, IEEE Trans. Mag., Vol. 27, No. 4, (1991).

[7] R. Skomski and J. M. D. Coey, “Giant energy product in nanostructured two-phase magnets”, Phys. Reg. B, Vol. 48, No. 21 (1993).

[8] T. Chen and W. Stutius, "The Phase Transformation and Physical Properties of the MnBi and $Mn_{1.08}Bi$ Compounds", IEEE Mag. Trans. MAG-10, 581, (1974).

[9] E. Adams, W. M Hubbard, and A. M Syeles, "A New Permanent Magnet from Powdered Manganese Bismuthide", J. Appl. Phys., Vol. 23, No. 11, pp. 1207-1211. (1952).

[10] W. G. Moffatt, “The Handbook of Binary Phase Diagrams”, Vol. 4, General Electric Company, Corporate Research and Development, Technology Marketing Operation, Genium, (1981).

[11] A. F. Andresen, "The Magnetic and Crystallographic Properties of MnBi Studied by Neutron Diffraction", Acta. Chem. Scan., Vol. 21, pp 1543-1554. (1967).

[12] H. Yoshida, T. Shima, T. Takahashi, and H. Fujimori, "Preparation of Highly Pure MnBi Intermetallic Compounds by Arc-Melting", Mater. Trans, JIM, Vol. 40, No. 5, pp. 455-458. (1999).

[13] X. Guo, X. Chen, Z. Altounian, and J. O. Strom-Olsen, “Magnetic properties of MnBi prepared by rapid solidification”, Phys. Rev. B, **46**, 22 14 578 (1992).

[14] X. Guo, A. Zaluska, Z. Altounian, and J. O. Strom-Olsen, "The Formation of Single-Phase Equiatomic MnBi by Rapid Solidification", J. Mater. Res., Vol.5, No. 11 (1990).

[15] S. Saha, R. T. Obermyer, B. J. Zande, V. K. Chandhok, S. Simizu, and S. G. Sankar, “Magnetic properties of the low-temperature phase of MnBi”, J. Appl. Phys. 91 8525 (2002).

[16] N. V. Rama Rao, A. M. Gabay, and G. C. Hadjipanayis, “Anisotropic fully dense MnBi permanent magnet with high energy product and high coercivity at elecvated temperatures”, J. Phys. D: Appl. Phys. **46** (2013).

[17] J. Cui, J. Choi, E. Polikarpov, M. E. Bowden, W. Xie, G. Li, Z. Nie, N. Zarkevich, M. J. Kramer, and D. Johnson, “Effect of composition and heat treatment on MnBi magnetic materials”, Acta. Mater., **79**, 374-381 (2014).

[18] B. W. Roberts and C. P. Bean, "Large Magnetic Kerr Rotation in BiMn Alloy", Phys. Rev. Vol. 96, No. 6, pp. 1494-1496. (1954).

[19] M. Kishimoto and K. Wakai, "Single-Domain Properties in MnBi Particles", Japan. J. Appl. Phys., Vol. 15, No. 9, pp 1843-1844. (1976).

[20] F. Yin, N. Gu, T. Shigematsu, and N. Nakanishi, “Sintering Formation of Low Temperature Phase MnBi and Its Disordering in Mechanical Milling”, J. Mater. Sci. Technol. 12 335 (1996)

[21] X. Guo, Z. Zaluska, and J. O. Strom-Olsen, “Electron microscope studies of phase transformations in rapidly solidified MnBi alloys”, Mater. Sci. Eng. A, Vol. 133, 509 (1991).

[22] P.-K. Nguyen, K. H. Lee, J. Moon, S. I. Kim, K. A. Ahn, L. H. Chen, S. M Lee, R. K. Chen, S. Jin, and A. E. Berkowitz, “Spark erosion: a high production rate method for producing $Bi_{0.5}Sb_{1.5}Te_3$ nanoparticles with enhanced thermoelectric performance”, Nanotechnology **23** 415604-415711 (2012).

[23] J. B. Yang, W. B. Yelon, W. J. James, Q. Cai, S. Roy, and N. Ali, “Structural and magnetic properties of the MnBi low temperature phase”, J. Appl. Phys., Vol. 91, No. 10, (2002).

[24] P. Kharel, X. Z. Li, V. R. Shah, N. Al-Aqtash, K. Tarawneh, R. F. Sabirianov, R. Skomski, and D. J. Sellmer, “Structural, magnetic, and electron transport properties of MnBi:Fe thin films”, J. Appl. Phys., Vol. 111, 07E326 (2012).

APPENDIX A: SPARK EROSION

A.1 Background

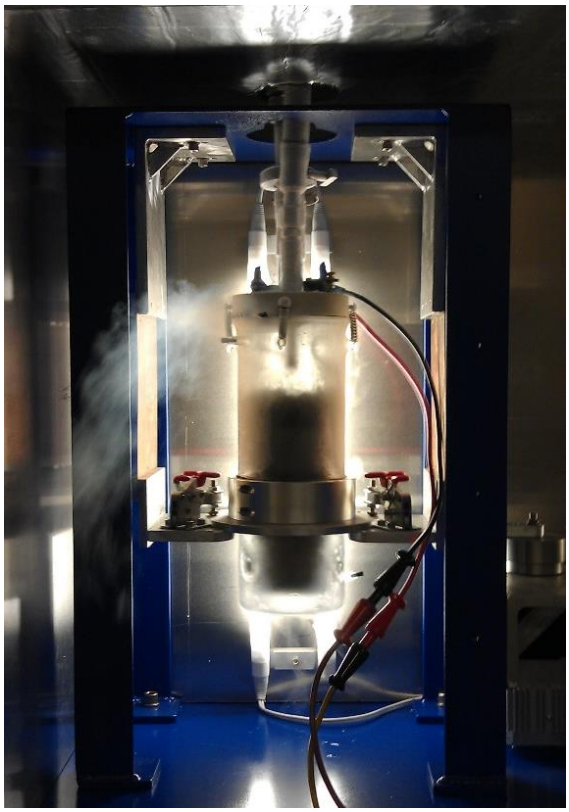

Figure A.1 Photograph of the shaker-pot version of spark erosion during a run.

Spark erosion is a technique developed by Ami E. Berkowitz, committee chair of this thesis, and John L. Walter at General Electric Company in 1980.[1] The technique utilizes the energy of electrostatic spark discharges to expel molten particles from an electrode or connected charge piece. In spark erosion, a charged capacitor is attached to electrodes of any conductive starting material. When the electric field across these two

electrodes, separated by a sufficiently small gap, is larger than the dielectric breakdown field of the liquid in which they are immersed, the capacitor discharges, producing a spark (micro-plasma) between the pieces involved. This micro-plasma, consisting of electrons and positive ions, is very hot, of the order of 10,000 K.[1] The kinetic energies of the faster electrons and slower ions are deposited on localized regions where the spark was initiated, superheating them to boiling. When the spark collapses, vaporized alloy and molten droplets are violently ejected from the boiling regions and propelled through the plasma region into the dielectric liquid where they are very rapidly quenched.

Spark erosion is very versatile – any material that is conductive can be spark-eroded. The process typically produces particles that are spherical in nature due to the generation of molten droplets. Hollow particles have also been produced.[2] Because of a fast quench rate, spark erosion can produce amorphous powders.[3] The ability to create fine particles also makes it an attractive method for producing ferrofluids.[4]

The majority of spark-eroded particles are typically of micron size. By varying electric power settings, Carrey *et al* has discussed the tunability of the maximum spark-eroded particle size, which is determined by how much material can be melted with the energy of one spark.[5] The actual dynamics are much more complicated because less energy typically goes into particle formation. In the work presented in this dissertation, high energy sparks focus on vaporizing a local portion of material rather than melting a large portion. This vaporization produces a majority fraction of nanoparticles that are useful for thermoelectric and permanent magnets.

A primary advantage of spark erosion is that it is a rapid-quenching technique that requires no crucible. Contamination is thus restricted to only contact with the dielectric

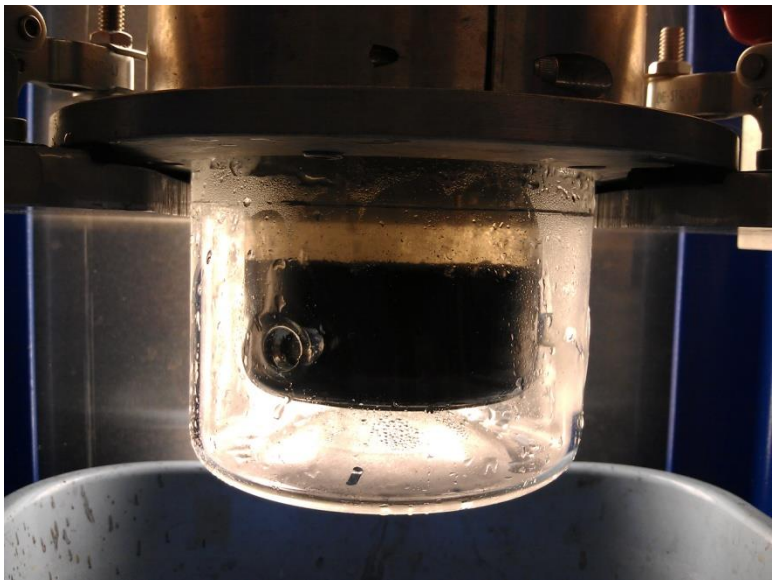

Figure A.2 Spark-eroded MnBi particle yield after 1 hour in a 4 inch ID glass pot. Rates of as high as 360 grams per hour have been achieved.

medium. The dielectric can be selected to be inert (e.g. liquid argon) so that it does not interact with the sparking material. Alternatively, liquid nitrogen, dodecane, ethanol, water, and carbon tetra-chloride have been suitable dielectrics for various materials. Since the entire process can be performed in a hermetically sealed vessel, oxidation and moisture can be minimized.

There are several configurations for utilizing spark erosion for particle production.[5] The *shaker-pot* version is the method of choice because of the ability to attain large yields while minimizing contamination and/or oxidation. Large yields are desirable for scalability and economic feasibility. In this configuration, power is only drawn to re-charge a capacitor that has discharged to form the powder-producing spark. The process is thus very energy-efficient, typically operating at only a few hundred watts.[6]

A.2 Setup and Preparation

The construction of the shaker-pot apparatus can be seen in Figure A.3. Here, a 10 cm diameter spark erosion cell is placed within a double-walled, vacuum-jacketed glass container that holds the dielectric liquid. Alternatively, cooling water can be flown

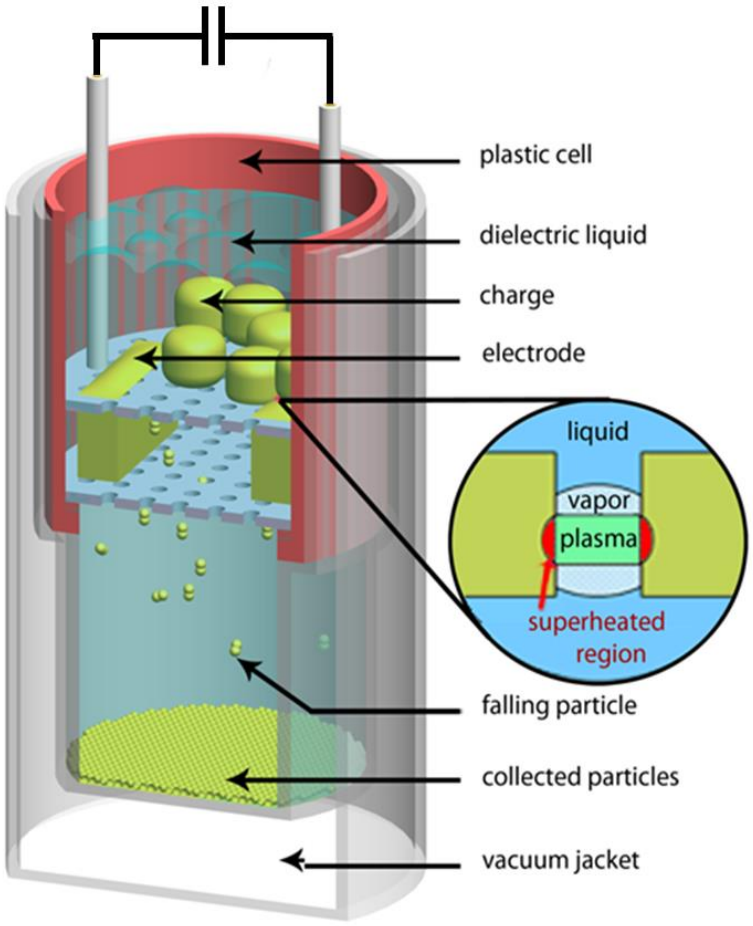

Figure A.3 Spark erosion shaker-pot schematic.

through this jacket to prevent heating when room-temperature dielectrics are used. Two electrodes of the alloy of interest are mounted in the cell and connected to the power

source. ‘Charge’ pieces of the same alloy, irregular shapes roughly 2 cm in size, are placed atop the perforated Delrin™ support, making contact with the electrodes.

The mounting of electrodes is sometimes a non-trivial process. Figure A.4 shows a schematic of how electrodes are typically mounted within the spark erosion cell. Brass rods are hard-soldered into T-junctions for fixing the electrode. The rod acts as the electrical connector and also to fix the electrode in place relative to the cell. The brass rod is typically #8 threaded (ANSI/ASME), and thus a hole of the same size should be machined into the electrode for mounting, as seen in the photograph next to the schematic. It is often too costly to machine this hole, or the shape of the electrode does not permit this configuration. For some metal alloys, electrical connection can be achieved by simply welding or soldering, and then a separate fixture holds the electrodes. An attractive alternative is to clamp the electrode by using aluminium sheet metal (also

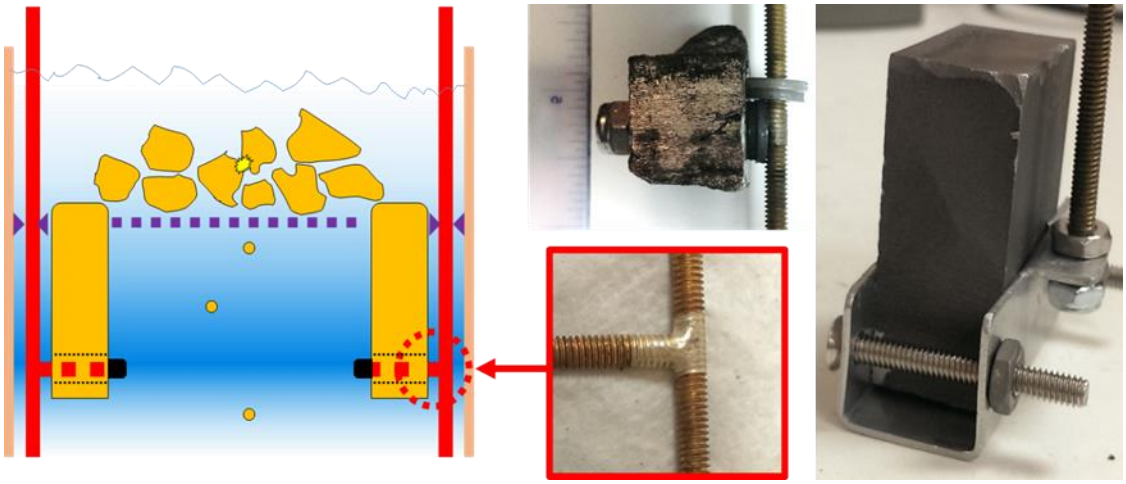

Figure A.4 Schematic for mounting of spark erosion electrodes showing threaded brass rods, alternative aluminum clamp, and charge placement.

displayed in Figure A.4)

We have found that irregularly shaped pieces with a multiplicity of corners and edges act as the best charge pieces. However, as with the electrodes, the shape of the charge is often limited by the economic practicality of cutting bulk ingots into optimal shapes and sizes. The photograph in Figure A.5 shows some charge morphologies that have been effective for spark erosion. This includes button ingots that are directly cast, cylindrical rods that have been segmented, crystals that have been cleaved, and large billets that have simply been fractured into pieces of suitable size. A photograph of the final cell consisting of mounted electrodes and charges is shown in Figure A.6.

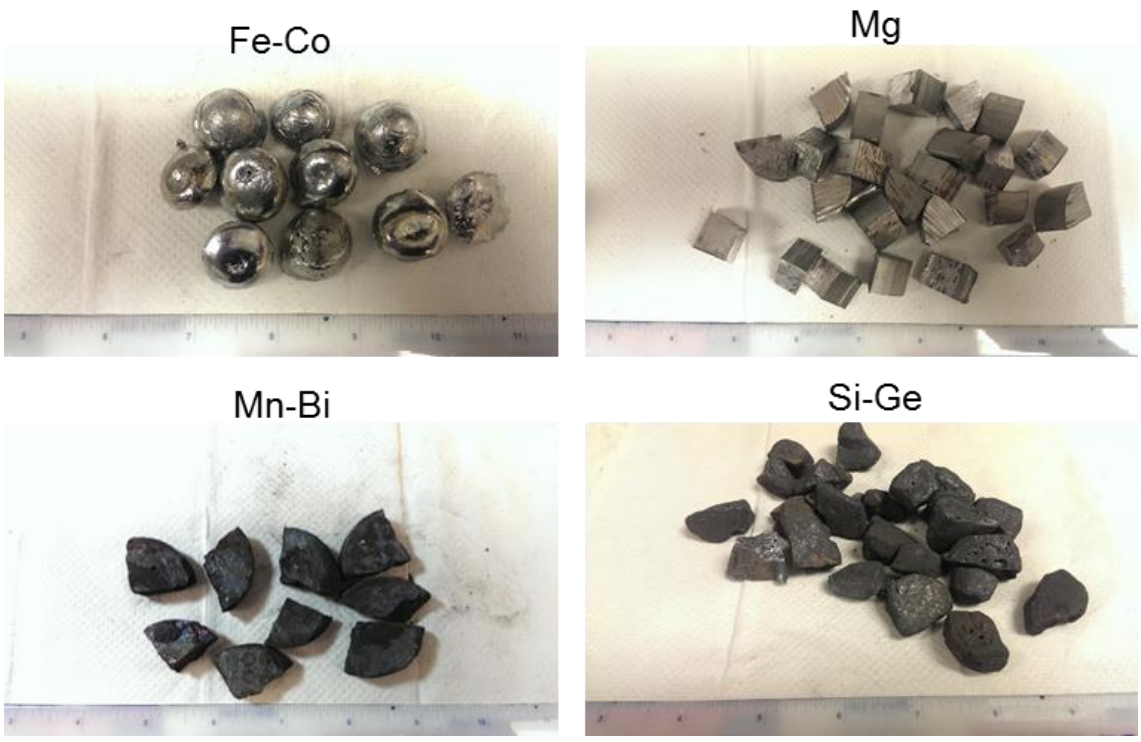

Figure A.5 Photographs of typical spark erosion charges measured with a ruler.

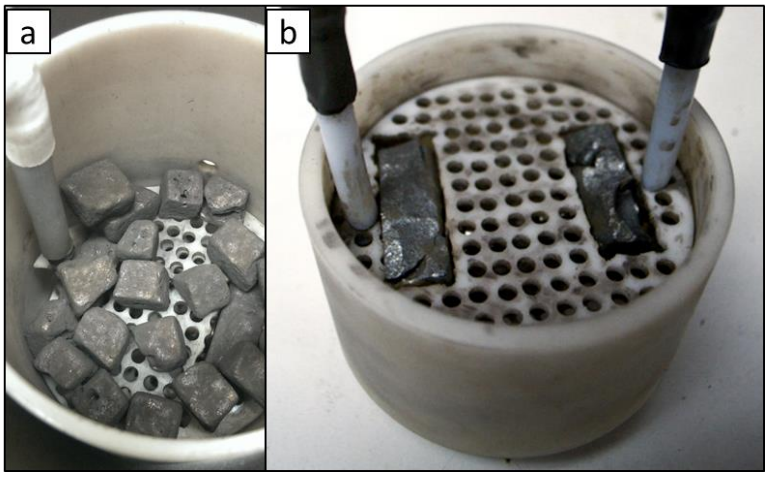

Figure A.6 Spark erosion cell (a) filled with charge, and (b) without charge and with shortened walls to show the exposed electrodes. Brass connectors must be electrically insulated in order to prevent their spark erosion.

A reactor cap creates a hermetic seal while allowing for electrical feedthrough, cryogen input, and exhaust. Additional charge can also be inserted through this exhaust port. While it has been found that the dielectric actually shields the particles from oxidation, the hermeticity of this reactor cap is still important for safety considerations (fine particles are often pyrophoric and can be toxic). The assembled vessel is driven by a variable speed shaking motor and attached with parts that can withstand the vibration at cryogenic temperatures without shattering the glass. A schematic of the completed assembly is shown in Figure A.7. The assembly is shaken so that contacts between the electrodes and charge pieces are made and broken frequently. Thus, electrical contact between the electrodes is made at random, as are the gaps among the charge pieces across which the sparks are generated.

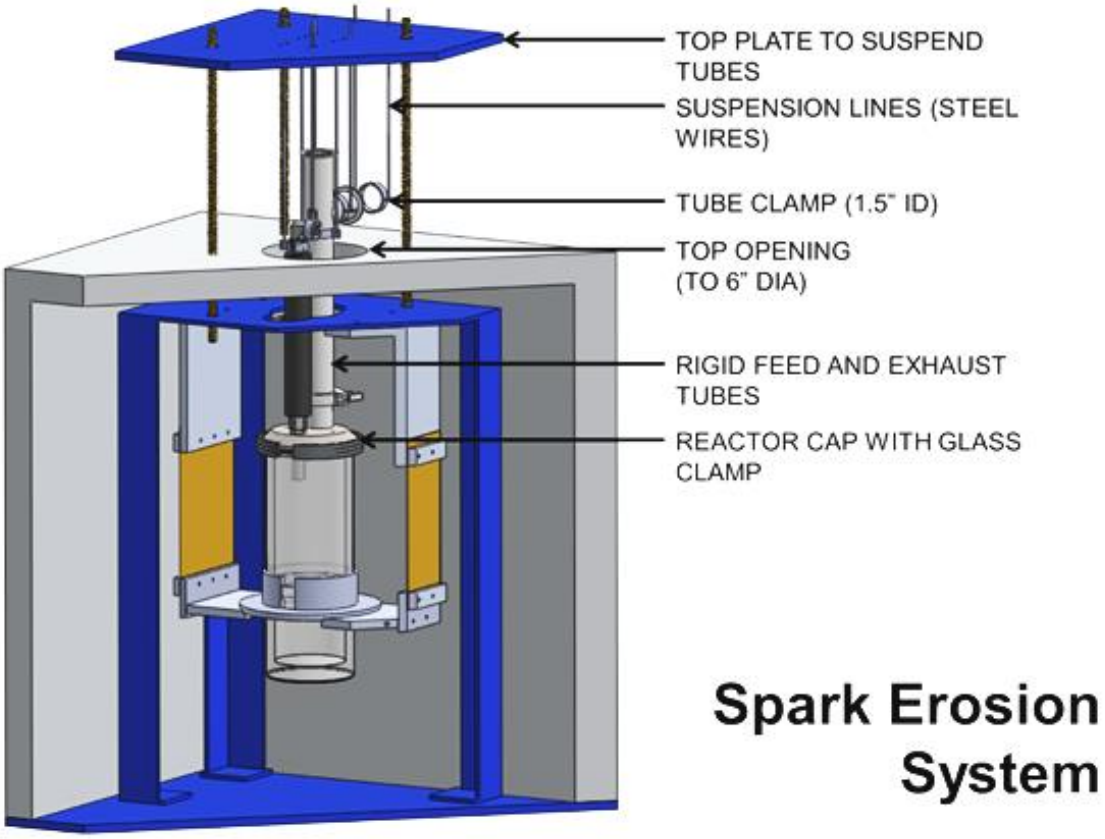

Figure A.7 Spark erosion shaker-pot setup, model view.

A.3 Operation Optimization

The properties of the spark erosion yield are determined by the properties of the spark discharges, which depend on many factors including the amount of charge being discharged from the capacitor, the resistance of the current pathway, the gap distance between the conductive material, and the lifetime of the plasma. The shaker-pot version of spark erosion is stochastic – charge pieces move at random thereby creating a distribution of gap sizes. This forces the capacitors, which are constantly being charged by a power supply, to discharge at random stages in the charging process and for random durations; capacitors often do not discharge completely.

The current waveforms of the spark discharges are observed using a pickup coil connected to an oscilloscope. The typical waveforms of 1000 A peak current and 80 μs time duration can be seen in Figure A.8. The ideal spark erosion run operates

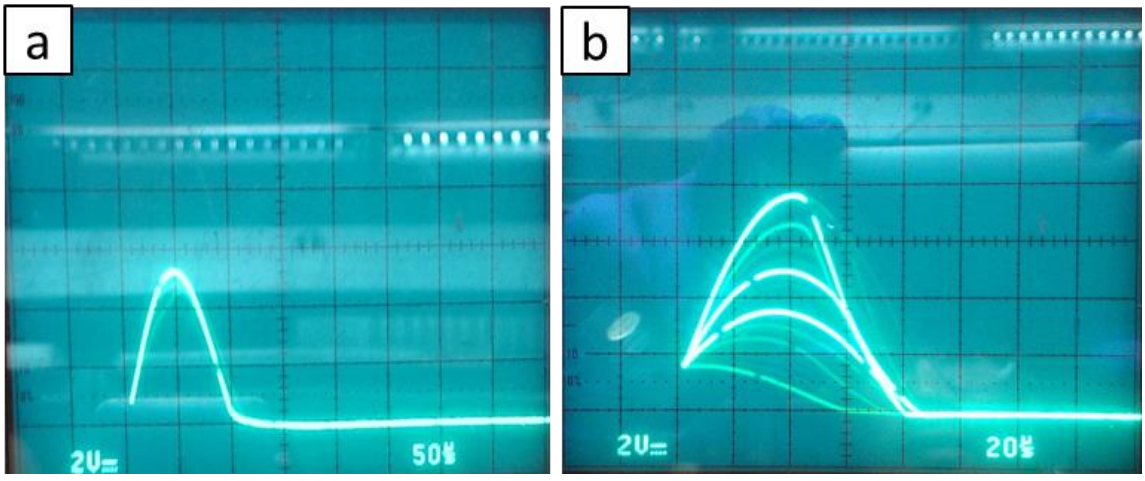

Figure A.8 Spark erosion current waveforms: (a) near ideal and (b) non-ideal distribution of peak amplitudes. Multiple waveforms can be seen by the "persist" function of the oscilloscope.

continuously at the maximum rate in which the all sparks produce uniformly high current waveforms. This is shown in Figure A.8(a), while Figure A.8(b) shows a distribution of peak currents (multiple sparks are seen due to “persistence mode” of trace). Failure to achieve waveform uniformity can lead to a larger distribution of particle sizes and morphologies.

In order to approach the ideal case, the shaking of the vessel and the packing of the charge should be optimized. Since charge packing changes during a run, the shaking requires monitoring and readjustment. Distribution of spark profiles can often be eliminated simply by varying the shaking speed. Excessive quantities of charge may also prevent ideal operation.

During the initial introduction of charge, configurations prone to “jamming” should be avoided. Heavier charge may require an increase in the shaking amplitude, which is changed by adjusting the camshaft length. If no gaps are formed during shaking due to a “jam” or otherwise, the circuit is shorted. This could cause damage to the power supply, cause excessive heat, or weld the charge pieces together. If a “jam” occurs during a run, the power is turned off in order to avoid damage to the electronics.

Aside from spark uniformity, conditions should be adjusted in order to optimize the yield rate. Initially, enough charge is added to form a current pathway without shaking. So if shaken too slowly, sufficient gaps cannot be formed – the number of sparks, the spark rate, will be high and a short may occur. If shaken too quickly, the spark rate will be lower than optimal. Charge size and quantity are most key to spark (and yield) rate. Larger charge pieces typically produce more uniform sparks at the expense of yield rate due to fewer surface contacts.

A.4 Processing and Handling

Spark-eroded metallic particles are often pyrophoric. In these cases, care is taken during collection, handling, and storage. After spark-eroding in a cryogen, the cell containing the charges and electrodes are removed while the vessel is still filled with the cryogen. The cap is replaced with a glass flange that consists of a graded surface and Teflon valve (Figure. 2.9a). The outlet is attached to a bubbler (filled with pump oil) that allows the cryogenic boil-off to escape while preventing air from entering. Once all the cryogen has evaporated, the Teflon valve is closed, and the entire vessel is loaded into an oxygen-gettered argon glove box (< 5 ppm O_2) for particle collection and storage. The powder is sieved (typically at 53 μm) in order to eliminate large chunks fractured off from charge pieces. All further handling of the powder, including annealing, also occurs within the glove box.

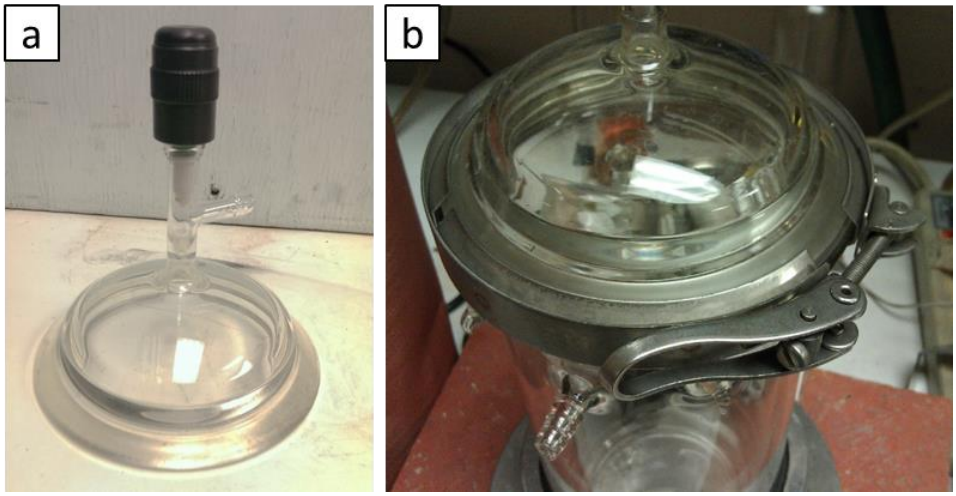

Figure A.9 Glass cap (a) and clamp (b) for safe boil-off of a cryogenic liquid. The cap, with of a Teflon valve, is a standard glass flange.

A.5 Effect of Parameters

The spark erosion parameters that are experimentally varied are the voltage, capacitance, and dielectric liquid. These parameters are the simplest to change, have the most profound effect on the yield rate and morphology, and are typically set before the run occurs, remaining unchanged for the duration of the run (although sometimes the voltage is tweaked in order to achieve a desired peak current). Parameters must be optimized for each system due to variations in material properties. Higher peak currents indicate high-energy sparks. High-energy sparks are apparently more effective in producing nanoparticles in various material systems.

To observe the effect of varying the capacitance, the maximum peak currents and spark time durations were recorded for several spark erosion runs in which aluminum was spark-eroded in various dielectric liquids at various capacitances with an applied voltage of 200 V. The results are shown in Figure A.10. It can be seen that both the spark current and time duration increase with the capacitance. In this case, the choice of dielectric has little effect on these measures (it actually has a large effect on the yield rate). The results are reasonable because the capacitance determines both the amount of charge accumulated and also the rate of discharge.

It is observed is that the peak current changes proportionally with the applied voltage while the spark time duration remains constant. In order to depict this effect, the totality of spark erosion runs performed for optimization of the MnBi work presented in Chapter 3 are plotted in Figure A.11 by the applied voltage and capacitance. The sizes of the circles that represent the run indicates the peak current (left) or pulse duration (right).

It can thus be seen from the current-based plot that the size of the circles increases with both increasing capacitance and voltage, which is consistent with what is seen in Figure A.10 for the aluminum system. However, the sizes of the circles for the time duration plot increase only with increasing capacitance and not with the applied voltage. This is also reasonable because an increase in voltage increases the amount of charge accumulated within the capacitor but not the rate of discharge. The voltage, however, also has a large effect on the rate since a larger applied voltage allows sparking to occur at larger gaps. The voltage can thus be changed to adjust the rate and peak currents.

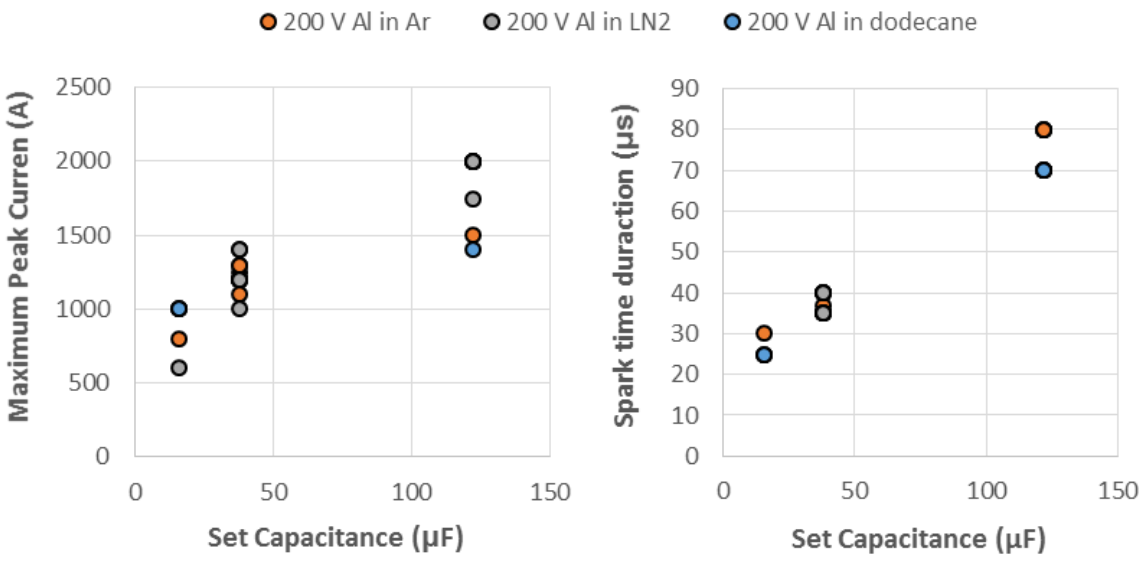

Figure A.10 The effect of the capacitance on the maximum peak current and spark time duration when aluminum is spark-eroded in various dielectric liquids. Both increase with capacitance regardless of dielectric medium.

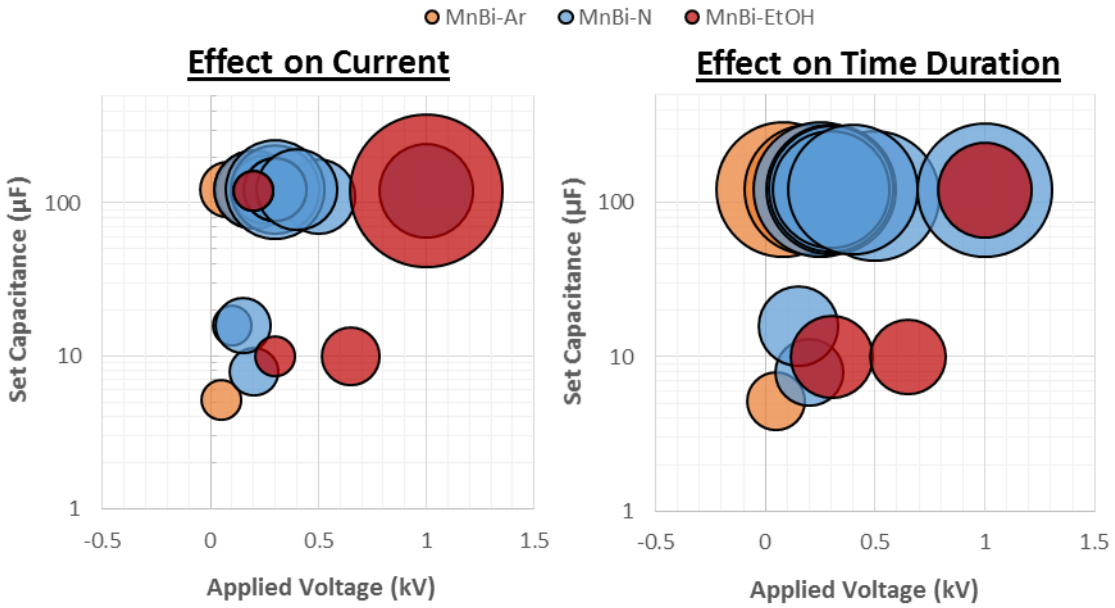

Figure A.11 The spark erosion runs for MnBi as functions of applied voltage and set capacitance with the circle size representing the peak current (left) or spark time duration (right).

Varying the dielectric affects chemistry, yield rate, and ease of processing. When spark-eroding in liquid nitrogen or an organic solvent, nitrides or carbides can often form. The work presented in this dissertation is limited to spark erosion in liquid nitrogen, mainly for purity, ease of post-processing; it doesn't produce any nitrides in the thermoelectric or permanent magnet systems discussed in this dissertation. As discussed in the previous section, the removal of the cryogenic liquid after spark erosion by vaporization is perhaps the simplest way of collecting nanoparticles. The yield rate is influenced by the breakdown voltage of the dielectric. Dielectrics with lower breakdown voltages should induce more sparks. Table 2.1 shows the maximum peak currents for various systems when spark-eroded at 200 V and 120 µF in various dielectric liquids.

Table A.1 Maximum peak currents in amps for various alloys spark-eroded in various dielectrics liquids when spark-eroded at 200 V and 120 μF. * denotes cryogen.

	Al	**Bi-Sb-Te**	**MnBi**	**Si-Ge**
***Liquid Nitrogen**	1920	1200	1600	1500
***Liquid Argon**	1900	1000	1500	-
Ethyl Alcohol	-	-	400	-
Distilled Water	-	500	-	400
Dodecane	1400	-	-	800

A.6 References

[1] A. E. Berkowitz and J. L. Walter, "Spark Erosion: A Method for Producing Rapidly Quenched Fine Powders", J. Mater. Res., **2** (2), 277 (1987).

[2] A. E. Berkowitz, H. Harper, D. J. Smith, H. Hu, Q. Jiang, V. C. Solomon, and H. B. Radousky, "Hollow metallic microspheres produced by spark erosion", Appl. Phys. Lett., Vol. 85, No. 6, (2004).

[3] A. E. Berkowitz, J. L. Walter, and K.F. Wall, "Magnetic Properties of Amorphous Particles Produced by Spark Erosion", Phys. Rev. Lett., Vol. 46, No. 22, 1484 (1981).

[4] A. E. Berkowitz and J. L. Walter, "Ferrofluids Prepared by Spark Erosion", J. Magn. Mater., **39**, 75 (1983).

[5] J. Carrey, H. B. Radousky and A. E. Berkowitz, "Spark-eroded particles: influence of processing parameters", J. Appl. Phys., 95, 823 (2004).

[6] P.-K. Nguyen, K. H. Lee, J. Moon, S. I. Kim, K. A. Ahn, L. H. Chen, S. M Lee, R. K. Chen, S. Jin, and A. E. Berkowitz, "Spark erosion: a high production rate method for producing $Bi_{0.5}Sb_{1.5}Te_3$ nanoparticles with enhanced thermoelectric performance", Nanotechnology **23** 415604-415711 (2012).

APPENDIX B: MAGNETIZATION EXTRAPOLATION

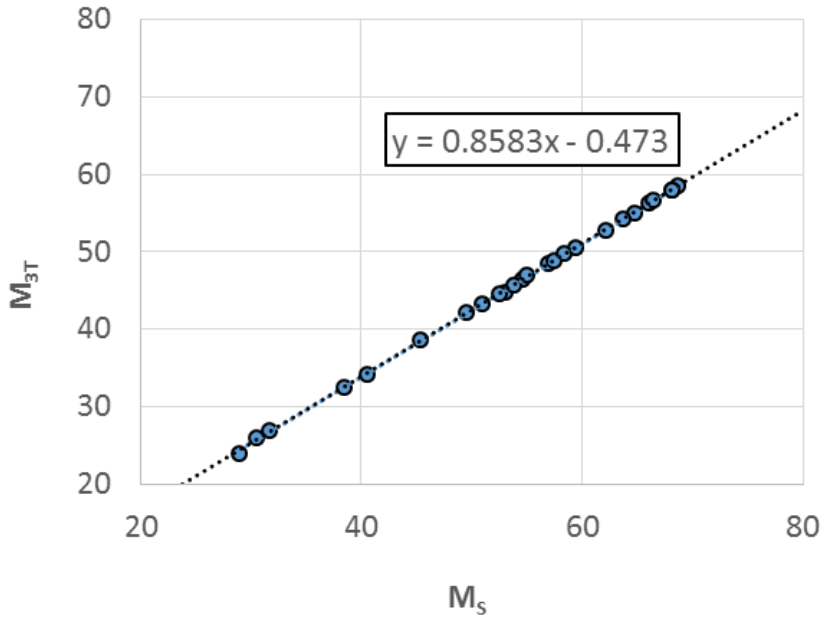

Figure B.1 M_{3T} vs M_S for randomly-oriented MnBi samples that were measured from -7 to +7 T showing a linear relationship

We can extrapolate our MnBi data to determine an approximate M_S for MnBi powder produced with a perfect 80 emu/g MnBi ingot. The missing magnetization can be attributed to dead layers. To do this, the data in Figure 3.21 is first extrapolated from M_{3T} to M_S. For MnBi powders measured in 7 T at room temperature, the M-H loop is closed at 3 T (the bifurcation field is less than 3 T). Therefore, the relationship between M at 3 T and M at 7 T for isotropic, randomly oriented powders is linear. A linear aggression is performed in Figure B.1 using powders that have been measured to 7 T to show this relationship. This can now be used to extrapolate for randomly-oriented MnBi powders that were only measured in 3 T.

APPENDIX C: TWO-PHASE CURVES

Since there are many factors to consider when mixing two different phases, a useful reference is constructed by combining the M-H loops of the constituent phases. Values from the raw data of several samples (Figure C.1) are interpolated in uniform field increments so that they can be accurately added in the proper ratios to produce a theoretical two-phase, non-interacting M-H loop. This can be used to see what a mixture should look like if there were no interactions.

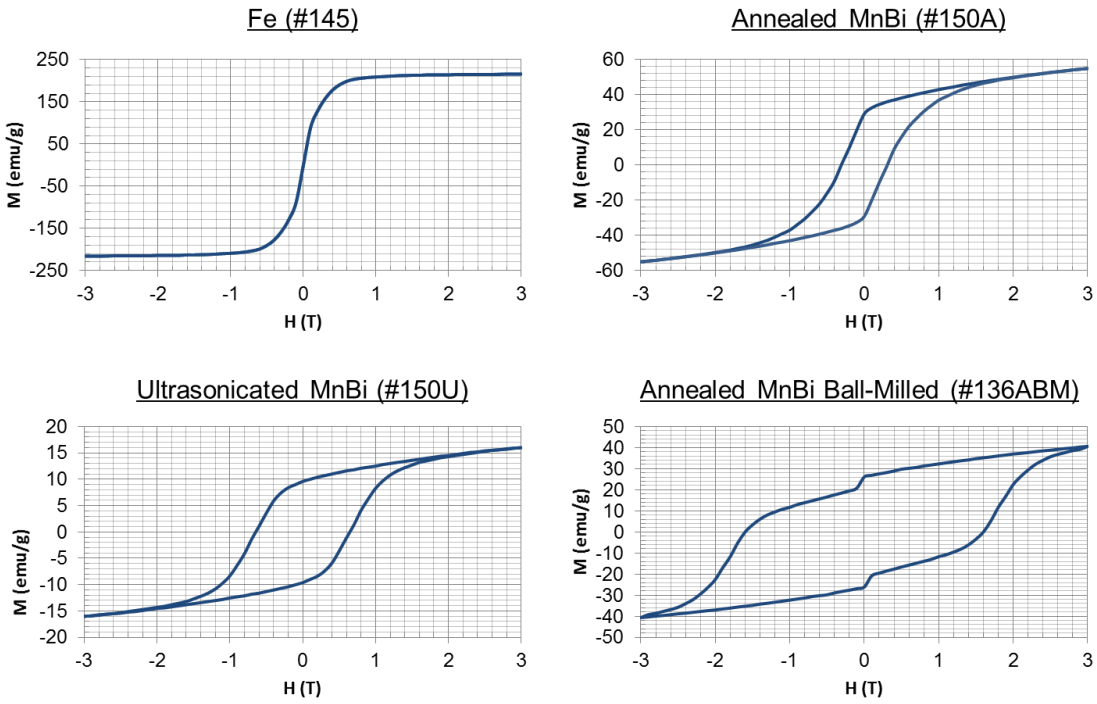

Figure C.1 M-H loops of the constituent phases used for reference when modeling the calculated M-H- loop of a non-interacting two-phase mixture.

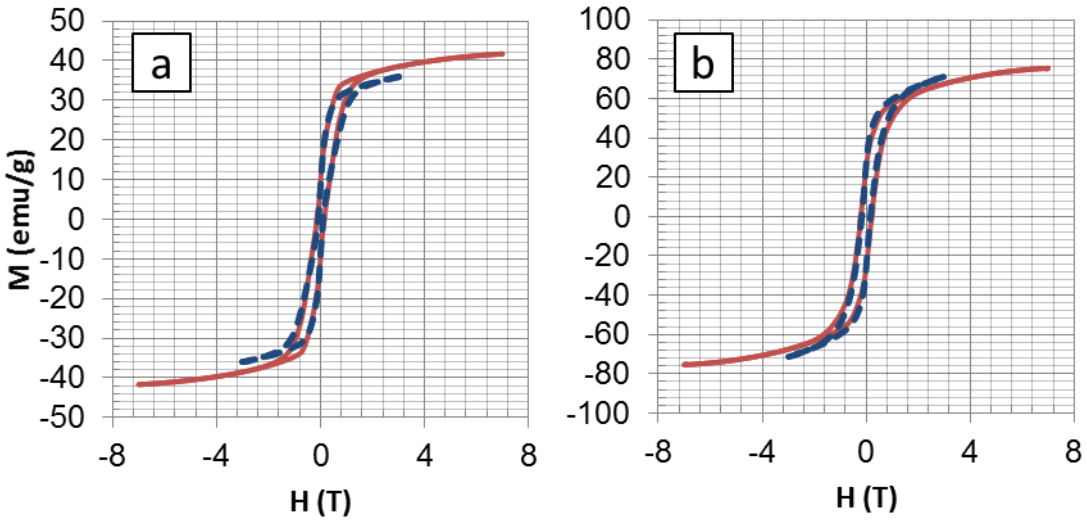

Figure C.2 Experimental mixture of spark-eroded MnBi with 10 wt. % spark-eroded Fe by ultrasonication in hexane compared to theoretical mixture (dotted) (a) before and (b) after annealing.

Figure C.2 shows an ultrasonicated mixture of 90% spark-eroded MnBi and 10% spark-eroded Fe by weight. By comparing these curves with their theoretical counterparts, it can be seen that they act as non-interacting two-phase mixtures. The moment in the mixture before annealing is slightly higher than the theoretical mixture because some crystallization of amorphous MnBi has occurred due to moderate heating from ultrasonication. In the case of the annealed sample, the theoretical mixture looks single-phase since the "kink" normally seen when a soft phase is added is subtle enough to not be noticed. A smooth loop, therefore, is not a good indication of exchange-spring behavior. When $(BH)_{MAX}$ is calculated for these mixtures, the result is indeed lower than the constituent MnBi alone.

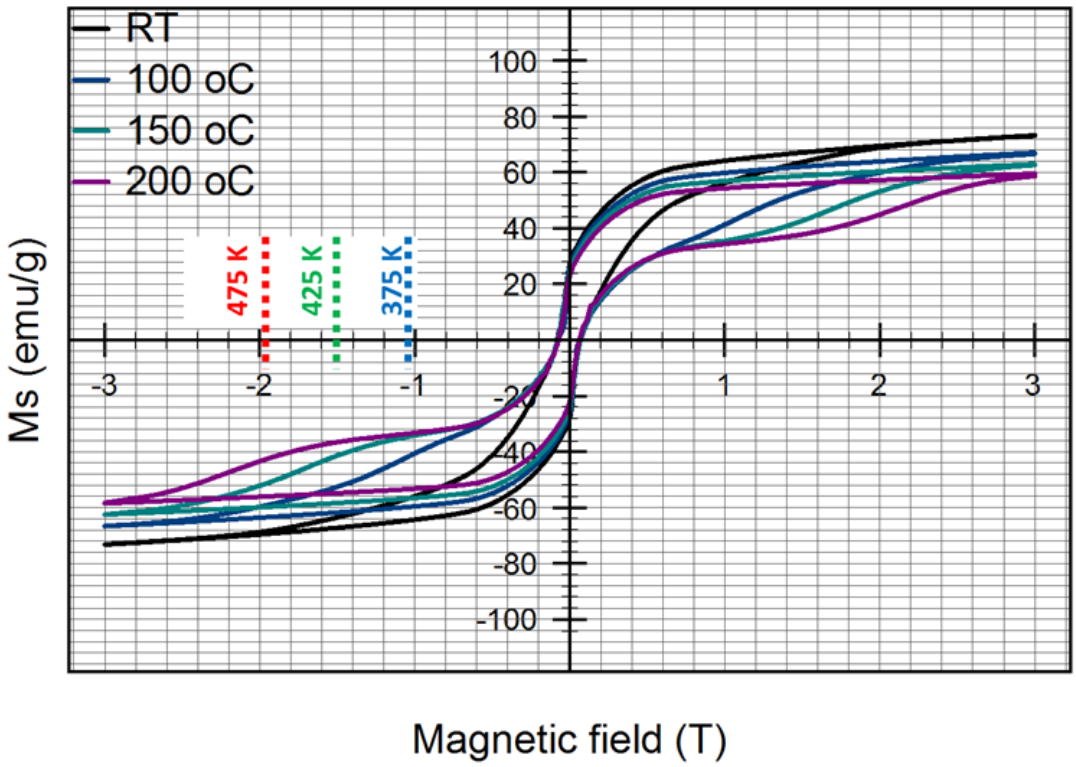

Figure C.3 Ultrasonicated mixture of spark-eroded MnBi with 10 wt. % spark-eroded Fe measured at elevated temperatures showing two-phase behavior.

In order to expand on this point, the same mixture was observed at higher temperatures in Figure C.3. Since H_C of MnBi is expected to increase significantly while H_C of Fe is negligible, the non-smooth two-phase behavior can be seen at elevated temperatures. Because the difference in H_C is large, the kink exists at around the same field as the anticipated H_C of pure MnBi (Figure 3.44). This can thus be a "litmus" test of exchange-spring behavior in an MnBi/Fe system – whether the "single-phase smoothness" is retained at elevated temperature.